Faculty of Mathematics and Physics
Charles University, Prague
2005

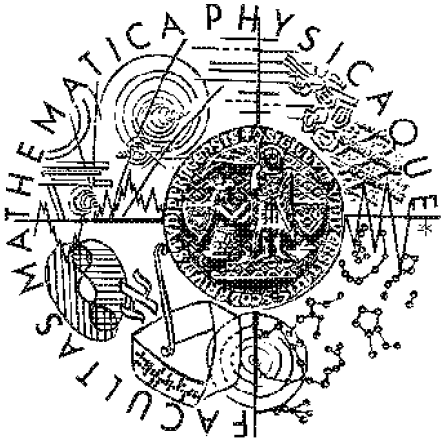

Measurement of pionium lifetime and study of correlation of particles with small relative velocities

Doctoral thesis

Jan Smolík

advisor: Richard Lednický, DrSc.
FZÚ AV ČR

Prohlašuji, že jsem disertační práci vypracoval samostatně s použitím uvedené literatury. Souhlasím se zapůjčováním práce.

V Praze, 29.7.2005 Jan Smolík

Abstract

The goal of DIRAC experiment at CERN is to measure the lifetime of the pionium atom, $A_{2\pi}$, a bound state of a π^+ and π^- meson, through the determination of its breakup probability. The data accumulated between 1999 and 2003 allow us to determine the $A_{2\pi}$ atoms lifetime with precision of 10%.

In this thesis we study the influence of finite size of the production region in the determination of breakup probability P_{br}. The size of the production region is studied using UrQMD simulation code. The results of simulation are compared with $\pi^-\pi^-$ correlation function analysed from data taken during 2001 runs.

Contents

1 Introduction **1**

2 Principles of Particle Correlation **3**
2.1 Short historical preview . . . 3
2.2 General Formalism . . . 4
2.3 Wave function . . . 13
2.3.1 Short-range FSI . . . 13
2.3.2 Coulomb FSI . . . 14
2.4 Bound systems . . . 16

3 Theoretical Background of Experiment **19**
3.1 Motivation . . . 19
3.2 Pionium Lifetime . . . 20
3.3 Method of Lifetime Measurement . . . 21
3.3.1 Production of $A_{2\pi}$ . . . 22
3.3.2 Propagation of $A_{2\pi}$ through target . . . 24
3.3.3 P_{br} determination . . . 25

4 DIRAC apparatus **27**
4.1 General layout description . . . 27
4.2 Beam lines, target station and magnet . . . 27
4.3 Upstream detectors . . . 29
4.3.1 MSGC detector . . . 29
4.3.2 Scintillation Fibre Detector . . . 30
4.3.3 Ionisation Hodoscope . . . 32
4.4 Downstream detectors . . . 32
4.4.1 Drift Chambers . . . 33
4.4.2 Vertical Hodoscope . . . 35
4.4.3 Horizontal Hodoscope . . . 37
4.4.4 Čerenkov Counters . . . 38
4.4.5 Preshower . . . 39
4.4.6 Muon Detector . . . 40
4.5 Trigger . . . 42

4.5.1 Trigger Scheme 42
4.5.2 Zero Level Trigger T0 43
4.5.3 First Level Trigger T1 43
4.5.4 Neural Network Trigger DNA 44
4.5.5 Fourth Level Trigger T4 45
4.6 Set-up performance 46
4.7 Contribution of the author 47

5 Simulated Data **48**
5.1 Simulation of r^* distribution 48
5.2 Correlation Function 63
5.2.1 Weighted Spectra 63
5.2.2 Numerical Computation 66
5.2.3 Correction Factors 68
5.3 Resume 72

6 Data Analysis **76**
6.1 Data selection 76
6.2 Correlation Function 78
6.3 Fit of $\pi^-\pi^-$ correlation function 82
6.4 Resume 86

7 Corrections to $A_{2\pi}$ lifetime measurement **88**
7.1 Uncertainty of n'_{CC} and n'_A 88
7.2 Uncertainty of k_{th} factor 91
7.3 Dependence of systematic shifts on ω yields 91
7.4 Resume 94

8 Summary **96**

Chapter 1

Introduction

The aim of the experiment DIRAC at CERN [1] is to measure the lifetime τ of $A_{2\pi}$ atom, the bound state of π^+ and π^- mesons, with a 10% precission. As this lifetime of order $10^{-15}s$ is determined by the probability of the annihilation $\pi^+\pi^- \to \pi^0\pi^0$, it is related to relevant scattering lengths $1/\tau \sim |a_0 - a_2|^2$. Thus the measurement performed by the experiment DIRAC enables us to determine the absolute value of the difference $a_0 - a_2$ of the s–wave isoscalar and isotensor $\pi\pi$–scattering lengths with a 5% precission in a model–independent way. The pion scattering lengths have been calculated in the framework of chiral perturbation theory with a precision of few per cent. From these values the lifetime of $A_{2\pi}$ atom can be predicted [25] to be $(2.9 \pm 0.1) \times 10^{-15}s$. The precise measurement of this lifetime provides a crucial test for the understanding of the chiral symmetry breaking scenario in QCD.

The method of the lifetime measurement is based on the production of the $A_{2\pi}$ atoms in a thin target and a subsequent detection of highly correlated $\pi^+\pi^-$ pairs leaving the target [17]. These pairs are results of $A_{2\pi}$ atom breakup in the target. The breakup probability P_{br} is a unique function of the target material and its geometry, the velocity of $A_{2\pi}$atoms and its lifetime. To achieve the declared accuracy of 10% for the lifetime measurement, the breakup probability should be measured about 4% precision [1].

In principle, there are two methods - the extrapolation and the subtraction ones - which can be used to measure the breakup probability. The extrapolation method requires the calculation of the number of produced $A_{2\pi}$ atoms N_A based on theory of the final state interaction (FSI) [7],[17]. This calculation, as well as the determination of the number of broken-up atoms n_A, is not required in the subtraction method. This method exploits the data taken at least on three different targets made out of the same material but consisting of a different number of layers of the same total thickness. However, this method needs a factor 7 larger statistics and cannot yield the required precision within the approved time-scale of the experiment DIRAC.

The theoretical computation in the extrapolation method is sensitive to the

finite space-time extent of the pion production region. In [17] the dependence on the distance r^* between the π^+ and π^- production points in their c.m.s. is treated in an approximate way, dividing the pion sources into the short-lived and the long-lived ones. It is assumed that for pion pairs coming from the short-lived source $r^* = 0$ while for other pairs $r^* = \infty$.

The finite-size corrections to this approach are studied in this thesis. For r^* less then 20 fm the relative correction shows a quasi–linear behaviour in q up to about $50 MeV/c$ while for r^* greater than 20 fm this correction has a non-trivial dependence on q [26]. In case that pions are produced at small distances, the correction can easily be taken into account by introducing the linear dependence into the method of determination of produced and broken-up $A_{2\pi}$atoms. However, there is a negligible tail of the distances $r^* > 20 fm$ mainly due to decays of ω and η' resonances. We focus our attention mainly on the influence of ω resonance and we show that it can induce a systematic shift in the determination of breakup probability on a level of several per cent. The influence of η' is not so important due to a small yield of this resonance and the fact that its contribution is to a large extent accounted for in the fraction of long lived sources treated as a free parameter.

Our studies are based on the simulation of r^*–distribution using UrQMD code. To check the reliability of the simulated results we extract from the measured data a $\pi^-\pi^-$ correlation function. This function contains the information about the distances r^* between π^-emission points under the same experimental conditions as the $A_{2\pi}$ lifetime is evaluated. Comparing this correlation function with the one obtained from simulated data for $\pi^-\pi^-$pairs we can check the reliability of the simulated r^*–distribution.

The results obtained in this thesis have been presented at several collaboration meetings during the years 2003 and 2004. Since then they are commonly used in the collaboration publications to evaluate systematic errors due to the effect of the finite size of the production region [2],[3]. Besides the official publications they were also used in a doctoral thesis [43]. They play a significant role in choosing a suitable measurement method for the future continuation of the experiment DIRAC [44].

The submitted thesis is organised as follows. In Chapter 2 we present principles of the theory of two-particle correlations due to the effects of final state interaction and quantum statistics. Chapter 3 gives an explanation of the method used for the measurement of $A_{2\pi}$lifetime and Chapter 4 contains the description of the experimental set-up. In Chapter 5 we analyse the simulated data with a focus on r^*–distribution and calculate the correlation function on the basis of this distribution. Chapter 6 is devoted to the extraction of the $\pi^-\pi^-$ correlation function from the measured data and a comparison of this function with the simulated one. Possible systematic shifts in the measurement of the breakup probability are evaluated in Chapter 7. The main results are summarised in Chapter 8.

Chapter 2

Principles of Particle Correlation

In this chapter the principles of the theory of particle correlations at small relative velocities are discussed. The main attention is focused on the problems related to the experiment DIRAC [30] performed at CERN Proton Synchrotron, which is consecrated to study of $A_{2\pi}$atoms. Good understanding of the correlations of identical and non-identical pions with small relative velocities is crucial for this experiment.

2.1 Short historical preview

The effect of momentum correlations was firstly observed in 1960 [4] as an enhanced production of the identical pion pairs with small opening angles, as compared to the production of nonidentical ones. This effect was named after its authors, G.Goldhaber, S.Goldhaber, W.Lee and A.Pais, GGLP effect.

In 70's Kopylov and Podgoretsky settled the basics of correlation femtoscopy [5]. They took cognisance of analogy between GGLP and HBT effects. HBT (Hanbury-Brown, Twist) effect, [6], allows one to measure the angular radii of stars by studying the dependence of a two photon space-time correlation rate on the distance between two separate detectors. Similar to astronomy they suggested to study the interference effects in terms of correlation functions. Despite fundamental differences between basic principles of these effects the adopted way turned out to be successful. In a series of papers Kopylov and Podgoretsky studied the influence of space-time parameters of a production region on the directional and the velocity dependence of the correlation function in various situations.

Now, this method is widely used as a tool for measurement of space-time characteristics of particle production processes. Due to this applicability it is also called correlation femtoscopy and it is used for evaluations in many heavy ion experiments, for example STAR or NA49.

2.2 General Formalism

The production of two particles with a small relative velocity is influenced by their mutual final state interaction (FSI) and, in case of the identical particles it is also determined by fundamental laws of quantum statistic (QS). To allow the separation of the FSI effect from the production process a sufficiently long two-particle interaction time in the final state must be provided as compared with the characteristic time of the production process. In other words, the magnitude of the relative momentum vector has to be much smaller than momentum transfer typical for particle production, which is several hundreds MeV/c.

Effects of FSI and QS are studied in terms of the correlation function $R(p_1, p_2)$, which is defined as the ratio of inclusive two-particle cross sections with or without influence of both FSI and QS

$$R(p_1, p_2) = \frac{(\frac{d^6\sigma}{d^3p_1 d^3p_2})}{(\frac{d^6\sigma_0}{d^3p_1 d^3p_2})}. \tag{2.1}$$

Since the Nature does not allow us to perform a measurement with the absence of FSI and QS effects, the denominator in (2.1) is obviously replaced by two-particle cross section obtained by mixing particles from different events $\frac{d^6\sigma_{mix}}{d^3p_1 d^3p_2}$. This substitution is valid in the cases when the kinematics constraints can be neglected. It is true in most heavy-ion and high energy experiments with a high multiplicity of studied particles. In case of DIRAC experiment this condition is not fully satisfied and some correction must be provided.

FSI influence

The inclusive double production cross section for pairs of particles with four-momenta p_1 and p_2 can be written in form

$$\frac{d^6\sigma}{d^3p_1 d^3p_2} = \frac{1}{(2\pi)^6 \gamma_1 \gamma_2} \sum_{\alpha} |T(p_1, p_2, ; \alpha)|^2, \tag{2.2}$$

where γ_i are Lorentz factors of particles ($\gamma_i = E_i/m_i$) and $T(p_1, p_2, ; \alpha)$ is invariant production amplitude. The sum is performed over the total spin S of the pair and its projection M and over all quantum numbers of other produced particles. It also includes the integration over their momenta with the energy and the momentum conservation law taken into account.

In ordinary processes particles are produced with large relative velocities while the studied pairs with small relative velocities are created seldom. Therefore, we can suppose that particles of the studied pair are separated in phase space from the other ones and, due to sharp fall of FSI with relative velocity, we can neglect the influence of other particles on the ones of this pair and write the invariant

production amplitude as a sum

$$T(p_1, p_2, \alpha) = T_0(p_1, p_2, \alpha) + \Delta T(p_1, p_2, \alpha), \tag{2.3}$$

where T_0 is the production amplitude without influence of FSI and ΔT represents the FSI contribution coming from the interaction between the particles of the pair. ΔT can be expressed by this formula

$$\Delta T(p_1, P_2, \alpha) = \frac{i\sqrt{P^2}}{2\pi^3} \int d^4\kappa \frac{T_0(\kappa, P-\kappa; \alpha) f^{S*}(p_1, p_2; \kappa, P-\kappa)}{(\kappa^2 - m_1^2 - i0)[(P-\kappa)^2 - m_2^2 - i0]}, \tag{2.4}$$

where $P \equiv 2p = p_1 + p_2$, $T_0(\kappa, P-\kappa; \alpha)$ is the analytically continued off mass-shell production amplitude, $f^{S*}(p_1, p_2; \kappa, P-\kappa)$ is the scattering amplitude of the studied particles, also off mass-shell continued.

Using Fourier transformation we can transform the production amplitude T_0 from momentum representation into the space-time representation $\mathcal{T}$

$$T_0(p_1, p_2; \alpha) = \int \mathrm{d}^4x_1\, \mathrm{d}^4x_2\ \mathrm{e}^{-ip_1x_1 - ip_2x_2} \mathcal{T}(x_1, x_2; \alpha) = \int \mathrm{d}^4x\ \mathrm{e}^{-i\tilde{q}x/2} \tau_P(x; \alpha), \tag{2.5}$$

where the second expression arises after integration over the pair c.m.s. four-coordinate $X = [(p_1P)x_1 + (p_2P)x_2]/P^2$ based on separation of the phase factors due to the free c.m.s. and relative motions

$$\mathrm{e}^{-ip_1x_1 - ip_2x_2} = \mathrm{e}^{-iPX} \mathrm{e}^{-i\tilde{q}x/2}.$$

The relative four–coordinate $x = x_1 - x_2$ and generalised relative four-momentum satisfy relations $\tilde{q} = q - P(qP)/P^2$, $q = p_1 - p_2$ and $(qP) = m_1^2 - m_2^2$. In case of $m_1 = m_2$ is $\tilde{q} = q$.

The total production amplitude T can be expressed in a similar way to (2.5) by replacing plane wave $\mathrm{e}^{-ip_1x_1 - ip_2x_2}$ by Bethe-Salpeter amplitude $\Psi^{S(-)}_{p_1,p_2}(x_1, x_2)$

$$T(p_1, p_2; \alpha) = \int \mathrm{d}^4x_1\, \mathrm{d}^4x_2 \Psi^{S(-)}_{p_1,p_2}(x_1, x_2) \mathcal{T}(x_1, x_2; \alpha) = \int \mathrm{d}^4x \psi^{S(-)}_{\tilde{q}}(x) \tau_P(x; \alpha), \tag{2.6}$$

where again the integration over pair c.m.s. four-coordinate in the second expression was performed resulting in

$$\Psi^{S(-)}_{p_1,p_2}(x_1, x_2) = [\Psi^{S(+)}_{p_1,p_2}(x_1, x_2)]^* = [\mathrm{e}^{iPX} \psi^{S(+)}_{\tilde{q}}(x)]^*. \tag{2.7}$$

Thus, on the assumption of quasi-free propagation of the low-mass two-particle system, the production amplitude is determined by the convolution of the space-time reduced production amplitude without FSI $\tau_P(x; \alpha)$ and the reduced Bethe-Salpeter amplitude $\psi^{S(-)}_{\tilde{q}}(x)$, both depending only on a relative four-coordinate x and on a generalised four-momenta $\tilde{q}$.

Further more $\psi^{S(-)}_{\tilde{q}}(x)$ can be written as

$$\psi^{S(+)}_{\tilde{q}}(x) = \mathrm{e}^{i\tilde{q}x/2} + \Delta\psi^{S(+)}_{\tilde{q}}(x), \tag{2.8}$$

where the correction to the plane wave is

$$\Delta\psi^{S(+)}_{\tilde{q}}(x) = \frac{\sqrt{P^2}}{2\pi^3 i}\mathrm{e}^{-iPx(1+Pq/P^2)/2}\int \mathrm{d}^4\kappa \frac{\mathrm{e}^{i\kappa x} f^S(p_1,p_2;\kappa,P-\kappa)}{(\kappa^2 - {m_1}^2 + i0)[(P-\kappa)^2 - {m_2}^2 + i0]}. \tag{2.9}$$

It is necessary to note, that in the two particle c.m.s. system, where $P = 0$, $\tilde{q} = \{0, 2\mathbf{k}^*\}$, $x = \{t^*, \mathbf{r}^*\}$, the reduced amplitude $\psi^{S(+)}_{\tilde{q}}(x)$ at $t^* = t^*_1 - t^*_2 = 0$ becomes identical with stationary solution $\psi^S_{-\mathbf{k}^*}(\mathbf{r}^*)$ of the scattering problem at non-relativistic quantum mechanics.

Although expressions (2.5) and (2.6) express different physical situations they both contain the same space-time representation of the production amplitude T_0. The influence of FSI manifested itself in replacement of plane wave $\mathrm{e}^{-i\tilde{q}x/2}$ in Eq.(2.5) by Bethe-Salpeter amplitude $\psi^{S(-)}_{\tilde{q}}(x)$ in Eq.(2.6).

Substituting the representation (2.6) of production amplitude T into the Eq.(2.2) we can write the inclusive double cross section in the form

$$(2\pi)^6\gamma_1\gamma_2\frac{d^6\sigma}{d^3\mathbf{p}_1 d^3\mathbf{p}_2} =$$

$$= \sum_S \int d^4x_1\, d^4x_2\, d^4x'_1\, d^4x'_2 \rho_S(x_1,x_2;x'_1,x'_2)\Psi^{S(-)}_{p_1,p_2}(x_1,x_2)\Psi^{S(-)*}_{p_1,p_2}(x'_1,x'_2) =$$

$$= \sum_S \int d^4x\, d^4x' \rho_{PS}(x;x')\psi^{S(-)}_{\tilde{q}}(x)\psi^{S(-)*}_{\tilde{q}}(x'), \tag{2.10}$$

where the functions $\rho_S(x_1,x_2;x'_1,x'_2)$ and $\rho_{PS}(x;x')$ represent elements of non–normalised two-particle space-time density matrices. They are defined as follows

$$\rho_S(x_1,x_2;x'_1,x'_2) = \sum_{\alpha'} \mathcal{T}(x_1,x_2;S,\alpha')\mathcal{T}^*(x'_1,x'_2;S,\alpha'),$$

$$\rho_{PS}(x;x') = \sum_{\alpha'} \tau_P(x;S,\alpha')\tau^*_P(x';S,\alpha') \equiv \tag{2.11}$$

$$\int d^4X\, d^4X' \mathrm{e}^{-iP(X-X')}\rho_S(X + \frac{p_2P}{P^2}x, X - \frac{p_1P}{P^2}x; X' + \frac{p_2P}{P^2}x', X' - \frac{p_1P}{P^2}x').$$

Using this representation we can write the cross section for production of two close non-identical particles without influence of FSI in the form

$$(2\pi)^6\gamma_1\gamma_2\frac{d^6\sigma_0}{d^3\mathbf{p}_1 d^3\mathbf{p}_2} =$$

$$= \sum_S \int d^4x_1\, d^4x_2\, d^4x_1'\, d^4x_2' \rho_S(x_1, x_2; x_1', x_2') \mathrm{e}^{-ip_1(x_1-x_1')-ip_2(x_2-x_2')} =$$

$$= \sum_S \int d^4x\, d^4x' \rho_{PS}(x; x') \mathrm{e}^{-i\tilde{q}(x-x')/2} \tag{2.12}$$

and using this we can rewrite Eq.(2.10) as

$$\frac{d^6\sigma}{d^3\mathbf{p}_1 d^3\mathbf{p}_2} = \frac{d^6\sigma_0}{d^3\mathbf{p}_1 d^3\mathbf{p}_2} \sum_S \mathcal{G}_S(p_1, p_2) \left\langle \Psi^{S(-)}_{p_1,p_2}(x_1, x_2) \Psi^{S(-)*}_{p_1,p_2}(x_1', x_2') \right\rangle'_{p_1p_2S} =$$

$$= \frac{d^6\sigma_0}{d^3\mathbf{p}_1 d^3\mathbf{p}_2} \sum_S \mathcal{G}_S(p_1, p_2) \left\langle \psi^{S(-)}_{\tilde{q}}(x) \psi^{S(-)*}_{\tilde{q}}(x') \right\rangle'_{\tilde{q}PS}, \tag{2.13}$$

where we used the quasi-averages of the bilinear products of the Bethe-Salpeter amplitudes defined as

$$\left\langle \Psi^{S(-)}_{p_1,p_2}(x_1, x_2) \Psi^{S(-)*}_{p_1,p_2}(x_1', x_2') \right\rangle'_{p_1p_2S} =$$

$$= \frac{\int d^4x_1\, d^4x_2\, d^4x_1'\, d^4x_2' \rho_S(x_1, x_2; x_1', x_2') \Psi^{S(-)}_{p_1,p_2}(x_1, x_2) \Psi^{S(-)*}_{p_1,p_2}(x_1', x_2')}{\int d^4x_1\, d^4x_2\, d^4x_1'\, d^4x_2' \rho_S(x_1, x_2; x_1', x_2') \mathrm{e}^{-ip_1(x_1-x_1')-ip_2(x_2-x_2')}} \tag{2.14}$$

$$\left\langle \psi^{S(-)}_{\tilde{q}}(x) \psi^{S(-)*}_{\tilde{q}}(x') \right\rangle'_{\tilde{q}PS} = \frac{\int d^4x\, d^4x' \rho_{PS}(x; x') \psi^{S(-)}_{\tilde{q}}(x) \psi^{S(-)*}_{\tilde{q}}(x')}{\int d^4x\, d^4x' \rho_{PS}(x; x') \mathrm{e}^{-i\tilde{q}(x-x')/2}} \tag{2.15}$$

and the statistical factor $\mathcal{G}_S$ representing the population probabilities of the pair spin-S states out of the region of the correlation effect in form

$$\mathcal{G}_S(p_1, p_2) = \frac{\int d^4x_1\, d^4x_2\, d^4x_1'\, d^4x_2' \rho_S(x_1, x_2; x_1', x_2') \mathrm{e}^{-ip_1(x_1-x_1')-ip_2(x_2-x_2')}}{\sum\limits_S \int d^4x_1\, d^4x_2\, d^4x_1'\, d^4x_2' \rho_S(x_1, x_2; x_1', x_2') \mathrm{e}^{-ip_1(x_1-x_1')-ip_2(x_2-x_2')}} =$$

$$= \frac{\int d^4x\, d^4x' \rho_{PS}(x; x') \mathrm{e}^{-i\tilde{q}(x-x')/2}}{\sum\limits_S \int d^4x\, d^4x' \rho_{PS}(x; x') \mathrm{e}^{-i\tilde{q}(x-x')/2}}. \tag{2.16}$$

Note that for unpolarised particles with spins j_1 and j_2 the statistical factor $\mathcal{G}_S$ is

$$\mathcal{G}_S = (2S+1)/[(2j_1+1)(2j_2+1)], \quad \sum_S \mathcal{G}_S = 1. \tag{2.17}$$

Finally, the correlation function of two non-identical particles can be written in the form

$$R(p_1, p_2) = \sum_S \mathcal{G}_S(p_1, p_2) \left\langle \Psi^{S(-)}_{p_1,p_2}(x_1, x_2) \Psi^{S(-)*}_{p_1,p_2}(x_1', x_2') \right\rangle'_{p_1p_2S} =$$

$$= \sum_S \mathcal{G}_S(p_1, p_2) \left\langle \psi^{S(-)}_{\tilde{q}}(x) \psi^{S(-)*}_{\tilde{q}}(x') \right\rangle'_{\tilde{q}PS}. \tag{2.18}$$

QS influence

The all formulae mentioned above, which deal with FSI influence, are valid for identical particles with one significant difference. Due to the effect of quantum statistics the Bethe-Salpeter amplitudes $\Psi^{S(-)}_{p_1,p_2}$ in these formulae must be replaced by their properly symmetrized combinations

$$\Psi^{S(-)}_{p_1,p_2}(x_1,x_2) \to \frac{1}{\sqrt{2}}[\Psi^{S(-)}_{p_1,p_2}(x_1,x_2) + (-1)^S \Psi^{S(-)}_{p_2,p_1}(x_1,x_2)]. \tag{2.19}$$

Consider the case of production of two identical non-interacting particles. Firstly, let us define emission functions G_S and g_{PS} as partial Fourier transformation of space-time density matrices ρ_S and ρ_{PS}

$$G_S(\bar{x}_1,p_1;\bar{x}_1,p_2) = \int \mathrm{d}^4\epsilon_1\,\mathrm{d}^4\epsilon_2 \mathrm{e}^{-ip_1\epsilon_1 - ip_2\epsilon_2}\rho_S(\bar{x}_1+\frac{\epsilon_1}{2},\bar{x}_2+\frac{\epsilon_2}{2};\bar{x}_1-\frac{\epsilon_1}{2},\bar{x}_2-\frac{\epsilon_2}{2}),$$

$$g_{PS}(\bar{x};\widetilde{q}) = \int \mathrm{d}^4\bar{X} G_S(\bar{X}+\frac{p_2P}{P^2}\bar{x},p_1;\bar{X}-\frac{p_1P}{P^2}\bar{x},p_2) =$$

$$= \int \mathrm{d}^4\epsilon \mathrm{e}^{-i\widetilde{q}\epsilon/2}\rho_{PS}(\bar{x}+\frac{\epsilon}{2},\bar{x}-\frac{\epsilon}{2}). \tag{2.20}$$

Here we make the substitution $x_i, x_i' \to \bar{x}_i = \frac{1}{2}(x_i+x_i'), \epsilon_i = x_i - x_i'$ and $\bar{x} = \bar{x}_1 - \bar{x}_2$. Now we can rewrite Eq.(2.12) into the form

$$(2\pi)^6\gamma_1\gamma_2\frac{\mathrm{d}^6\sigma_0}{\mathrm{d}^3\mathbf{p}_1\mathrm{d}^3\mathbf{p}_2} = \sum_S \int \mathrm{d}^4\bar{x}_1\,\mathrm{d}^4\bar{x}_2 G_S(\bar{x}_1,p_1;\bar{x}_2,p_2) = \sum_S \int \mathrm{d}^4\bar{x} g_{PS}(\bar{x},\widetilde{q}), \tag{2.21}$$

and if we substitute the Bethe-Salpeter amplitudes in Eq.(2.10) by properly symmetrized combination of the plane waves we get for inclusive double cross section the following expression

$$(2\pi)^6\gamma_1\gamma_2\frac{\mathrm{d}^6\sigma}{\mathrm{d}^3\mathbf{p}_1\mathrm{d}^3\mathbf{p}_2} = \sum_S \int \mathrm{d}^4\bar{x}_1\,\mathrm{d}^4\bar{x}_2[G_S(\bar{x}_1,p_1;\bar{x}_2,p_2)+G_S(\bar{x}_1,p;\bar{x}_2,p)(-1)^S\cos(q\bar{x})]$$

$$= \sum_S \int \mathrm{d}^4\bar{x}[g_{PS}(\bar{x},q) + g_{PS}(\bar{x},0)(-1)^S\cos(q\bar{x})], \tag{2.22}$$

where $p = (p_1+p_2)/2$ is off-mass-shell four-momentum. The presence of the emission functions $G_S(\bar{x}_1,p;\bar{x}_2,p)$ and $g_{PS}(\bar{x},0)$ is a direct consequence of the interference of symmetrized two-particle plane waves.

Putting the formula's (2.21) and (2.22) directly into the definition of correlation function (2.1) we obtain

$$\mathcal{R}(p_1,p_2) = 1 + \frac{\sum_S \int \mathrm{d}^4\bar{x}_1\,\mathrm{d}^4\bar{x}_2 G_S(\bar{x}_1,p;\bar{x}_2,p)(-1)^S\cos(q\bar{x})}{\sum_S \int \mathrm{d}^4\bar{x}_1\,\mathrm{d}^4\bar{x}_2 G_S(\bar{x}_1,p_1;\bar{x}_2,p_2)}$$

$$= 1 + \frac{\sum\limits_S \int \mathrm{d}^4\bar{x} g_{PS}(\bar{x},0)(-1)^S \cos(q\bar{x})}{\sum\limits_S \int \mathrm{d}^4\bar{x} g_{PS}(\bar{x},q)} \tag{2.23}$$

Smoothness assumption

Consider the simple case of the particle emission by one-particle sources according to the one-particle production amplitude

$$\mathcal{T}_A^{(1)}(x_1;x_A) \sim \exp[-\frac{(\mathbf{x}_1-\mathbf{x}_A)^2}{2{r_A}^2} - \frac{(x_{01}-x_{0A})^2}{2{\tau_A}^2}] \exp(-\frac{{\mathbf{x}_A}^2}{4{r_0}^2} - \frac{{x_{0A}}^2}{4{\tau_0}^2}), \tag{2.24}$$

which corresponds to the source at rest with Gaussian distribution of the emission points $x_1 = \{x_{01}, \mathbf{x}_1\}$ with characteristic widths r_A, τ_A around the source centres $x_A = \{x_{0A}, \mathbf{x}_A\}$, also Gaussian distributed with widths r_0, τ_0. Assuming further that the sources are sufficiently heavy, we can describe them classically. The four-coordinates of the source centres x_A can then be considered as a part of the quantum numbers α' and the sum in Eq.(2.11) contains the integration over x_A. Performing this integration and substituting $x_1, x_1' \to \bar{x}_1 = \frac{1}{2}(x_1+x_1'), \epsilon_1 = x_1 - x_1'$ we get the one-particle space-time density matrix

$$\rho_A^{(1)}(x_1,x_1') \sim \exp(-\frac{{\boldsymbol{\epsilon}_1}^2}{4{r_A}^2} - \frac{{\epsilon_{01}}^2}{4{\tau_A}^2}) \exp(-\frac{{\bar{\mathbf{x}}_1}^2}{2{r_0}^2+{r_A}^2} - \frac{{\bar{x}_{01}}^2}{2{\tau_0}^2+{\tau_A}^2}) \tag{2.25}$$

and the corresponding one-particle emission function

$$G_A^{(1)}(\bar{x}_1,p) \sim \exp(-{r_A}^2\mathbf{p}^2 - {\tau_A}^2{p_0}^2) \exp(-\frac{{\bar{\mathbf{x}}_1}^2}{2{r_0}^2+{r_A}^2} - \frac{{\bar{x}_{01}}^2}{2{\tau_0}^2+{\tau_A}^2}). \tag{2.26}$$

We can see that the source space-time dimensions r_A and τ_A determine both the non-diagonality of space-time density matrix and the distribution of particle four-momenta. In a particular case of the sources of a negligible space-time extent ($r_A = 0$ and $\tau_A = 0$) any particle four-momenta are equally probable.[1]

The actual estimation of r_A and τ_A, based on experimental data, yields on average $r_A^2 + \tau_A^2 \approx 0.1 fm^2$ (based on the analysis of single-particle spectra in [8]). Contrary to this the effective value of r_0^2 and τ_0^2 are about $1 fm^2$ for hadron-hadron interaction and of several tens of fm^2 for the collisions involving heavy nuclei.

[1]Note that for a source moving with a non–relativistic velocity $\boldsymbol{\beta}_A$ and emitting the particle with the mean three–momentum $\mathbf{p}_A = m_1\boldsymbol{\beta}_A$, Eqs. (2.24) and (2.25) acquire phase factors $\mathrm{e}^{i\mathbf{p}_A\mathbf{x}_1}$ and $\mathrm{e}^{i\mathbf{p}_A\boldsymbol{\epsilon}_1}$ respectively and the substitution $\mathbf{p} \to \mathbf{p} - \mathbf{p}_A$ has to be done in Eq. (2.26). If the $\mathbf{p}_A$–distribution decouples from the distribution of other source characteristics in a Gaussian form of a width Δ_0, we still arrive at Eqs. (2.25), (2.26), up to a substitution ${r_A}^2 \to {r_A}^2/[2(r_A\Delta_0)^2+1]$ in the first factor, corresponding to a widening of the momentum distribution due to the dispersion of the source velocities.

The smoothness condition, which requires

$$r_A^2/2 \ll r_0^2, \quad \tau_A^2/2 \ll \tau_0^2, \tag{2.27}$$

guarantees, that influence of the space-time extents of sources r_A and τ_A are negligible in comparison with the space-time extent of the distribution of the sources. Due to a small value of r_A and τ_A the momentum dependence of emission function is weak (see Eq.(2.26)) and we can neglect its dependence on the four-momentum difference q in the region of the interference effect characterised by the inverse space-time distance between the particle production points. It means, smoothness assumption allows us to rewrite expression (2.23) describing correlation of identical particles into the form

$$R(p_1,p_2) \doteq 1 + \frac{\sum\limits_S \int \mathrm{d}^4\bar{x}_1\, \mathrm{d}^4\bar{x}_2 G_S(\bar{x}_1,p_1;\bar{x}_2,p_2)(-1)^S \cos(q\bar{x})}{\sum\limits_S \int \mathrm{d}^4\bar{x}_1\, \mathrm{d}^4\bar{x}_2 G_S(\bar{x}_1,p_1;\bar{x}_2,p_2)}$$

$$= 1 + \frac{\sum\limits_S \int \mathrm{d}^4\bar{x}\, g_{PS}(\bar{x},q)(-1)^S \cos(q\bar{x})}{\sum\limits_S \int \mathrm{d}^4\bar{x}\, g_{PS}(\bar{x},q)}, \tag{2.28}$$

where we replace $G_S(\bar{x}_1,p;\bar{x}_2,p)$ by $G_S(\bar{x}_1,p_1;\bar{x}_2,p_2)$ and $g_{PS}(\bar{x},0)$ by $g_{PS}(\bar{x},q)$.

Assuming, for example, there is a fraction λ of pairs of identical particles which are emitted by independent one-particle sources described by Gaussian amplitude (2.24). The remaining fraction $(1-\lambda)$ is related to very long-life source as $\eta, K_s^0, \Lambda, \ldots$, what means that relative distances r^* in the pair c.m.s. are extremely large and no correlation effect appears. In this situation the correlation function would have this form

$$R(p_1,p_2) = 1 + \lambda \sum_S \mathcal{G}_S(-1)^S exp(-r_0^2 q^2 - \tau_0^2 q_0^2). \tag{2.29}$$

This simple model shows, that a characteristic feature of the correlation function of identical particles is the presence of an interference maximum or minimum at region of small q, changing to a horizontal plateau at sufficiently large q (i.e. large in comparison with the inverse characteristic space-time distance between the particle emission points).

To take into account the finite size of the sources, we should provide in Eq.(2.29) substitution $r_0^2 \to r_0^2 + r_A^2/2$, see [10]. In case of Gaussian distribution of the mean emission three-momentum p_A of a width Δ_0 the substitution is $r_0^2 \to r_0^2 + r_A^2/[2 + (r_A\Delta_0)^{-2}]$. It is evident, that if the smoothness condition (2.27) is satisfied, the both effects become negligible.

The two particle emission function $G_S(\bar{x}_1,p_1;\bar{x}_2,p_2)$ can also be used to express a production cross section for interacting particles. In case that smoothness

condition is fulfilled, we can rewrite Eq.(2.10) in an approximate form

$$(2\pi)^6\gamma_1\gamma_2\frac{\mathrm{d}^6\sigma}{\mathrm{d}^3\mathbf{p}_1\mathrm{d}^3\mathbf{p}_2} \doteq \sum_S \int \mathrm{d}^4x_1\,\mathrm{d}^4x_2 G_S(x_1,p_1;x_2,p_2)|\psi_{\widetilde{q}}^{S(+)}(x)|^2 =$$

$$= \sum_S \int \mathrm{d}^4x g_{PS}(x,\widetilde{q})|\psi_{\widetilde{q}}^{S(+)}(x)|^2. \tag{2.30}$$

Let us define an averaging

$$\langle|\psi_{\widetilde{q}}^{S(+)}(x)|^2\rangle_{\widetilde{q}PS} = \frac{\int \mathrm{d}^4x_1\,\mathrm{d}^4x_2 G_S(x_1,p_1;x_2,p_2)|\psi_{\widetilde{q}}^{S(+)}(x)|^2}{\int \mathrm{d}^4x_1\,\mathrm{d}^4x_2 G_S(x_1,p_1;x_2,p_2)} \tag{2.31}$$

and than we can write Eq.(2.30) as

$$\frac{\mathrm{d}^6\sigma}{\mathrm{d}^3\mathbf{p}_1\mathrm{d}^3\mathbf{p}_2} \doteq \frac{\mathrm{d}^6\sigma_0}{\mathrm{d}^3\mathbf{p}_1\mathrm{d}^3\mathbf{p}_2}\sum_S \mathcal{G}_S\langle|\psi_{\widetilde{q}}^{S(+)}(x)|^2\rangle_{\widetilde{q}PS}. \tag{2.32}$$

Using this approximation directly in the definition (2.1) we obtain for the correlation function simple expression

$$R(p_1,p_2) \doteq \sum_S \mathcal{G}_S\langle|\psi_{\widetilde{q}}^{S(+)}(x)|^2\rangle_{\widetilde{q}PS}. \tag{2.33}$$

Remind that for identical particles the Bethe-Salpeter amplitudes must be symmetrized according to Eq.(2.19).

Approximative expressions mentioned above are valid up to correction representing by a fraction of $(r_A^2+v^2\tau_A^2)/(r_0^2+v^2\tau_0^2)$, where v is a pair velocity in the rest frame of sources. This correction is less than a few percent for high energy hadron-hadron collisions and less than a few per-mil for collisions involving nuclei in case of identical particles. For non-identical particles this correction is substantially smaller.

In addition to simplification of the correlation function calculation, the smoothness assumption allows us to use classical transport codes like RQMD, UrQMD or VENUS for simulations of correlation problems. These codes produce sharp information about space-time position together with momentum information. This is in conflict with the uncertainty principle and can be used as an approximation only if the non-diagonality of the space-time density matrix is small. The smoothness condition makes this certain.

Equal-time approximation

For non-interacting and non-identical particles Bethe-Salpeter amplitude $\psi_{\widetilde{q}}^{(+)}(x) = \mathrm{e}^{-i\mathbf{k}^*\mathbf{r}^*}$ is independent of the relative emission time t^* in the c.m.s. of the pair.

However, for interacting particles Bethe-Salpeter amplitude is explicitly dependent on t^*. The effect of mutual interaction is vanishing with the increase in t^*.

It can be shown [7], that the effect of non-zero t^* can be neglected on condition

$$|t^*| \ll m(t^*)r^{*2}, \tag{2.34}$$

where $m(t^* > 0) = m_2$ and $m(t^* < 0) = m_1$. In this case we can use the approximation of equal emission times of the two particles in their c.m.s ($t^* = 0$) and substitute the Bethe-Salpeter amplitude by the non-relativistic two-particle wave function $\psi^S_{-\mathbf{k}^*}(\mathbf{r}^*)$.

The condition (2.34) is usually satisfied for heavy particles like kaons or nucleons. But even for pions this approximation merely leads to a slight overestimation (typically less than a few percent) of the strong FSI contribution to the production cross section [7].

For example, let us assume simple static model of independent one-particle Gaussian source described by amplitude (2.24).[2] In this model, the condition (2.35) of the equal-time approximation can be roughly written in the form [7]

$$\tau_0 \ll \mu\gamma r_0({r_0}^2 + v^2{\tau_0}^2)^{1/2}. \tag{2.35}$$

Clearly, this condition is not satisfied for very slow particles emitted by the sources of a long lifetime. The increasing importance of the non-equal time effect with the decreasing pair velocity is demonstrated in Fig. 2.2 for the strong FSI contribution in the $\pi^0\pi^0$ correlation function. For sufficiently large velocities $v > 0.5$ and radii $r_0 > 1\ fm$, we are interested in, the effect is rather small, not exceeding 5% of the strong FSI contribution in the low-k^* region, corresponding to the effect of several per mille in the correlation function. The effect of non-equal times on the Coulomb FSI contribution into correlation function is very small and can be neglected.

Adopting the equal-time approximation, we can rewrite Equations (2.32) and (2.33) for the production cross section and correlation function as follows

$$\frac{\mathrm{d}^6\sigma}{\mathrm{d}^3\mathbf{p}_1\mathrm{d}^3\mathbf{p}_2} \doteq \frac{\mathrm{d}^6\sigma_0}{\mathrm{d}^3\mathbf{p}_1\mathrm{d}^3\mathbf{p}_2}\sum_S \mathcal{G}_S\langle|\psi^S_{-\mathbf{k}^*}(\mathbf{r}^*)|^2\rangle_{\tilde{q}PS}, \tag{2.36}$$

$$R(p_1,p_2) \doteq \sum_S \mathcal{G}_S\langle|\psi^S_{-\mathbf{k}^*}(\mathbf{r}^*)|^2\rangle_{\tilde{q}PS} \tag{2.37}$$

[2]Note that in high energy collisions, such a model is relevant for a limited rapidity region only. It means that the pair velocity v in the rest frame of the sources is related to the measured velocity rather indirectly

We can roughly estimate $\langle v\rangle$ from the distribution of particle transverse momenta. Taking for pions the $p_\perp^2$-slope of ~ 6 $(\mathrm{GeV/c})^{-2}$ (now we have to account for lower $p_\perp$-values due to indirect pions) and using $\langle v^2\rangle \approx \langle 3p_\perp^2/(3p_\perp^2 + {m_{12}}^2)\rangle$, we get $\langle v\rangle \approx 0.8$.

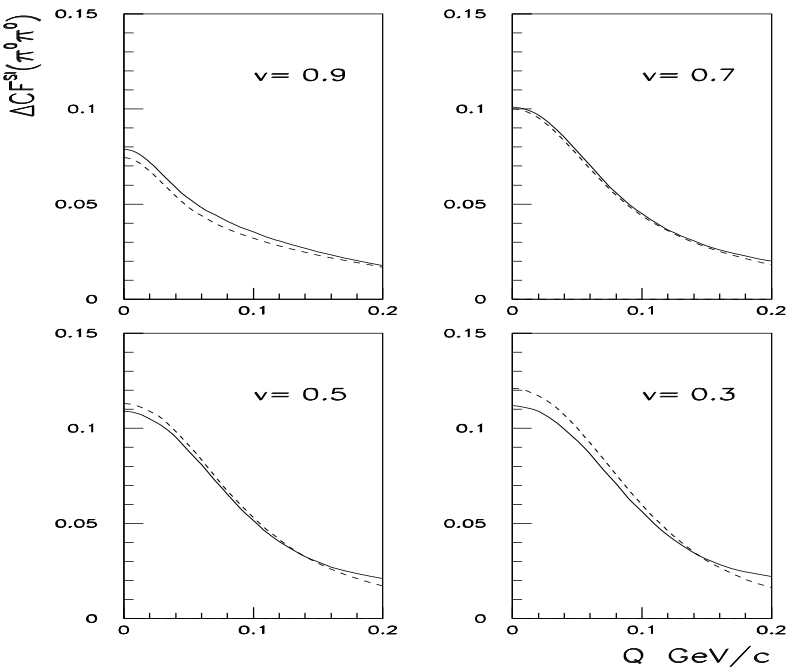

Figure 2.1: The FSI contribution to the $\pi^0\pi^0$ correlation function calculated for different values of the pair velocity v in a Gaussian model of independent one–particle sources with the spatial and time width parameters $\tau_0 = r_0 = 2\ fm$. Solid curves are exact results and dash curves are those obtained in the equal–time approximation.

2.3 Wave function

In this section we will discuss the wave function used in computation of correlation function under smoothness assumption and equal-time approximation (Equation (2.37)). This function corresponds to a stationary solution of an appropriate scattering problem.

2.3.1 Short-range FSI

First we will discuss the case when at least one particle of the pair is neutral, so only strong FSI acts (short-range force). In the considered region of small k^* ($q = 2k^*$) the short–range particle interaction is dominated by s-waves. Since the radius of the s-wave interaction is usually small compared with the distance r^* between the production points of particles of the pair in their c.m.s., the FSI effect is mainly determined by the asymptotic behaviour of the scattered wave

outside the region of the strong interaction $r^* > d$

$$\Delta\psi_{-\mathbf{k}^*}(\mathbf{r}^*) = f(k^*)\mathrm{e}^{ik^*r^*}/r^*. \tag{2.38}$$

The s-wave amplitude f depends only on the magnitude of the vector $\mathbf{k}^*$. Assuming only elastic channel, amplitude f can be represented as

$$f = [\exp(2i\delta_0) - 1]/(2ik^*) = (K^{-1} - ik^*)^{-1}, \tag{2.39}$$

where δ_0 is the s–wave phase shift and $K^{-1} = k^* \cot\delta_0$ is a real function of k^*. Usually (for potentials vanishing with the distance exponentially or faster), this function is real also for negative kinetic energies $k^{*2}/(2\mu)$, (where reduced mass $\mu = m_1 m_2/(m_1 + m_2)$), so that its expansion can contain only even powers of k^* [12]. Retaining near threshold only the first two terms in the expansion, one can express the function K^{-1} or K through the corresponding two parameters, i.e. the scattering length f_0 and the effective range d_0 or curvature b_0

$$K^{-1} \doteq 1/f_0 + \frac{1}{2}d_0 k^{*2}, \quad K \doteq f_0 + b_0 k^{*2}, \quad b_0 \doteq -d_0 {f_0}^2/2. \tag{2.40}$$

The expansion of K^{-1} is superior for two–nucleon systems (due to large scattering lengths, amounting to about 20 fm in the singlet case) while for other systems, the K–expansion is often preferred. To extend the latter to a wider energy range, it is usually written in a relativistic form and additional parameters are added. For example according to [13]

$$K = \frac{2}{\sqrt{s}}\frac{s_{\mathrm{th}} - s_0}{s - s_0}\sum_{j=0}^{3} A_j x^{2j}, \quad x = 2k^*/\sqrt{s_{\mathrm{th}}}, \tag{2.41}$$

where $s = (p_1 + p_2)^2 = (\omega_1^* + \omega_2^*)^2$, $\omega_{1,2}^* = (m_{1,2}^2 + k^{*2})^{1/2}$ and $s_{\mathrm{th}} = (m_1 + m_2)^2$. The parameter s_0 takes into account the eventual resonance, specifying the value of the two–particle c.m.s. energy squared where the phase $\delta_0(k^*)$ passes through 90^o.

Note that the extension of the asymptotic wave function in the inner region of the strong interaction leads to a relative shift in the production cross section of the order $|f|^2 \frac{\mathrm{d}}{\mathrm{d}k^{*2}}\mathrm{Re}(1/f)/\langle r^*\rangle^3$ [7, 11]. The leading part of this shift can be, in principle, corrected for. However, being quadratic in the amplitude f, it is rather small for $\pi\pi$, πK or πp–systems, usually not exceeding several percent of the short–range FSI contribution.

2.3.2 Coulomb FSI

Now we will suppose that both particles are charged, so Coulomb interaction must be considered in addition. Similar to the previous case of neutral particles,

we will approximate (with the same accuracy) the wave function near threshold by the asymptotic solution outside the region of the strong interaction $r^* > d$. The long-range Coulomb interaction modifies not only spherical waves but also the plane wave. The stationary solution can be written in the form [12]

$$\psi_{-\mathbf{k}^*}(\mathbf{r}^*) = \mathrm{e}^{i\delta_c}\sqrt{A_c(\eta)}\left[\mathrm{e}^{-i\mathbf{k}^*\mathbf{r}^*}F(-i\eta,1,i\xi) + f_c(k^*)\frac{\widetilde{G}(\rho,\eta)}{r^*}\right], \qquad (2.42)$$

where $\xi = \mathbf{k}^*\mathbf{r}^* + k^*r^* \equiv \rho(1+\cos\theta^*)$, $\rho = k^*r^*$, $\eta = (k^*a)^{-1}$, $a = (\mu z_1 z_2 e^2)^{-1}$ is the two-particle Bohr radius including the sign of the interaction, $\delta_c = \arg\Gamma(1+i\eta)$ is the Coulomb s-wave phase shift,$A_c(\eta)$ is the Coulomb penetration factor defined as

$$A_c(\eta) = \frac{2\pi\eta}{(\exp(2\pi\eta)-1)}, \qquad (2.43)$$

and

$$F(\alpha,1,z) = 1 + \alpha z/1!^2 + \alpha(\alpha+1)z^2/2!^2 + \cdots \qquad (2.44)$$

is the confluent hyper-geometric function and $\widetilde{G} = \sqrt{A_c}(G_0 + iF_0)$ is a combination of the regular (F_0) and singular (G_0) s–wave Coulomb functions (see, e.g., [14])

$$\widetilde{G}(\rho,\eta) = P(\rho,\eta) + 2\eta\rho\left[\ln|2\eta\rho| + 2C - 1 + \chi(\eta)\right]B(\rho,\eta). \qquad (2.45)$$

Here $C \doteq 0.5772$ is the Euler constant, the functions

$$\begin{aligned} B(\rho,\eta) &= \sum_{s=0}^{\infty} B_s, \quad B_0 = 1, \quad B_1 = \eta\rho, \quad B_2 = (\eta\rho)^2/3 - \rho^2/6, \quad \ldots, \\ P(\rho,\eta) &= \sum_{s=0}^{\infty} P_s, \quad P_0 = 1, \quad P_1 = 0, \quad P_2 = -3(\eta\rho)^2 - \rho^2/2, \quad \ldots \end{aligned} \qquad (2.46)$$

are given by the following recurrence relations[3]

$$\begin{aligned} (n+1)(n+2)B_{n+1} &= 2\eta\rho B_n - \rho^2 B_{n-1}, \\ n(n+1)P_{n+1} &= 2\eta\rho P_n - \rho^2 P_{n-1} - (2n+1)2\eta\rho B_n \end{aligned} \qquad (2.47)$$

and the function

$$\chi(\eta) = h(\eta) + iA_c(\eta)/(2\eta), \qquad (2.48)$$

where the function $h(\eta)$ is expressed through the digamma function $\psi(z) = \Gamma'(z)/\Gamma(z)$

$$h(\eta) = [\psi(i\eta) + \psi(-i\eta) - \ln(\eta^2)]/2. \qquad (2.49)$$

The amplitude $f_c(k^*) = f(k^*)/A_c(\eta)$, where $f(k^*)$ is the amplitude of the low-energy s-wave elastic scattering due to the short–range interaction renormalised

[3]Note that $B(\eta,\rho) \to \sin(\rho)/\rho$ and $P(\eta,\rho) \to \cos(\rho)$ in the limit $\eta\rho \equiv r^*/a \to 0$.

Pair	$\pi^+\pi^\pm$	$\pi^+K^\pm$	$\pi^\pm p$	$K^+K^\pm$	$K^\pm p$	$pp\pm$
a, fm	± 387.5	± 248.6	± 222.5	± 109.6	± 83.6	± 57.6
Q_c, MeV/c	6.4	10.0	11.1	22.6	29.7	43.0

Table 2.1: The Bohr radii of some pairs including the sign of the interaction, $a = (\mu z_1 z_2 e^2)^{-1}$, and the characteristic width of the Coulomb correlation effect, $Q_c \equiv 2k_c^* = 4\pi/|a|$, corresponding to $|\eta|^{-1} = 2\pi$ (see Eq. (2.43)).

by the long–range Coulomb forces. Assuming again the absence of inelastic transitions, the amplitude $f(k^*) = (\mathrm{e}^{2i\delta_0} - 1)/(2ik^*)$ and satisfies the one–channel s–wave unitarity condition. Similar to the case of neutral particles, one then has [12]

$$f_c(k^*) = \left(K^{-1} - \frac{2\chi(\eta)}{a} \right)^{-1}, \tag{2.50}$$

where the function K is real for real kinetic energies, including negative ones (provided the short–range potential vanishes with the distance exponentially or faster), and can be parametrised according to Eqs. (2.40) or (2.41).

Note that $\delta_c \to 0$, $A_c \to 1$ for $\eta \to 0$ ($k^* \gg |a|^{-1}$) and $\widetilde{G} \to \mathrm{e}^{i\rho}$, $F \to 1$ for $\eta\rho \equiv r^*/a \to 0$. So, the two–particle wave function in the absence of the long–range Coulomb forces is recovered provided r^*, f_0 and $1/k^*$ are much smaller than the Bohr radius $|a|$.

In Table 2.1 we list the values of Bohr radii a for the most often studied pairs.

2.4 Bound systems

Production of weakly bound two-particle systems, like deuterons or hadronic atoms ($\pi^+\pi^-$atoms, in particular) can be described in the same manner as the production of two free particles. Due to a low binding energy there is practically no direct production of such bound systems. Their dominant production mechanism is thus due to the particle interaction in the final state.

In analogy to Eq.(2.6) for the production amplitude of free particles $T(p_1, p_2, \alpha)$, the invariant production amplitude $T_b(p_b; S, \alpha')$ of a two–particle bound system with spin S is related to the space time representation $\mathcal{T}$ or τ_p of T_0 and to Bethe-Salpeter amplitude of bound system $\Psi^{S(-)}_{b,p_b}(x_1, x_2) = [\Psi^{S(+)}_{b,p_b}(x_1, x_2)]^* = [\mathrm{e}^{ip_b X}\psi^{S(+)}_b(x)]^*$

$$T_b(p_b; S, \alpha') = \int d^4x_1\, d^4x_2 \Psi^{S(-)}_{b,p_b}(x_1, x_2)\mathcal{T}_0(x_1, x_2; S, \alpha') = \int d^4x \psi^{S(-)}_b(x)\tau_P(x; S, \alpha') \tag{2.51}$$

The corresponding production cross section can be written using two-particle space-time density matrices ρ_S or ρ_{PS} defined by Equation (2.11)

$$(2\pi)^3\gamma_b\frac{d^3\sigma_b^S}{d^3\mathbf{p}_b} = \int d^4x_1\, d^4x_2\, d^4x_1'\, d^4x_2'\rho_S(x_1,x_2;x_1',x_2')\Psi_{b,p_b}^{S(-)}(x_1,x_2)\Psi_{b,p_b}^{S(-)*}(x_1',x_2') =$$

$$= \int d^4x\, d^4x'\rho_{PS}(x;x')\psi_b^{S(-)}(x)\psi_b^{S(-)*}(x') \tag{2.52}$$

and similar to Eq. (2.13), we can also rewrite the formula for production cross section of the bound system through the reference spectrum defined in Eq. (2.12) where $\mathbf{p}_1 \doteq \mathbf{p}_2 \doteq \mathbf{p}_b/2$ and $\gamma_1 \doteq \gamma_2 \doteq \gamma_b$ (i.e. $\widetilde{q} \doteq 0$)

$$\frac{d^3\sigma_b^S}{d^3\mathbf{p}_b} = (2\pi)^3\gamma_b\frac{d^6\sigma_0}{d^3\mathbf{p}_1 d^3\mathbf{p}_2}\mathcal{G}_S(p_1,p_2)\left\langle\Psi_{b,p_b}^{S(-)}(x_1,x_2)\Psi_{b,p_b}^{S(-)*}(x_1',x_2')\right\rangle'_{p_1p_2S} =$$

$$= (2\pi)^3\gamma_b\frac{d^6\sigma_0}{d^3\mathbf{p}_1 d^3\mathbf{p}_2}\mathcal{G}_S(p_1,p_2)\left\langle\psi_b^{S(-)}(x)\psi_b^{S(-)*}(x')\right\rangle'_{0PS}. \tag{2.53}$$

Note, that in case of equal particle emission times in pair c.m.s., the amplitude $\psi_b^{S(-)}(x)$, which describes the relative motion of bound particles, coincides with the usual non-relativistic stationary solution of the two-particle bound system $\psi_b^S(\mathbf{r}^*)$.

Smoothness assumption and equal-time approximation

We can simplify the problem of production of a weakly a bound system in similar way we proceed the problem of two free particles. If the smoothness condition (2.27) is fulfilled, the production cross section can be rewritten into the approximate form using two-particle emission function defined by Eq.(2.20)

$$\begin{aligned}(2\pi)^3\gamma_b\frac{d^3\sigma_b^S}{d^3\mathbf{p}_b} &\doteq \int d^4x_1\, d^4x_2 G_S(x_1,p_1;x_2,p_2)|\psi_b^{S(+)}(x)|^2 = \\ &= \int d^4x\, g_{PS}(x,0)|\psi_b^{S(+)}(x)|^2 \equiv \\ &\equiv (2\pi)^6\gamma_1\gamma_2\frac{d^6\sigma_0}{d^3\mathbf{p}_1 d^3\mathbf{p}_2}\mathcal{G}_S\langle|\psi_b^{S(+)}(x)|^2\rangle_{0PS},\end{aligned} \tag{2.54}$$

where $\mathbf{p}_i = \mathbf{p}_b m_i/(m_1+m_2)$.

In case that condition (2.34) is valid we can use the time-equal approximation which allows us to substitute Bethe-Salpeter amplitude by non-relativistic wave function and in analogy to Eq.(2.36) we can write

$$\gamma_b\frac{d^3\sigma_b^S}{d^3\mathbf{p}_b} \doteq (2\pi)^3\gamma_1\gamma_2\frac{d^6\sigma_0}{d^3\mathbf{p}_1 d^3\mathbf{p}_2}\mathcal{G}_S\langle|\psi_b^S(r^*)|^2\rangle_{0PS}, \tag{2.55}$$

where $b = \{n0\}$ and $\mathbf{p}_i = \mathbf{p}_b m_i/(m_1 + m_2)$; for equal-mass particles are $\mathbf{p}_1 = \mathbf{p}_2 = \mathbf{p}_b/2$ and $\gamma_1 = \gamma_2 = \gamma_b$.

Comparing the Eqs. (2.55) and (2.36) we see that the production of a weakly bound two-particle system is closely related with the production of two particles in continuous spectrum at small relative velocities in their c.m.s.

$$\frac{\left(\frac{d^3\sigma_b^S}{d^3\mathbf{p}_b}\right)}{\left(\frac{\mathrm{d}^6\sigma}{\mathrm{d}^3\mathbf{p}_1\,\mathrm{d}^3\mathbf{p}_2}\right)} \sim \frac{\langle|\psi_b^S(r^*)|^2\rangle_{0PS}}{\langle|\psi_{-\mathbf{k}^*}^S(\mathbf{r}^*)|^2\rangle_{\widetilde{q}PS}}. \tag{2.56}$$

Moreover, since the Schrödinger equation at a small negative energy $-\epsilon_b = -\kappa^2/(2\mu)$ practically coincides with that in continuous spectrum at zero energy, the r^*-dependence of the corresponding wave functions at a given orbital angular momentum l and $r^* \ll \kappa^{-1}$ is the same.

This relation was firstly formulated by A.B. Migdal [15] in connection with the production of non-relativistic deuterons and then generalised [16] to the relativistic case and the inclusive production. Similar relation was obtained, in the limit of an instantaneous emission from a point-like region, also for the case of the production of pure Coulomb hadronic atoms [17]. A complete treatment of the production of weakly bound systems, accounting for the finite-size effects, can be found in Ref. [18].

Chapter 3

Theoretical Background of Experiment

The aim of DIRAC experiment is to measure the lifetime of pionium ($A_{2\pi}$), an atom consisting of π^+ and π^- mesons. The lifetime is dominated by the scattering process $\pi^+\pi^- \to \pi^0\pi^0$ and, therefore it is related to the $\pi\pi$ scattering lengths, allowing to determine them.

3.1 Motivation

Quantum Chromodynamics (QCD) is considered as the elementary theory of strong interaction today. Essentially, it is a perturbation theory with a running coupling constant. Due to an increasing value of the coupling constant with decreasing energy the theory meets some difficulties in the low energy region. The two most widely accepted approaches developed to remedy this problem are the lattice QCD and the Chiral Perturbation Theory (ChPT).

ChPT is an effective theory which provides predictions by forgoing the quark and gluon degrees of freedom in favour of composite hadron interactions. ChPT describes the problem of pion scattering with a high precision. The recent prediction of isoscalar a_0 and isotensor a_2 S-wave $\pi\pi$ scattering lengths including corrections up to two loops are according to [19] [20]

$$a_0 = 0.220 \pm 0.005[m_\pi^{-1}] \quad a_2 = -0.0444 \pm 0.0010[m_\pi^{-1}] \tag{3.1}$$

and their difference

$$a_0 - a_2 = 0.265 \pm 0.004[m_\pi^{-1}]. \tag{3.2}$$

Despite this theoretical computation done with a very high precision there was lack of experimental tests of these values for a long time. At the time of preparation of DIRAC experiment of which the main goal is just to measure the difference $|a_0 - a_2|$ with a 5% accuracy, the experimental value of this difference was known with $\sim$ 20% precision.

The most precise measurement of the scattering lengths has been performed recently by the E865 experiment at Brookhaven Alternating Gradient Synchrotron [21]. A K_{e4} decay branch $K^{\pm} \to \pi^+\pi^- e^{\pm}\nu_e(\bar{\nu}_e)$ was considered and a_0 was obtained

$$a_0 = 0.216 \pm 0.013(stat.) \pm 0.002(syst.) \pm 0.002(theor.). \tag{3.3}$$

In this case, a_0 was determined with 6% precision. During a_0 evaluation the ChPT predictions had to be relied on.

A value of the $\pi\pi$ scattering length a_2 was found in a model-dependent way by an experiment performed at TRIUMF [22], which analysed the process $\pi^+ p \to \pi^+\pi^+ n$ near the production threshold. Pion data were accumulated for several energy values ranging from 172 MeV to 200 MeV and a_2 was found to be

$$a_2 = -0.040 \pm 0.003. \tag{3.4}$$

The latter value was determined with the 7.5% precision and is in agreement with the ChPT prediction mentioned in Eq.(3.1).

Contrary to these experiments DIRAC provides the model independent measurement of $|a_0 - a_2|$ and serves a crucial test of the ChPT predictions.

3.2 Pionium Lifetime

Pionium ($A_{2\pi}$) is an electromagnetically bound system of π^+ and π^- ($\pi^+\pi^-$-atom) with the ground state binding energy $E_b = 1.86keV$ corresponding to Bohr radius $a = 387fm$ and Bohr momentum $p_b = 0.51MeV$. Its existence was firstly confirmed by experiment done in Serpuchov laboratory in 1994 [23]. The lower limit on $A_{2\pi}$ lifetime of $\tau > 1.8 \times 10^{-15}s$ (90% CL) was set up here.

The dominant decay is into $\pi_0\pi_0$ with branching ratio of 99.6%.[1] Thus, the lifetime is dominated by the charge-exchange scattering process $\pi^+\pi^- \to \pi^0\pi^0$ practically on zero energy (due to the small binding energy pions are practically on mass-shell with the very small relative momentum p_b). So the lifetime directly depends on $\pi\pi$ scattering amplitudes a_0 and a_2 and the leading order formula for the $A_{2\pi}$ lifetime in ground state reads [24]

$$\frac{1}{\tau} = \Gamma^{LO}_{A_{2\pi}} = \frac{2}{9}\alpha^3 p^*(a_0 - a_2)^2, \tag{3.5}$$

where α is fine-structure constant ($\sim 1/137$) and

$$p^* = \sqrt{M^2_{\pi^+} - M^2_{\pi^0} - 1/4\alpha^2 M^2_{\pi^+}} \tag{3.6}$$

[1] The other possible decay is into $\gamma\gamma$. Due to a very small probability of this channel it is neglected here.

is the π^0 momentum in the $A_{2\pi}$ rest frame. The lifetimes of higher n states τ_n are connected to the ground state lifetime as:

$$\tau_n = \tau n^3. \tag{3.7}$$

As the lifetime strongly depends on the energy level, the annihilation strongly favours low-n states and occurs only for the states with even orbital quantum numbers l. The strong decays of odd–l states into pairs of identical bosons are forbidden by the conservation of parity.

Applying the Chiral Perturbation theory methods Gasser *et. al.* [25] have taken into account for higher order corrections and obtained the more precise formula for $A_{2\pi}$ ground state lifetime

$$\Gamma_{A_{2\pi}} = \frac{2}{9}\alpha^3 p^*(a_0 - a_2)^2(1 + \delta_\Gamma), \tag{3.8}$$

with[2] $\delta_\Gamma = (5.8 \pm 1.2) \times 10^{-2}$. Combined with (3.2) the theoretical prediction of $A_{2\pi}$ lifetime in ground state is

$$\tau_{1s} = 2.9 \pm 0.1\ fs. \tag{3.9}$$

3.3 Method of Lifetime Measurement

The direct measurement of $A_{2\pi}$ lifetime is due to its very small value practically impossible. Therefore an indirect method based on the determination of $A_{2\pi}$ breakup probability P_{br} is used.

There is a small but finite probability that two oppositely charged pions produced in a primary interaction will create the bound state - $A_{2\pi}$ atom. After its creation pionium flies through the target and can either decay into $\pi^0\pi^0$or interact with atoms of the target and thus be excited or broken-up. The product of this breakup is a $\pi^+\pi^-$pair with very small relative momentum ($q < 3MeV/c$).

The breakup probability P_{br}, defined as a ratio of the numbers of broken-up n_A and produced N_A $A_{2\pi}$ atoms

$$P_{br} = \frac{n_A}{N_A}, \tag{3.10}$$

can be calculated for a given target material and a thickness as a function of the $A_{2\pi}$ momentum and the lifetime. The measurement of P_{br} thus allows to determine the $A_{2\pi}$ lifetime (Fig. 3.1).

Due to very distinct features of $\pi^+\pi^-$pairs from broken-up $A_{2\pi}$ ($Q < 3MeV/c$, opening angle $< 3mrad$), the n_A can be measured from the excess of $\pi^+\pi^-$pairs

[2]To a certain degree, the inclusion of δ_t undermines the claim that the $|a_0 - a_2|$ difference may be obtained from the lifetime in a model-independent way. However, this correction amounts to a 6% change in the decay width in Eq. (3.5).

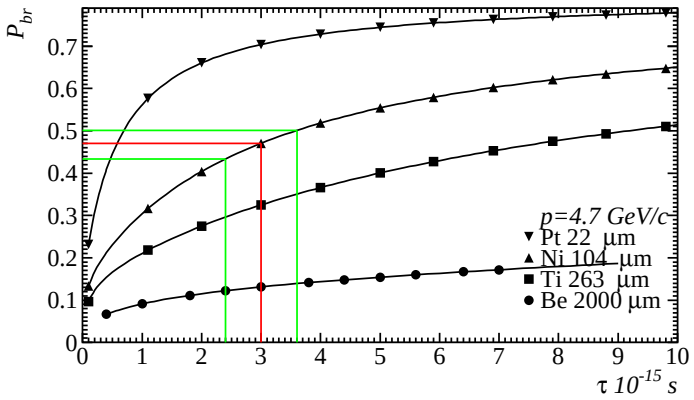

Figure 3.1: Probability of $A_{2\pi}$ breakup P_{br} in the target as a function of $A_{2\pi}$ lifetime

at very small relative momentum. As for N_A, it can be calculated using the relation between the two-pion production in continuous (free pions) and discrete (bound pions) spectrum.

3.3.1 Production of $A_{2\pi}$

Since $A_{2\pi}$ is weakly bound system its production can be described according to Section 2.4. In the following let us first neglect the strong FSI. Pions emerging from a high energy proton-nucleus collision may be either produced directly or stem from strong decays ("short-lived" sources like ρ or Δ resonances) and electromagnetic or weak decays ("long-lived" sources like η, Λ or K).

The typical distance between emission points of pion pairs produced directly or from short-lived sources is on level of several fm while for pairs from long-lived sources this distance is very large. Since the relative space-time distance between the emission points x enters in the $\pi^+\pi^-$ pure Coulomb amplitudes $\psi_q^{(-)\mathrm{coul}}(x)$ and $\psi_b^{(-)\mathrm{coul}}(x)$ scaled by the Bohr radius $a = 387.5fm$, one can put in Eqs. (2.36) and (2.55) $\psi_{-\mathbf{k}^*}(x) \approx \mathrm{e}^{-i\mathbf{k}^*\mathbf{r}^*}|\psi^{\mathrm{coul}}_{-\mathbf{k}^*}(0)|$ and $\psi_b(x) \approx \psi_b^{\mathrm{coul}}(0)$ for the fraction λ of the pairs with both pions from short-lived sources, and $\psi_{-\mathbf{k}^*}(x) \approx \mathrm{e}^{-i\tilde{q}x/2}$ and $\psi_b(x) \approx \psi_b^{\mathrm{coul}}(\infty) = 0$ for the remaining fraction $(1-\lambda)$, respectively. As a result, Eqs. (2.36) and (2.55) reduce to

$$\frac{d^6\sigma}{d^3\mathbf{p}_1 d^3\mathbf{p}_2} \approx \frac{d^6\sigma_0}{d^3\mathbf{p}_1 d^3\mathbf{p}_2} g[\lambda|\psi^{\mathrm{coul}}_{-\mathbf{k}^*}(0)|^2 + (1-\lambda)], \tag{3.11}$$

$$\frac{d^3\sigma}{d^3\mathbf{p}_b} \approx (2\pi)^3\gamma_b \frac{d^6\sigma_0}{d^3\mathbf{p}_1 d^3\mathbf{p}_2} g\lambda|\psi_b^{\mathrm{coul}}(0)|^2, \tag{3.12}$$

where σ_0 represents the production cross section of pions without influence of FSI and g is a normalisation parameter. The expression for the production of bound $\pi^+\pi^-$ system implies $\mathbf{p}_1 \doteq \mathbf{p}_2 \doteq \mathbf{p}_b/2$ and $\gamma_1 \doteq \gamma_2 \doteq \gamma_b$.

The squares of the non-relativistic Coulomb wave functions at zero separation are

$$|\psi^{\rm coul}_{-\mathbf{k}^*}(0)|^2 = A_c(\eta), \quad \eta = (k^* a)^{-1}, \tag{3.13}$$

$$|\psi^{\rm coul}_{b}(0)|^2 = \delta_{l0}(\pi|a|^3 n^3)^{-1}. \tag{3.14}$$

Here $a = -(\mu e^2)^{-1} = -387.5$ fm is the Bohr radius accounting for the opposite signs of the pion charges. $A_c(\eta)$ is Coulomb penetration factor (also called Gammov-Sommerfeld factor) defined by Eg. (2.43). The production of free $\pi^+\pi^-$pairs is enhanced at small $q = 2k^*$ as $4\pi/(|a|q)$ and at large q it approaches unity as $1 + 2\pi/(|a|q)$.

In this approach the pairs of two free pions, both produced directly or from short-lived source, undergo Coulomb FSI and therefor they are further called Coulomb pairs. The rest of free pairs is not influenced by Coulomb FSI and that is why they are called non-Coulomb pairs.

As for the bound $\pi^+\pi^-$ pairs $b = \{nl\}$, at zero separation they are produced only in the s-wave states $\{n0\}$ and the fractions with given main quantum numbers n are uniquely fixed by the n^{-3} law in Eq. (3.14).

From formulae (3.11) and (3.12) we see a clear relation between the number of produced $A_{2\pi}$ atoms N_A and the Coulomb pairs N_{CC} for low q, $0 \le q \le q_0$. We can define a theoretical k-factor

$$k_{th}(q_0) \equiv \frac{N_A}{N_{CC}} = \frac{(2\pi\alpha m_\pi)^3}{\pi} \frac{\sum\limits_{n=1}^{\infty} \frac{1}{n^3}}{\int\limits_0^{\eta(q_0)} A_C(\eta) d^3\eta} \tag{3.15}$$

which equals to 0.615 for $q_0 = 2MeV/c$.

In order to account for the finite size of the pion production region and of the two-pion strong FSI, the squares of the Coulomb wave functions in Eqs. (3.11) and (3.12) must be substituted by the square of the complete wave functions, averaged over the distance $\mathbf{r}^*$.[3] Formally we can write

$$\frac{\mathrm{d}^6\sigma}{\mathrm{d}^3\mathbf{p}_1\mathrm{d}^3\mathbf{p}_2} \doteq \frac{\mathrm{d}^6\sigma_0}{\mathrm{d}^3\mathbf{p}_1\mathrm{d}^3\mathbf{p}_2}\{\lambda[1+\delta(\mathbf{k}^*)]A_c(\eta) + (1-\lambda)\}, \tag{3.16}$$

$$\frac{\mathrm{d}^3\sigma}{\mathrm{d}^3\mathbf{p}_b} \doteq (2\pi)^3\gamma_b \frac{\mathrm{d}^3\sigma_0}{\mathrm{d}^3\mathbf{p}_1\mathrm{d}^3\mathbf{p}_2}\lambda(1+\delta_b)|\psi^{\rm coul}_b(0)|^2, \tag{3.17}$$

where

$$1 + \delta(\mathbf{k}^*) \doteq \left\langle |\psi^{\rm coul}_{-\mathbf{k}^*}(r^*)|^2 \right\rangle^{\rm SLS}_{\widetilde{q}P} / A_c(\eta), \tag{3.18}$$

$$1 + \delta_b \doteq \left\langle |\psi^{\rm coul}_{b}(r^*)|^2 \right\rangle^{\rm SLS}_{0P} / |\psi^{\rm coul}_{b}(0)|^2. \tag{3.19}$$

[3] In addition, we should include processes $\pi^0\pi^0 \to A_{2\pi}$ as well as $\pi^0\pi^0 \to \pi^+\pi^-$ but their contribution is small and is neglected here. See [26], Section 7 for the complete treatment.

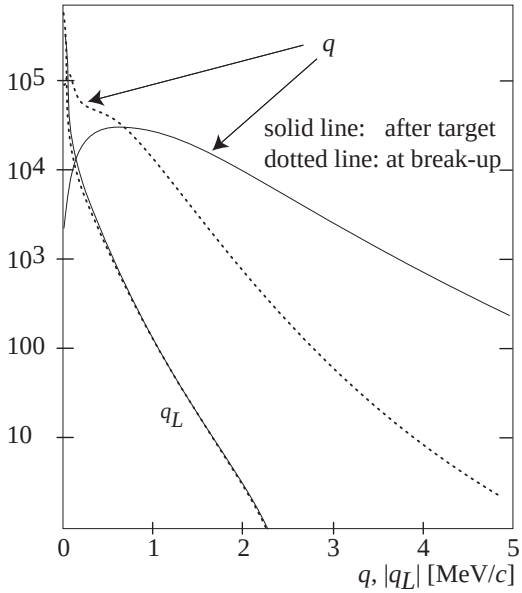

Figure 3.2: Relative momentum distributions (q, q_L) for atomic $\pi^+\pi^-$pairs at the point of break-up and at the exit of the target. Note that q_L is almost not affected by multiple scattering in the target.

The averaging is done over r^*–distribution related to the short–lived sources (SLS). According to Migdal's argument [15], we can put [27]

$$\delta_b \doteq \delta(0) \tag{3.20}$$

provided the characteristic distance of the pion short-lived sources is much less than the two-pion Bohr radius $|a|$.

Adopting the Eq. (3.20) we can conclude that these corrections basically cancel in the k-factor (Eq. (3.15)) for small q_0. Thus finite size and strong FSI correction can be neglected for k_{th} up to a correction of only a fraction of a percent [26].

3.3.2 Propagation of $A_{2\pi}$ through target

Once produced, the $A_{2\pi}$ atoms propagate with relativistic velocity (average Lorentz factor $\gamma \sim 17$ under DIRAC experiment condition) through the target and can either interact, mainly electromagnetically, with atoms of the target or annihilate into $\pi^0\pi^0$. During interaction with target atoms, $A_{2\pi}$ can be excited or de-excited into higher or lower n-state or broken up into free pair $\pi^+\pi^-$(atomic pairs). This pairs exhibit specific kinematic features [17] which allow to identify them experimentally, namely at very low relative momenta q and q_L (the component of $\vec{q}$ parallel to the total pair momentum $\mathbf{P}$) as show in Fig. 3.2

The evolution scenario of $A_{2\pi}$ in the target has been modelled using relativistic atomic transport equation and Glauber and Born scattering cross-sections. An atom was propagated through a series of discrete steps, where at the end of each step the atom's evolution is decided based on the following expressions for the probabilities per unit length:

$$P_{anh} = \frac{1}{\lambda^{anh}_{nlm}} = \begin{array}{ll} \frac{2M_\pi}{p_\pi n^3 \tau} & ,l = 0 \\ 0 & ,l \neq 0 \end{array}$$

$$P_{dsc} = \frac{\sigma^{n'l'm'}_{nlm} \rho N_0}{A}$$

$$P_{br} = \frac{\sigma^{\infty}_{nlm} \rho N_0}{A}, \tag{3.21}$$

where $\sigma^{n'l'm'}_{nlm}$ and σ^{∞}_{nlm} are excitation (de-excitation) and breakup cross-sections, respectively, ρ is the target density, A the atomic number of the target material, N_0 is the Avogadro's number, λ^{anh}_{nlm} is the mean free path for annihilation and p_π is the $A_{2\pi}$ laboratory momentum.

For the ChPT lifetime prediction of $2.9 fs$ the simulated P_{br} for a $95 \mu m$ Ni target corresponds to 45% with precision of 1% [28].

3.3.3 P_{br} determination

In order to evaluate the break-up probability P_{br}, the total number of produced $A_{2\pi}$ atoms N_A and the total number n_A of atomic pairs from broken-up $A_{2\pi}$ must be determined. None of them are directly measurable. They are extracted from the measured q and q_L, respective, spectra of $\pi^+\pi^-$pairs.[4]

Two distribution of q and q_l are measured: **prompt** and **accidental**, respectively. Into the first one only pairs of simultaneously created pions ($|\Delta t| < 0.5ns$) contribute. The second one consist of pairs where each pion was produced in different primary interaction (and different times $|\Delta t| > 5ns$). Hence they are uncorrelated and can serve as a reference spectrum not influenced by FSI ($\sim \frac{d^6\sigma_0}{d^3p_1 d^3p_2}$). The prompt distribution comprises of atomic, Coulomb, non-Coulomb and some admixture of accidentals pairs (See Table (3.1) for their classification).

Note that due to a different kinematics condition for creation of accidental and prompt pairs the accidentals must be corrected to get reference spectrum [29].

The method of determination of N_A and n_a is the following. First, the contribution of accidental pairs in the prompt distribution is subtracted. This clean prompt spectrum is fitted using formula Eg.(3.11) where the cross-section $\frac{d^6\sigma_0}{d^3p_1 d^3p_2}$

[4]The q distribution of $\pi^+\pi^-$pairs is affected by multiple scattering in target, mainly in transverse direction, while q_L is almost not influenced (Fig. (3.2)). Thus the analysis is done independently for both spectra and final results are compared.

Pion Pair Type	Origin
Atomic pairs	Breakup-ed $A_{2\pi}$ atoms. Atoms originated only from pairs where both pions are produced directly or from short-lived sources
Coulomb pairs	Both pions are created directly or from short-lived sources
Non-Coulomb pairs	At least one pion come from a long-lived source
Accidental pairs	Pions created in two separated primary interaction

Table 3.1: Classification of pairs by their origin

is substituted by corrected measured distribution of accidentals $\frac{d^6 N_{acc}^{corr}}{d^3p_1 d^3p_2}$. This fit is done for $q > 4MeV/c$ in the area where the atomic pairs are absent. The fitted function is extrapolated into the region of $q < 4MeV/c$ and the excess of measured distribution over this function determines the number n'_A of observed atomic pairs. This function brings at once information about contribution of Coulomb ($\sim \lambda A_c(\eta)$) and non-Coulomb ($\sim (1-\lambda)$) pairs into this q-region. So we can determine the number of detected Coulomb pairs n'_{CC}.

From the full Monte-Carlo simulation of detector response the efficiencies of detection for Coulomb ϵ_{CC} and atomic ϵ_A pairs are determined. The total number of atomic pairs is then $n_A = n'_A/\epsilon_A$. To obtain the total number of produced $A_{2\pi}$ atoms we use the relation (3.15) between number of Coulomb pairs and $A_{2\pi}$ atoms and we get $N_A = k_{th}(q)n'_{CC}/\epsilon_{CC}$. The breakup probability is given by

$$P_{br} = \frac{n_A}{N_A} = \frac{1}{k_{th}(q)} \frac{\epsilon_{CC}}{\epsilon_A} \frac{n'_A}{n'_{CC}} \tag{3.22}$$

Let us remind that here we used assumption of production of Coulomb pairs with spatial separation $r^* \ll |a|$ and non-Coulomb pairs with separation $r^* \gg |a|$. This approach is violated for pion pairs containing pions from decays of some resonances such as ω and η' with the path lengths of about 30 and 900 fm, respectively. While their influence practically cancels in $k-th$-factor, the correction due to this effect in n'_A and n'_{CC} can be up to several percent. The study of the influence of finite size of production region is the subject of this work.

Chapter 4

DIRAC apparatus

The DIRAC experimental setup is designed for precise measurement of $\pi^+\pi^-$pairs with very low relative momentum. After a calibration at the end of 1998 DIRAC has been collecting data since summer 1999. A detailed description of DIRAC double arm spectrometer is published in [30].

4.1 General layout description

The DIRAC apparatus is located at the T8 proton beam line of 24 GeV/c momentum in East Hall of the PS accelerator at CERN.

It is designed like double–arm spectrometer with crucial task to detect close $\pi^+\pi^-$ pairs with high resolution over the pair relative momentum. The main parts of setup are proton beam line, target station, secondary particle vacuum channel, spectrometer magnet and detectors placed upstream and downstream to the magnet. A top view of DIRAC setup with the indication of the various detector can be seen on Figure 4.1 while Figure 4.2 shows a side view.

The secondary channel is arranged at an angle 5.7° upwards with respect to the proton beam. The horizontal and vertical acceptance of the channel is $\pm 1°$. The upstream part is instrumented with the following detectors: microstrip gas chambers (MSGC), scintillating fibre detector (SFD) and scintillation ionisation hodoscope (IH). The downstream part consists of two identical arms along which are these detectors: drift chambers (DC), vertical (VH) and horizontal (HH) hodoscope, Čerenkov counter (CH), preshower detector (PSH) and muon detector (MU). The arms are deflected from spectrometer axis by 19° to opposite sides in order to detect positive and negative charged particles.

4.2 Beam lines, target station and magnet

The protons are extracted from PS to T8 beam line in spills with duration of $\approx 400 - 500ms$ using a slow ejection mode. During data taking from 1 to 5

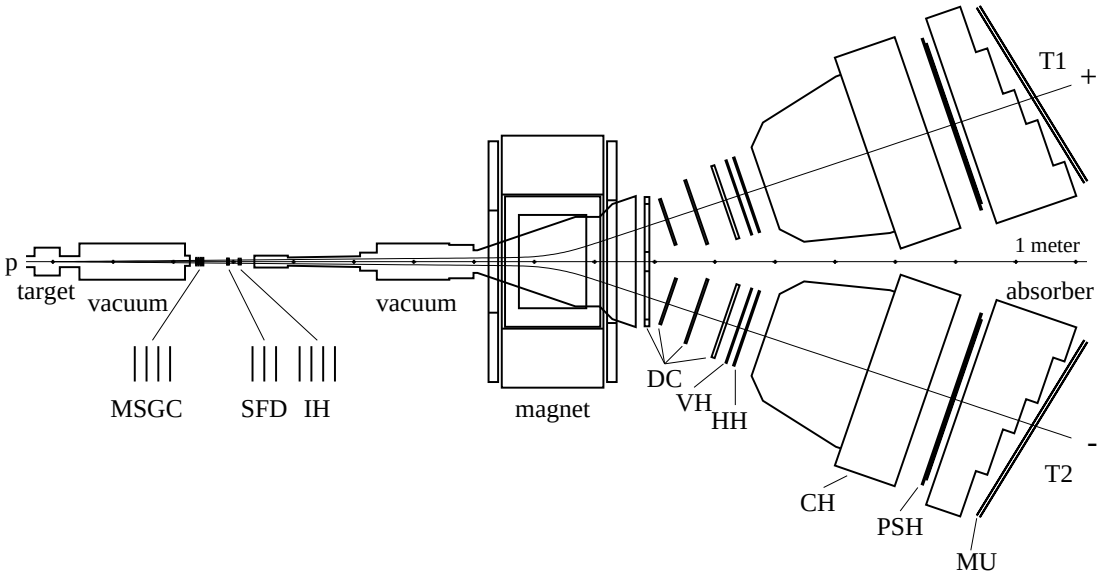

Figure 4.1: Schematic top view of the DIRAC spectrometer. Moving from the target station towards the magnet there are 4 planes of microstrip gas chambers (GEM/MSGC), 3 planes of scintillating fibre detectors (SFD) and 4 planes of ionisation hodoscope (IH). Downstream the dipole magnet, on each arm of the spectrometer, there are 4 stations of drift chambers (DC), vertical and horizontal scintillation hodoscopes (VH, HH), gas Čerenkov counter (CH), preshower detector (PSH) and, behind the iron absorber, muon detector (MU).

spills are delivered to DIRAC experiment per one PS super-cycle of $14 - 19s$ duration. The obvious intensity is $\sim 1 \times 10^{11}$ proton per spill for Ni target. The dimension of beam spot at the target location is in vertical direction $x = 1.6mm$ and horizontal one $y = 3.2mm$ at 2σ level.

After passing the target station the primary beam continues in a vacuum line below the spectrometer into a beam dump. Both the line and the beam dump are equipped by an appropriate shielding to decrease background in the apparatus. (The detector's counting rates are $\sim$ 25 times higher when a target is in place than with the target out of place.)

The vacuum target station houses a device with 12 holders for targets which can be remotely changed. During data taking targets made of Pt ($28\mu m$ thick), Ni (94 and $98\mu m$ thick) and Ti ($250\mu m$ thick) were used.

The secondary channel is declined at an angle 5.7° upwards with respect to the primary proton beam. It extends vacuum part from the target through the magnet up to the drift chambers with an open air gap of $\sim 1.5m$ length which allows to insert the upstream detectors (see Figure 4.1).

The dipole spectrometer magnet is placed at $8.5m$ distance from target and

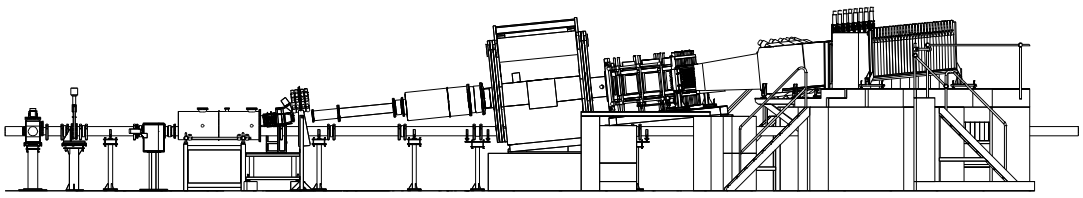

Figure 4.2: Side view of the DIRAC setup. The secondary particle channel is inclined by 5.7° with respect to the primary proton beam.

has an aperture $1.55 \times 0.50 m^2$ ($W \times H$). The applied magnetic field $B = 1.65T$ ($BL = 2.2Tm$) splits the positive and negative charged particles into the opposite arms and allows the measurement of their momenta. The magnetic field was carefully measured and parametrised to allow precise reconstruction of tracks of particles with different momenta, see [31].

4.3 Upstream detectors

The upstream detectors are placed close to the target. Their main task is a precision measurement of close particle tracks with high detection rate and efficiency. It is important for a sharp determination of pairs relative momenta. These detectors are also used in high levels of the trigger.

4.3.1 MSGC detector

The Micro Strip Gas Chamber detector is placed at a distance of $2.4m$ from the interaction point. It is a proportional gas detector based on the principle of Gas Electron Amplifier complemented with the second amplification and readout provided by Micro Strip Gas Chambers. The schematic view is shown on Figure 4.3. It is the first usage of this type of detector in a real experiment.

The detector consists of four independent subdetectors which allow to measure particle coordinates in four orientations 0°, 90°, 5°, 85° with respect to vertical line. The average efficiency of particle detection by one plane of $10.24 \times 10.24 cm^2$ active area is 93%. This yields efficiency of 75% for all four planes required for a track reconstruction. Although a single hit resolution is $54\mu m$, a double track resolution for close-lying tracks falls down to and is of the order of 500 to $700\mu m$. The time resolution amounts approximately to $200ns$.

The complete setup of the detector has been placed on from year 2001 with a typical "off-time" about 40%.

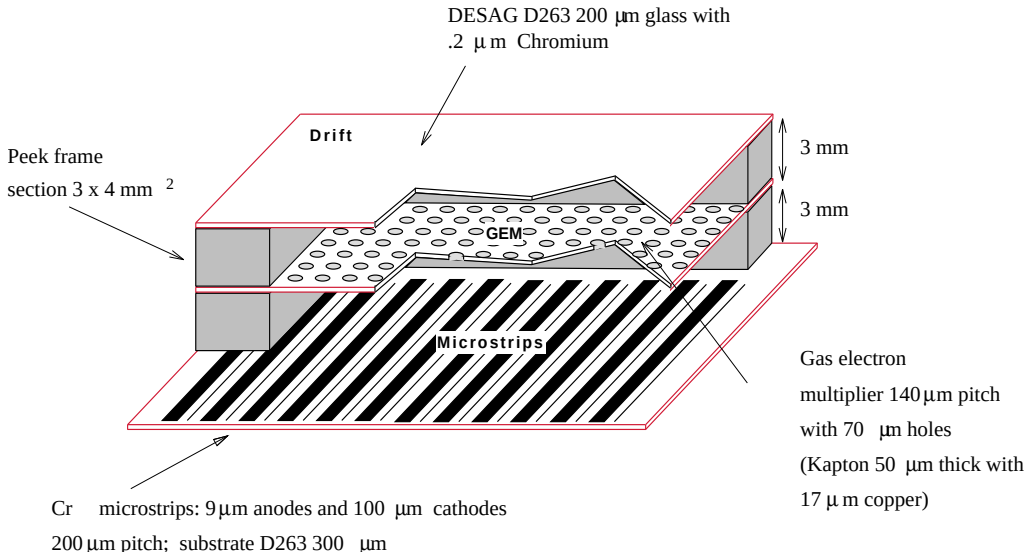

Figure 4.3: Layout of the MSGC detector.

4.3.2 Scintillation Fibre Detector

The Scintillation Fibre Detector enables to perform tracking upstream to the magnet and triggering. It is placed at a distance of $2.95m$ from the target and covers an active area of $105 \times 105mm^2$. Originally, it consisted of two planes (X and Y) which measured track coordinates in two perpendicular directions. In 2002 the third one (U) was added. It allows to measure track coordinates in the direction inclined by an angle 45° from X and Y direction. This significantly improves the track-finding mechanism in the upstream region.

Each of X and Y planes has 240 sensitive columns. One column is composed from five scintillating KURARAY fibres (SciFi) with length of $130mm$ and diameter of $0.50mm$. Each fibre is connected to a clear light guide of $\sim 300mm$ length. The edges of clear fibres belonging to one column are assembled in a bundle and carefully polished and glued into holes of a square black plate which fixes the fibres endings on the position sensitive photomultiplier (PSPM). In total there are 16 channels per PSPM (Hamamatsu H6568) and 15 PSPM to yield all the 240 channels per one plane. The level of optical cross-talk among PSPM channels was measured to be of the order of 1%. The pitch of one sensitive column is $0.44mm$ and the thickness of one plane is about $\sim 2mm$.

U plane, in contrast to X and Y planes, consists of only three layers of scintillating fibres with a little bit higher diameter of $0.57mm$. There is 320 active columns in 5 sections of different fibre lengths ($150, 130$ and $70mm$) to cover roughly the same sensitive area like X and Y planes.

A layout illustrating the main characteristics of SFD planes is shown on Fig-

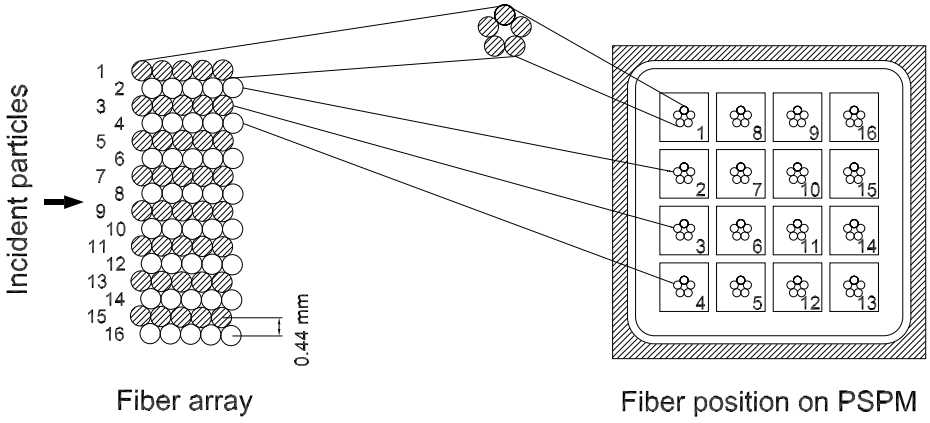

Figure 4.4: The SFD principal structure. A 16-channel fragment is shown.

ure 4.4.

The readout electronics contains a dedicated peak sensing circuit (PSC) which provides a signal discrimination and a dynamic rejection of cross-talk in adjacent channels. The PSC discriminates the signal according to the condition

$$2A_i - A_{i-1} - A_{i+1} > A_{thr},$$

where A_i, A_{i-1} and A_{i+1} are signal amplitudes and A_{thr} defines the threshold value. For time correlated (time difference $\delta t < 5ns$) two tracks with a relative distance larger than one column pitch the PSC successfully eliminates unwanted cross-talk. However, if two adjacent sensitive columns are crossed by two particles simultaneously, PSC algorithm suppresses one hit with a probability of about 50%. In such case the signature from double track event cannot be distinguished from a single track events using SFD detector alone. The distinction between the single track events and close-lying double track events can partly be remedied using the ionisation hodoscope (IH) signal, since double track events deposit on average more energy in IH than single track events. For double track events with relative time difference greater than $5ns$ PSC behaves as an ordinary leading edge discriminator. The inefficiencies due to the PSC and PSC time-correlation ware studied in [32]. The detailed description of PSC can be found in [33].

SFD performance is influenced by the high flux of particles at the position of detector near the interaction point and by a non-negligible amount of scattered particles crossing detector side ward. The one track inefficiency is estimated to be 5%, for double ionization events with two tracks requirement the efficiency is about 91% [32]. The time resolution was found to be $0.8ns$ and the space resolution is equivalent to pitch of sensitive column $440\mu m$. Double track resolution is distorted for close-lying track due to PSC behaviour.

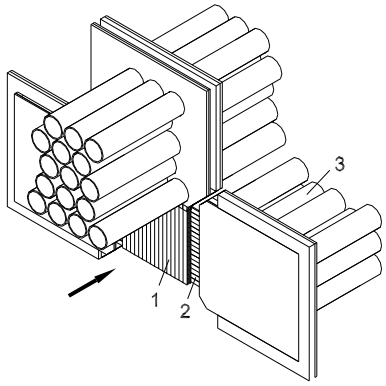

Figure 4.5: Isometric view of the Ionisation Hodoscope. 1 – scintillators, 2 – light-guides, 3 – photomultipliers with shielding.

4.3.3 Ionisation Hodoscope

For DIRAC experiment the measurement of close tracks is crucial. From the above discussion about SFD detector it is clear that SFD does not fulfil this task sufficiently. To solve this problem the technique based on a measurement of ionisation losses is used as well. Dedicated Ionisation Hodoscope (IH) has been built to separate single track hits from double close-lying tracks by means of their ionisation losses.

The present IH detector was installed in 2001 to replace old one. It is placed at a distance of $3.05m$ from the target and covers a sensitive area of $11 \times 11cm^2$. It consists of four planes, two with slabs oriented in X direction, two in Y. Each plane is assembled from 16 plastic scintillating slabs of $11cm$ length, $7mm$ width and $1mm$ thickness. (The old detector was of a similar design but only with two planes and a slab thickness of $2mm$.) Planes with the same slab orientation are shifted by the half slab width with respect to each other. Each slab is connected to one photomultiplier photo–cathode (FEU-85) via $2mm$ thick and $7mm$ wide Lucite light guide. The nonsensitive gap between slabs is less then $70\mu m$ wide. Figure 4.5 shows isometric view of IH detector.

The ADC and TDC signals of IH are read out and are available during the off-line analysis. The ADC spectra for single and double ionisation events are shown in Figure 4.6. If the threshold is set to retain 95% of double ionisation signal, the contamination of single particle amplitudes is less than 15%. The time resolution of IH is better than $1ns$.

4.4 Downstream detectors

The downstream detectors form two arms of DIRAC spectrometer, which are deflected from the axis of the secondary channel by 19° to opposite sides. The

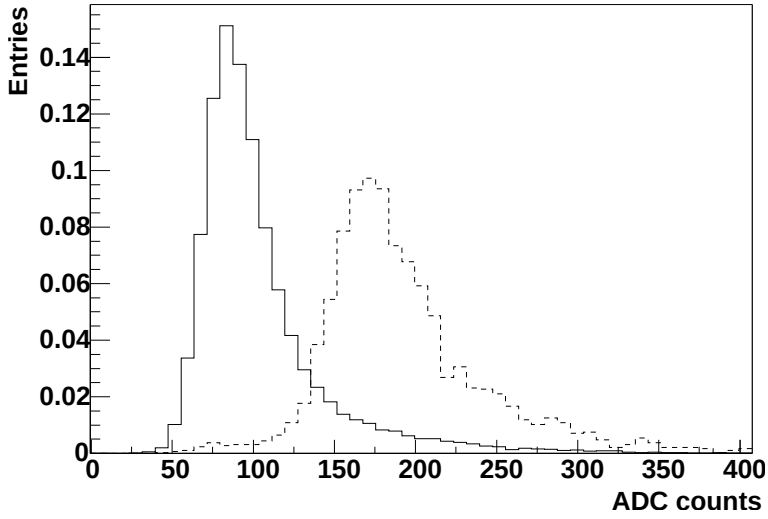

Figure 4.6: Typical ADC spectra for single (solid line) and double (dashed line) ionisation loss from particles crossing one IH scintillating slab.

detectors fulfil several tasks: the measurement of space parameters of track after magnet (DC), identification of electrons and muons (CH,PSH and MU) and fast triggering and time measurement (VH and HH).

4.4.1 Drift Chambers

The drift chambers system is used to perform particle tracking downstream the spectrometer magnet. It is designed to sustain high particle fluency up to $10kHz/cm^2$. It is formed by seven independent modules, three in each arm (DC-2, DC-3 and DC-4) and one common for both arms (DC-1).

The largest module DC-1 is placed close to the spectrometer magnet and houses two separated sensitive areas of $0.4 \times 0.8\ m^2$ each. This chamber provides six successive measurements of the particle trajectory along the coordinates X,Y,W,X,Y,W, where W denotes a measurement along direction inclined 11.3° with respect to the X. It is instrumented by 800 electronic channels.

Each of the arms is further equipped with three chambers, performing the measurements of X, Y (DC-2), X, Y (DC-3) and X, Y, X, Y (DC-4) coordinates of tracks. Their sensitives areas are $.40 \times .80\ m^2$ (DC-2), $0.40 \times 1.12\ m^2$ (DC-3) and $.40 \times 1.28\ m^2$ (DC-4). Both arms contain together 1216 electronic channels. The main characteristic of DC modules are summarised in Table 4.1

A schematic drawing of the sensitive element is shown in Figure 4.7. The anode wires pitch is $10mm$, the distance between the anode and cathode planes is $5mm$. The cathode planes and potential wires are at equal voltages. The sensitive area, corresponding to each anode wire and limited by cathode planes

Module	Sensitive area $[cm^2]$	Number of channels	Measured coordinate	Number of planes
DC-1	40×80	400	X	2+2
	+	+	Y	2+2
	40×80	400	W	2+2
DC-2	40×80	120	X	1
			Y	1
DC-3	40×112	152	X	1
			Y	1
DC-4	40×128	336	X	2
			Y	2

Table 4.1: General properties of DC modules

and potential wires, has a square shape area of $10 \times 10\ mm^2$. In this configuration with, a suitable gas mixture it is possible to achieve a linear behaviour of the drift function except of a small region near potential wires.

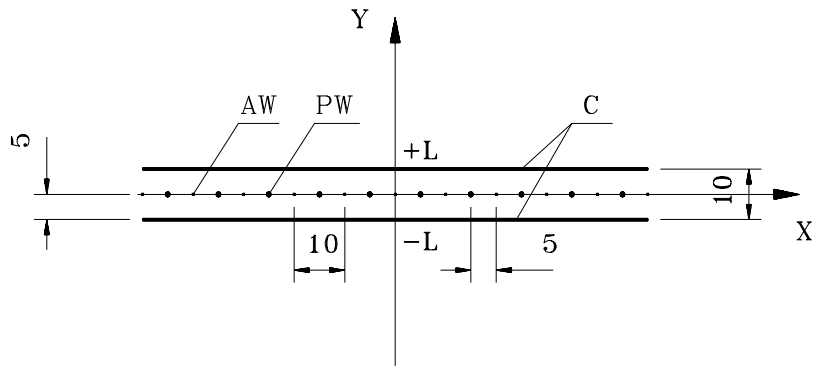

Figure 4.7: Schematic view of the wire chamber electrodes: AW – anode wires, PW – potential wires, C – cathode foils. Dimensions are in mm.

Cathode planes are made of 20 μm thick carbon-coated mylar foils with surface resistivity of about 400 Ω/m^2. This solution provides stable chamber operation due to a high work function of carbon coating together with a small amount of material added along the particle path.

Anode and potential wires of 50 and 100 μm diameter, respectively, are made of a copper-beryllium alloy. The rather large diameter of the anode wires has been chosen in order to operate the chambers at high current avalanche amplification mode.

The employed gas mixture is $Ar(\sim 50\%) + iC_4H_{10}(\sim 50\%) + H_2(0.5\%)$ and the chamber operation voltage is 3.85 kV.

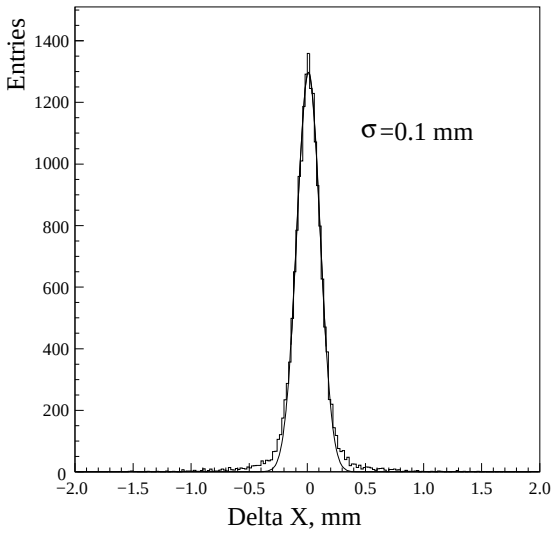

Figure 4.8: Distribution of differences between the measured and predicted X-coordinate for one drift chamber plane ($X4$).

The DC electronics is a custom-made system [34] which provides read-out into the data collecting memories and input to the trigger processor. It consists of TDCs, which are mounted onto the chamber frames, bus drivers, read-out controllers and VME memories. The accepted data are transferred to the VME buffers within 5 μs on average.

Coordinate resolution of the DC system is demonstrated in Fig 4.8, where the distribution of differences between the predicted position and measured coordinates in one of the planes is shown. The measured standard deviation $\sigma = 100$ μm is defined not only by intrinsic chamber plane resolution but also by the accuracy of the predicted track coordinates. Taking the latter into account the intrinsic space resolution of one plane is better than 90 μm.

The average track efficiency of one chamber is about 97%. The track efficiency of the DC system as a whole is about 99%, due to the redundancy of the measurement.

4.4.2 Vertical Hodoscope

Vertical Hodoscope is designed to achieve very high time resolution to be able to distinguish between the particle pairs from one primary proton interaction and the particles produced at two different primary interactions. Furthermore, it is used in cooperation with other detectors in several levels of the trigger system.

Two VH telescopes are placed at a distance of 11.6 m from target, one per arm (VH1 and VH2). With the sensitive area 0.4×1.3 m^2 they are matching the acceptance of DC. Each of the telescopes consists of 18 vertical scintillation

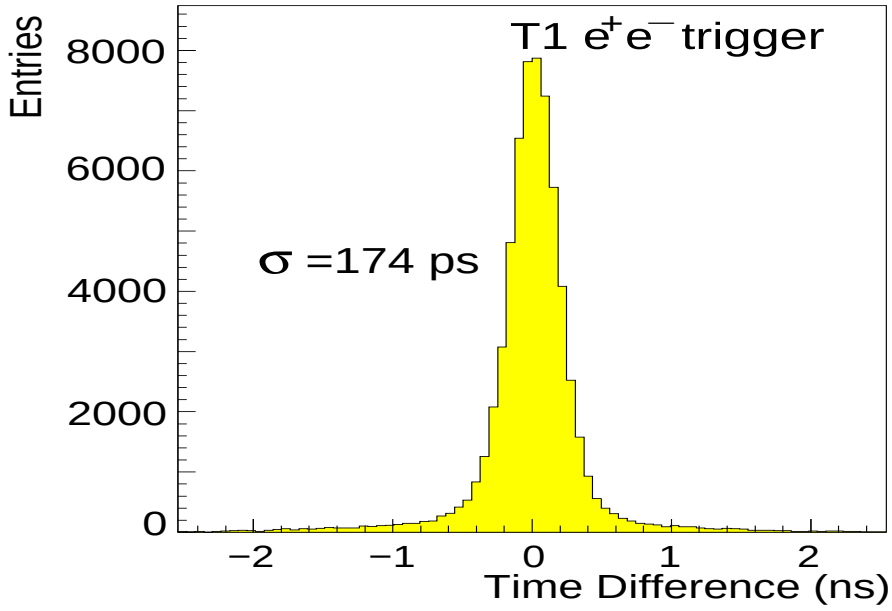

Figure 4.9: Time difference spectrum for e^+e^- pairs detected by the Vertical Hodoscope, after path length correction. Data come from a sample of e^+e^- calibration triggers.

counters made from BICRON BC420 with dimensions of 40 cm length, 7 cm width and 2.2 cm thickness. Scintillation light is collected at both ends of slab by two photomultipliers (Hamamatsu R1828-01). Voltage dividers are designed to operate at particle rates up to 2 MHz without any degradation of the time resolution. The front-end electronics use LeCroy L3420 constant fraction discriminators followed by CAEN C561 meantimers to provide a position independent time measurement. After appropriate delay the signal is treated by TDC system with the least count of $62ps$.

The detection efficiency of telescopes is slightly different, for positive arm it is 99.5% and for negative one 98.8%

The time resolution of VH was measured using e^+e^- pairs created in γ conversion or Dalitz decay of π^0. This pairs are almost synchronous in time, as the time of flight is momentum independent in the available momentum acceptance region. Figure 4.9 shows the time difference distribution of detection of these electron pairs as measured by VH telescopes in opposite arms and corrected on different paths of flight. The fitted width of distribution $\sigma = 174ps$ corresponds to intrinsic an time resolution of one slab $\sigma = 127ps$.

The time differences for events with pion flag is demonstrated in Figure 4.10. The central peak of time correlated pions (prompt events) has a width $\sigma = 193ps$. The flat background is composed of time uncorrelated pairs (accidental pairs), which do not originate in one primary beam interaction. The shoulder on the

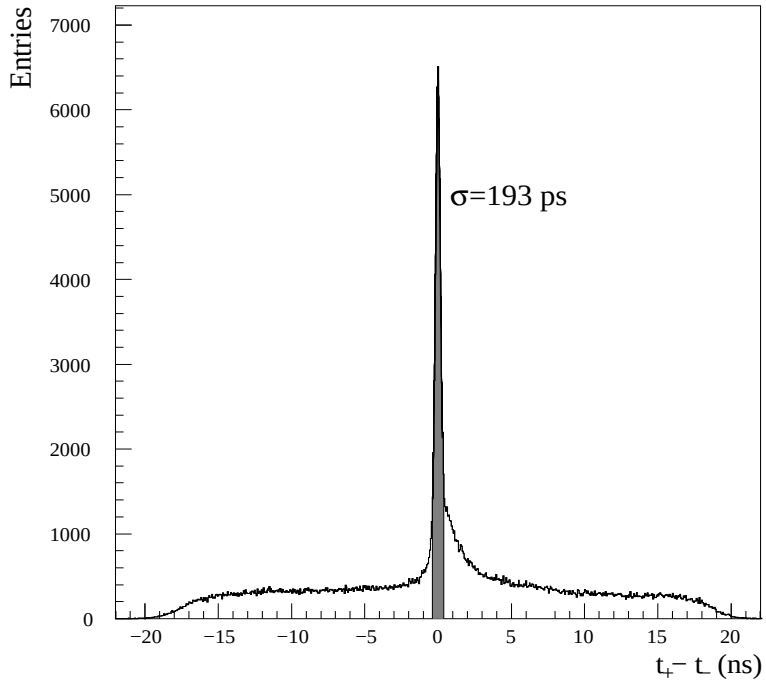

Figure 4.10: Time difference between charged positive and negative particles obtained from standard hadron trigger data. The central peak has a Gaussian width of 193 ps, and the shaded area represents a 2σ cut used to select prompt $\pi\pi$ events. The flat background is originated from accidental pairs, not belonging to the same beam interaction. Note the shoulder on the right–hand side of the peak, due to $\pi^- p$ prompt pairs.

right side of the peak is the effect of admixture of $\pi^- p$ pairs.

The timing capability of VH allows to separate $\pi^+\pi^-$pairs from $\pi^- p$ in the momentum range from 1 to 5 GeV/c and from πK pairs in the range from 1 to 2.5 GeV/c, as illustrated in Figure 4.11.

4.4.3 Horizontal Hodoscope

Horizontal Hodoscope detector is, as VH one, separated into two arms. Each of them covers active area of 0.4×1.3 m^2 and consists of 16 scintillating slabs oriented in horizontal direction (X–direction). Slabs are made of BICRON BC420 scintillating material with dimensions of 130 cm at length, 2.5 cm at width and with a thickness of 2.5 cm. Their ends are connected through lightguides to Phillips XP 2008 photomultipliers which are equipped, as VH ones, with voltage dividers to allow high counting capability. The front–end electronics system contains the same elements as VH.

The HH participates at T1 trigger and its response is used to apply compla-

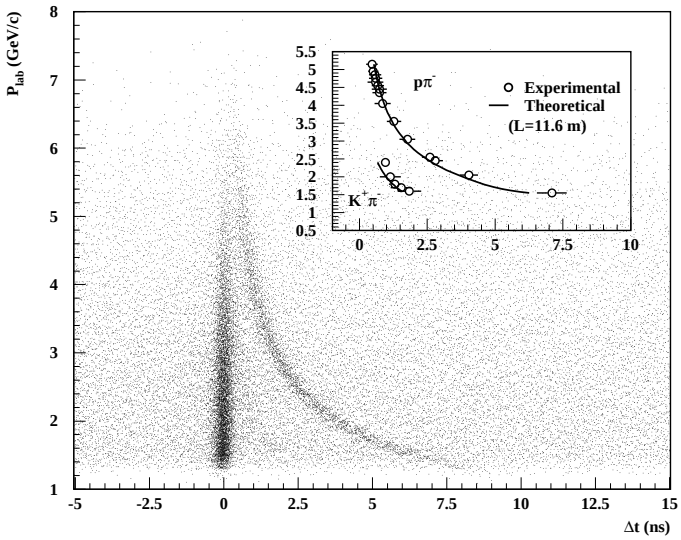

Figure 4.11: Correlation between the measured momentum of the positive particle and the VH time difference between the positive and negative spectrometer arm, taking into account the correction for the difference in path length. The accumulation bands correspond to $\pi^-\pi^+$ (vertical band) and $\pi^- p$ (curved band) pairs. A small cluster of $\pi^- K^+$ pairs is also visible in the intermediate region.

narity criterion to track pairs hitting both detectors arms. This criterion selects oppositely charged particles with relative vertical displacement less then 7.5 cm. The single hit detection efficiency of HH is better than 96.6% on both arms and the time resolution is 320 ps. It is worse than for VH due to greater length of slabs.

4.4.4 Čerenkov Counters

Čerenkov Counters play a crucial role in rejection of main background composed of e^+e^- pairs from photon conversion, Dalitz decay of π^0 and a minor extend from resonance decay. They are used in low levels of the trigger system and during off-line analysis.

They consist of two identical threshold Čerenkov detectors located in distance of 11.8 m from target. Each detector covers one spectrometer arm. The gas radiator, N_2 at normal temperature and pressure ($\theta_{\check{C}} = 1.4°$), is enclosed in volume defined by entrance and exit windows at distance of $2.85m$ and with dimensions 0.56×1.43 m^2 and 0.96×3.36 m^2, respectively. The pairs of adjacent mirrors (spherically deformed rectangles with average dimensions 0.30×0.35 m^2

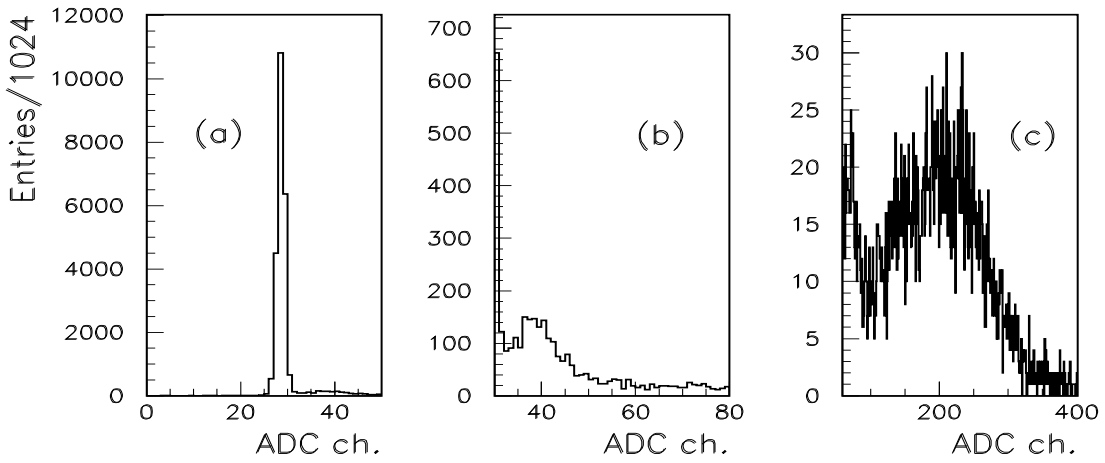

Figure 4.12: ADC spectrum from one Čerenkov photomultiplier: (a) spectrum from pions (practically equal to the ADC pedestal distribution), (b) amplitude signal from single photoelectron, (c) spectrum from electrons.

and $6mm$ thickness) reflect Čerenkov light into the same photomultiplier (Hamamatsu R1587 with $130mm$ UV-glass window). Each detector is equipped with 10 pairs of mirrors and 10 photomultipliers on two rows.

The analog signals from individual photomultipliers are fed into two custom-made summing modules , one per arm. The sum is after discrimination used in trigger for tagging of electrons. The sum and signals of individual photomultipliers are fed , after a delay line, into ADC units (LeCroy 4300B) and are available for off-line analysis and the detector tuning.

The typical ADC spectra from one Čerenkov channel are shown in Figure 4.12. The single photo-electron spectrum was used to cross-check the conversion factor from ADC counts to number of photoelectrons (N_{pe}). The mean values are $N_{pe} = 16.2$ and 16.4 respectively. From these values it was inferred that both counters have an efficiency greater than 99.8% when operated at a threshold slightly less than two photoelectrons. The pion contamination above the detection threshold is estimated to be less than 1.5%.

4.4.5 Preshower

Preshower detector (PSH) is used in the low level trigger logic and during off-line analysis allows additional elimination of electron background.

PSH is situated at a distance of 15.4 m from target and in each arm covers sensitive area of 0.75×2.8 m^2. The detector concept is based on a different behaviour of electrons and pions in matter. When electron flies through lead sheet it initialises electromagnetic showers while pion behaves mainly as a minimum ionising particle. The signal registered after the lead absorber strongly depends

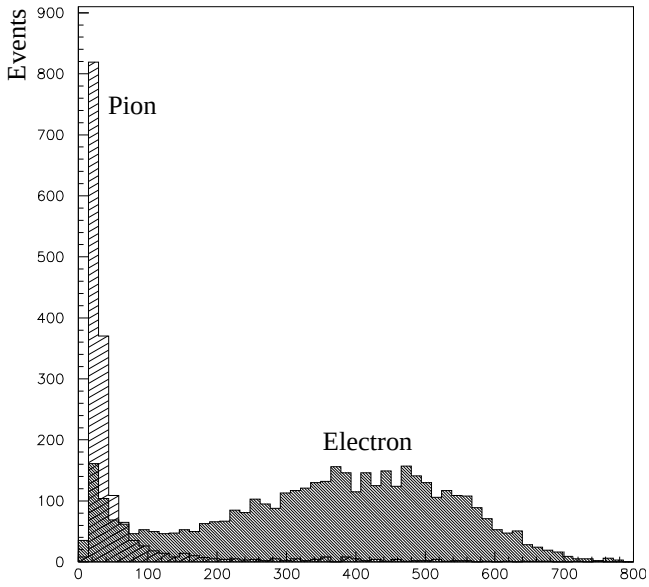

Figure 4.13: Pulse-height spectra for pions and electrons in one element of PSH.

on a species of a particle. For electrons it is stronger than for pions.

PSH is built like an array of 8 elements per one arm. Each element has a lead converter and one scintillating slab of $0.75 \times .35\ m^2$ size and 1 cm thickness. On one of its side each slab is connected through a light guide to EMI 9954-B photomultiplier. The lead converters of the two outermost elements of each arm (low momentum region) are $10mm$ thick, whereas the rest of them are $25mm$ thick.

The detector signals are linearly split into two branches, one used for trigger purposes and another one for off-line analysis. In the former, a leading edge discriminator is used with a threshold corresponding to efficient detection of minimum ionising particles. In the latter the signals are fed into 20 dB attenuators in order to fit the electron signals into dynamical range of LeCroy 4300B ADC. The typical ADC spectrum is shown in Figure 4.13.

The single arm detector efficiency is 99.5% for pions. The off-line studies show that rejection of electrons reaches 85% with less than 5% losses of pions. The combined information of CH and PSH provides almost 100% rejection of electrons.

4.4.6 Muon Detector

The muon counters are designed to detect muons, a serious source of background. The detector is placed at the downstream end of DIRAC apparatus at $16.5m$ distance from the target station and cover active area of $.75 \times 3.4\ m^2$ in each

spectrometer arm.

Muon detector consists of scintillation counters which are placed behind an iron absorber. This absorber almost entirely absorbs hadrons and related hadron showers and let fly through only muons. Its thickness is in the range from 60 to 140 cm. The thickness is larger in the region close to the spectrometer axis in order to compensate for harder particle momenta.

Due to location near the primary beam dump the detector may undergo high flux of background radiation from the dump. This fact requires a special design of the counter arrays and electronics. A double layer structure has been envisaged. Each arm is instrumented by 28 couples of scintillation counters with sensitive area of $75 \times 12cm^2$ each and $0.5cm$ thickness. The counters of couples are placed one after another in very small distance. The muon signal is accepted only if both matched counters are simultaneously hit. This condition significantly decreases the number of dummy signals, especially the ones from neutrons escaping from the beam dump.

The scintillation light is guided by fish-tail light from one end of a counter into photomultipliers (FEU-85). Signals from pair of corresponding counters are fed into constant fraction discriminators (CAEN C808) followed by meantimer (CAEN C561). This scheme ensures that output signal is generated only if both counters are hit and corresponding timing occurs only if the same particle crosses both counters.

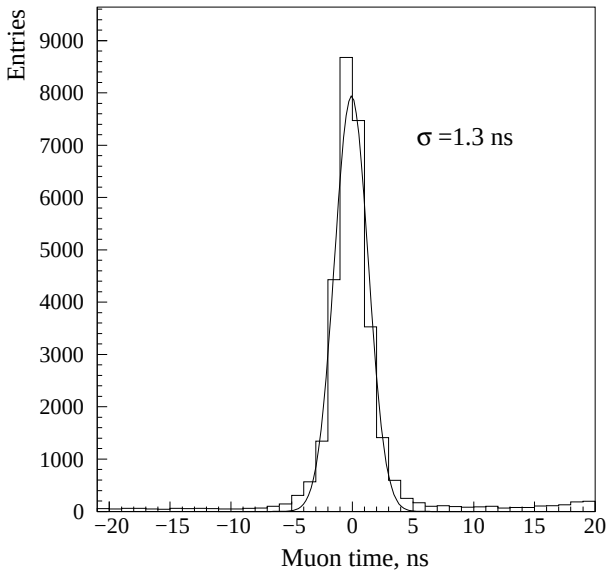

Figure 4.14: Time difference between the signals of the muon detector and the vertical hodoscope.

The suppression of muons is done off-line by applying a time cut between VH and MU detectors, see Figure 4.14. The fraction of events with at least one muon

was estimated at around 10%. Such muon events originate mostly ($\sim 80\%$) from $\pi^{\pm}$ decays proceeded between DC and Muon counters [35]. The time resolution of detector is 1.3 ns. It was not possible to study the efficiency of $\mu^{\pm}$ detection.

4.5 Trigger

The characteristic attribute of atomic pairs is their small relative momentum $Q < 3MeV/c$ while free pion pairs are produced with a wide distribution over Q. In order to reduce a number of free pairs in uninteresting region of high Q and to save maximum of rare atomic pairs a sophisticated multilevel trigger system is used.

The desired selection criterion is to reject pairs with $Q_l > 30\ MeV/c$ or $Q_x > 3\ MeV/c$ or $Q_y > 3\ MeV/c$ and keep all pairs with Q components below these values (Q_l, Q_x and Q_y are longitudinal and transversal components of the relative momentum, respectively). Due to the method of data analysis not only time correlated pairs in the mentioned Q interval are needed but also the uncorrelated ones are used. The optimal ratio between time-correlated and time-uncorrelated pairs is achieved with the coincidence time window of $\pm 20ns$ between the positive and negative spectrometer arms.

Since the start of operation in 1999 the trigger system has been several times upgraded. The most recent version is describe here. The comprehensive description of DIRAC trigger is in [36] and the performance of the trigger was studied in [37].

4.5.1 Trigger Scheme

A block diagram of the trigger system is presented on Figure 4.15. The zero level trigger (T0) activates neural network level of trigger (DNA). The first level of trigger (T1) starts digitisation of the detector signals in data acquisition modules (ADC, TDC, etc.) and in drift chambers data processor (T4). The positive decision of DNA in coincidence of T1 is demanded. If no, the clear signal is sent to data acquisition modules. Otherwise, additional positive decision from T4 is demand to read-out data of all detectors. This two stage process is chosen to minimise the trigger decision time and dead time due to long read-out time of MSGC. The read-out of MSGC is started immediately after DNA decision.

In addition to the main trigger task to detect atomic pairs, several additional calibration triggers are run in parallel. They are applied on T1 level without higher trigger levels but with appropriate prescaling factor.

The whole trigger system is fully computer controlled and no hardware intervention is needed in order to change the trigger configuration. The average number of accepted events per spill under typical experimental condition is 700.

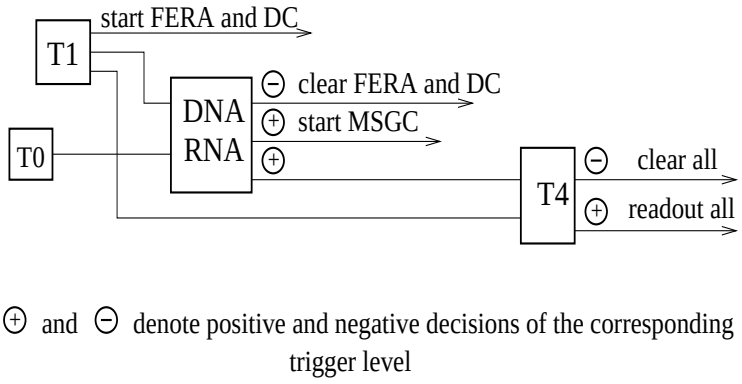

Figure 4.15: General block diagram of the DIRAC multilevel trigger.

4.5.2 Zero Level Trigger T0

The T0 trigger is introduced to obtain very early initial signal for DNA trigger. It is defined as a coincidence between Vertical Hodoscope and Preshower detector in each arm separately :

$$VH_1 \cdot PSH_1 \ \ \& \ \ VH_2 \cdot PSH_2,$$

where 1, 2 denotes positive and negative arm, respectively. The coincidence time window is chosen as for T1 trigger to be $\pm 20ns$.

4.5.3 First Level Trigger T1

The T1 trigger allows to make a fast coincidence among downstream detectors together with precise timing. It fulfils this basic tasks:

- Selects events with signals in both detector arms downstream the magnet in the time window of $\pm 20ns$. For timing the signal from Vertical Hodoscope is used.

- Classifies the signals from each arm as pion or electron. Protons, kaons and muons are also flagged like pions; their identification is performed in off-line analysis.

- Applies a cut on vertical angle between track of pions (Complanarity cut). It requires the difference between hit slabs in horizontal hodoscope in the two arms smaller or equal 2. This cut throws out pairs with high Q_y.

- Selects additional calibration events: e^+e^-, $\Lambda \rightarrow p + \pi^-$ decays and K decays into three charged pions.

To mark registered track in one arm like **pion** the signals from the downstream detectors must agree with this mask:

$$VH_i \cdot HH_i \cdot \overline{CH}_i \cdot PRS_i \;\; (i = 1 \; or \; 2),$$

which means, that hits must be registered in the vertical and horizontal hodoscopes and the preshower detector but not in Čerenkov detector of the appropriate arm.

Contrary to pion, for **electron** mark the signal of Čerenkov detector is demanded. The mask for electrons is following:

$$VH_i \cdot HH_i \cdot CH_i \cdot PRS_i \;\; (i = 1 \; or \; 2),$$

The marks of tracks from individual arms are combined for final T1 decision about pion pairs ($\pi_1\pi_2$) and electron pairs (e_1e_2). The vertical hodoscope is used to define the timing of track and to establish time coincidence window. Additionally, the Complanarity condition is demanded on pion pairs. This cut reduce number of accepted pairs by factor of two.

Additional to pion and electron pair signatures T1 trigger accepts events which are likely to come from a Λ decay $\Lambda \to p + \pi^-$ and kaons decay into three charged pions. Due to asymmetric kinematic of Λ decay the mask is following:

$$(VH_1(17) \cdot HH_1 \cdot \overline{CH}_1 \cdot PRS_1) \;\&\; (VH_2(1-16) \cdot HH_2 \cdot \overline{CH}_2 \cdot PRS_2)$$

For vertical hodoscope only the slab 17 is used in the positive arm while for the negative arm the slabs from 1 to 16 are looked at. The coincidence window is reduced to $\pm 2.5ns$.

For Kaon label three hits in vertical and horizontal hodoscope are demanded. At least one hit must be registered in each arm. The coincidence window is wider than that for Λ mark and is $\pm 5ns$.

The decision time of T1 electronics is $\sim 120ns$ in all.

4.5.4 Neural Network Trigger DNA

The DIRAC neural network trigger [38] is a processing system using a neural network algorithm. Its hardware is based on the custom-built version of the neural trigger used in the CPLEAR experiment [39].

DNA receives the hit patterns from the vertical hodoscopes VH_1, VH_2 and the X-planes of the upstream detectors IH and SFD. Optionally the PSH can be taken into account too. DNA is able to cope with up two hits in each VH_1 and VH_2 and up to five hits per X-plane of IH. Events with more hits are accepted for off-line evaluation. The hits in the two X-planes of IH are processed independently and simultaneously. An event is accepted if the trigger decision is true at least for one X-plane. This scheme eliminates influences of death spaces between slabs of IH X-planes.

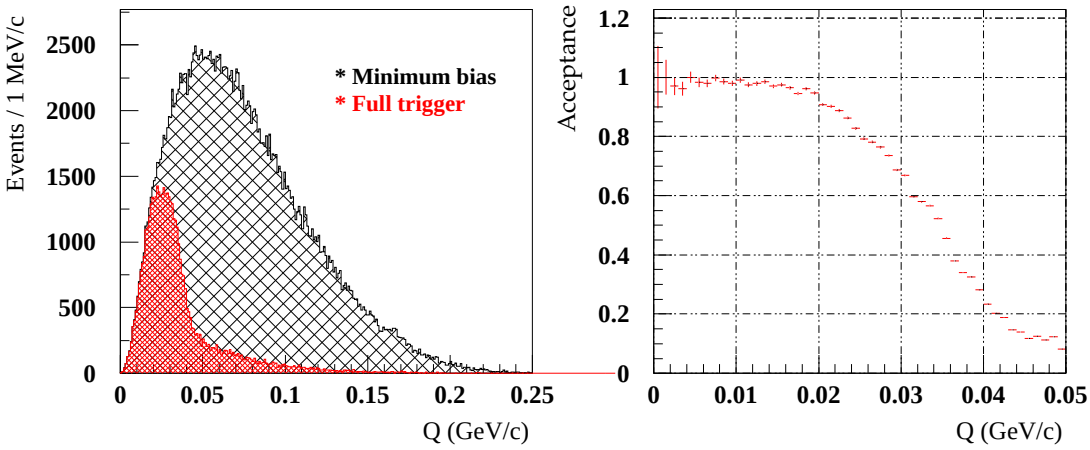

Figure 4.16: Left: Distribution of Q for accepted $\pi^+\pi^-$ pairs after the full DIRAC trigger system, and for minimum bias pairs. Right: trigger acceptance, determined as the ratio between the previous two distributions.

DNA was trained to select pairs with low relative momenta: $Q_x < 3MeV/c$ and $Q_L < 30MeV/c$. The training was performed on Monte Carlo simulated data followed by checks on real data. The cut on Q_y is done by Complanarity condition imposed by T1 trigger.

DNA trigger is started by the fast T0 pretrigger and evaluation time of an event is $\sim 210ns$. DNA rejection rate is about 2.3 with respect to T1 and the efficiency for the observed Q region is about 94%.

4.5.5 Fourth Level Trigger T4

T4 is the final stage of trigger. It quickly reconstructs X-projection of track registered by drift chambers and allows to estimate the Q_x projection of pair relative momentum. The detail description is given in [36].

T4 processor includes two stages: the track finder and track analyser. The track finder processor (one per arm) receives the numbers of hit wires from all X-planes of drift chambers and tries to find all possible tracks. Each track is assigned by the unique number "track identifier", in which are coded the hit wires belonging to this track. This allows to suppress parasitic combinations of hit wires in found tracks.

If at least one track is found in each arm, the track analyser continues the event evaluation. It receives the track identifiers from both arms and compares them with the content of the look-up memory table which contains all possible combinations of track identifiers for pion pairs with $Q_x < 3MeV/c$ and $Q_L < 30MeV/c$. This table was obtained from the dedicated simulation using the precise geometry of setup. If the relevant pair of tracks is found, T4 generates

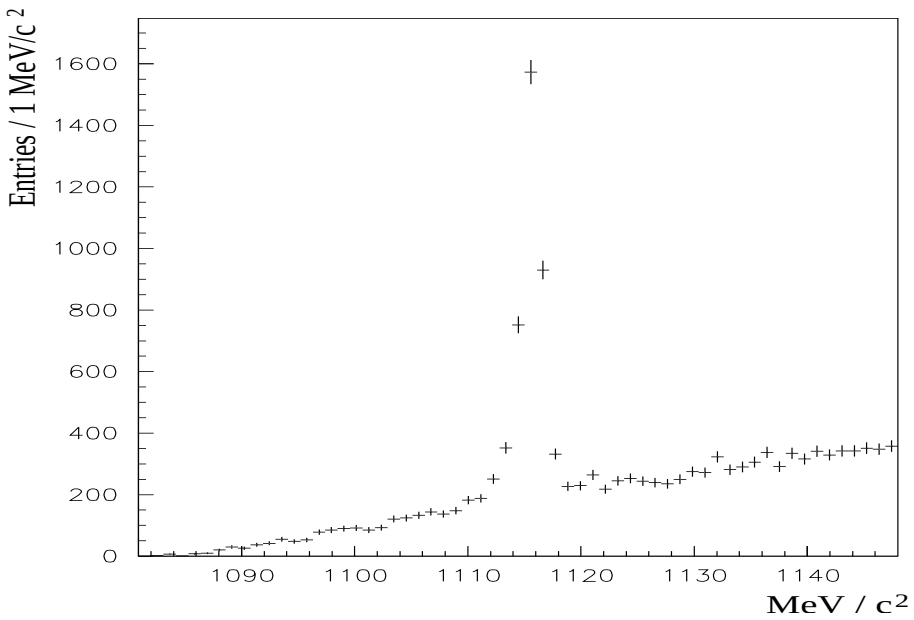

Figure 4.17: Invariant mass distribution of $p\pi^-$ pairs. Events were selected from a sample of Λ calibration data.

the positive decision and the event is accepted and all detector signals are read out. Otherwise, the Clear and Reset signal are applied to the all electronics.

The decision time of T4 trigger depends on complexity of the events and is about $\sim 3.5\mu s$ on average. The T4 rejection factor is about 5 with respect to T1 and around ~ 2.5 with respect to DNA.

The dependence of the acceptance of the trigger system on Q is shown in Figure 4.16. We see that In region of $Q < 20MeV/c$ it exceeds 95% and than falls on level of 10% for $50MeV/c$.

4.6 Set-up performance

The detector system is designed to provide high efficiency and resolution in the momentum and time detection of $\pi^+\pi^-$pairs with a small opening angle and a small relative momentum q.

The accuracy in determination of the relative momentum q is affected by detector resolution and multiple scattering in the target and set-up elements. Based on the dedicated measurements and simulations the accuracy of the determination of the longitudinal (q_L) and transverse (q_x, q_y) components of the relative momentum q has been estimated as 0.6 MeV/c and 0.4 MeV/c, respectively. If upstream detectors are excluded from the track reconstruction, the uncertainty in the measurement of q increases to a level of $1MeV/c$ for each component.

Calibration of the energy scale and the experimental determination of the setup resolution are performed by monitoring the position and the width of the Λ signal detected by the apparatus. Reconstructed $p\pi^-$ invariant mass obtained from the calibration data is shown in Fig. 4.17. The Λ signal is clearly seen above a small background. Gaussian plus polynomial fit to the data gives $M_\Lambda = 1115.67$ MeV/c^2 and $\sigma_\Lambda = 0.43$ MeV/c^2. Calibration using $\Lambda \to p\pi^-$ decays is used in addition to control the precision of the setup alignment. Any misalignment of the tracking system in one arm relative to the other arm would result in asymmetrical errors on the reconstructed momenta.

The accuracy of the time measurement is obtained from the analysis of distribution of the e^+e^- time differences at Vertical Hodoscope as describe in Section 4.4.2 and is about $170ps$.

4.7 Contribution of the author

The author, as a member of Prague group, shared the responsibility for Horizontal Hodoscope (HH). His work included the participation on test beams, on preparation of HH for data-taking and maintenance of this detector during running period. He performed the analysis of an efficiency of this detector which was presented on a collaboration meeting and was included into the DIRAC-GEANT simulation code.

He regularly participated in data taking. In the years 2001 and 2002 he collaborated on off-line checks of a set-up performance and took part in development of the code intended for this purpose.

He further took part in two analyses of the apparatus performance. The first one was devoted to determination of the dead time of the apparatus from a number of events taken per spill. Due to the high uncertainty in the measurement of beam intensity this analysis didn't give a reasonable result and the dead time was evaluated by another method. The second analysis was concerned with the calibration of the set-up using the decay of K meson into three charged pions. Due to a very low probability of the detection of all three pions from Kaon decay it was not possible to extract the clear Kaon signal from the data.

The author was further involved in 2001 data calibration and presented the DIRAC experiment preliminary results on a conference "Mesons and Light Nuclei 2001, Prague" [40]. The repeated installations of detectors for background measurement in DIRAC experimental area belong to his other activities.

Chapter 5

Simulated Data

5.1 Simulation of r^* distribution

In order to get an image of space-time characteristics of a pion production region the Monte-Carlo simulation was done using UrQMD-1.3 (Ultrarelativistic Quantum Molecular Dynamics model) code [41]. This is a classical transport code which produces information about both the momenta and the emission points of outgoing particles.

The original code does not take into account final size of resonances and manages their decays as point-like. It means, that all daughter particles originating in one resonance decay fly out from one space point. This approach causes an unphysical behaviour of r^*–distribution in the region of very small r^*. There is non-negligible amount of pairs coming from decay of one mother resonance and these pairs generate a δ–peak at $r^* = 0$. Moreover, this approach deforms the distribution of pairs where pions are gradually generated in a cascade decay of one resonance. Their contribution disturbs the behaviour for $r^* \to 0$ given by a space factor $\propto r^2$ (See Figure 5.1). Therefore, we modified the original code by smearing origin points of decay products using a Gaussian distribution with $0.5fm$ width.

To get reliable information about r^*–distribution, the very limited spatial acceptance of detector set-up has to be taken into account. Due to a high computer time need for the simulation of interactions we avoid a full simulation of the detector response and, at the first stage, we take into account only the geometrical restriction given by the secondary channel.

Besides spatial restriction done by the secondary channel the momentum acceptance of the spectrometer system must be taken into account. The acceptance matrix for both π^- and π^+ was obtained from the full detector simulation. Its dependence on the magnitude of pion momentum and on the angle with respect to the secondary channel axis in zx and zy planes for π^- is shown in Figure 5.2. The strong dependence on magnitude and angle in zx–plane (the plane perpendicu-

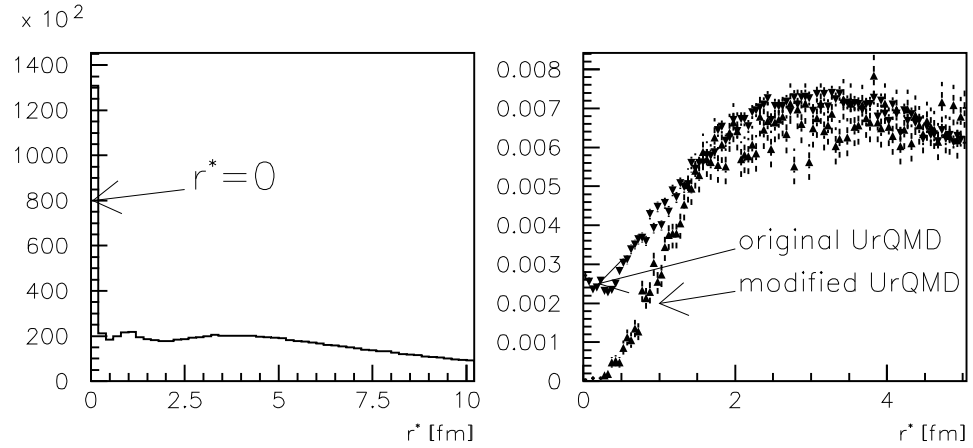

Figure 5.1: **Left:** $r^* = 0$ peak composed of pairs of pions coming from the decay of a common point–like resonance. **Right:** Deformation of r^*–distribution due to cascade decay of point–like resonances (original UrQMD) and the same distribution after the introduction of smearing of resonance decay points (modified UrQMD).

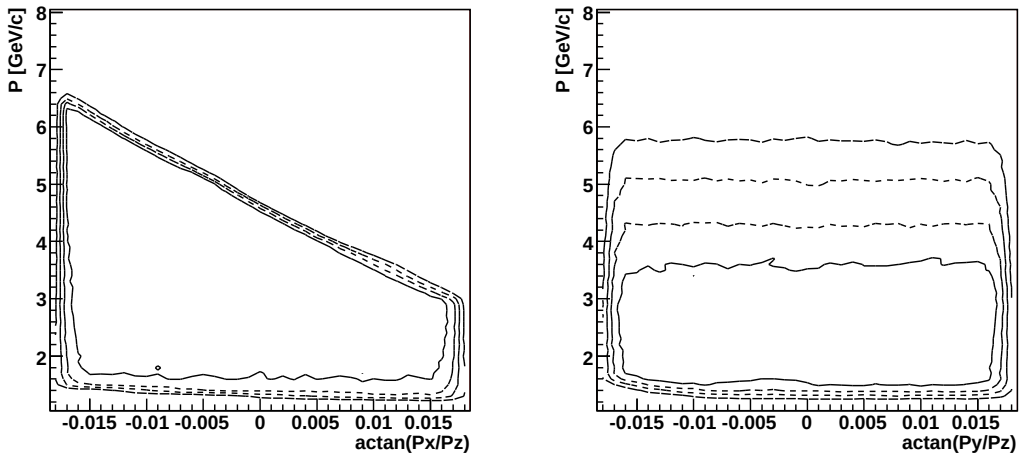

Figure 5.2: Acceptance of drift chambers for π^- obtained from the full simulation of detector response. **Left:** Dependence of the acceptance on the magnitude of pion momentum and angle with respect to the secondary channel axis in zx-plane. **Right:** The same as for Left, for zy-plane. The full lines mark the level of 80% acceptance, the dashed ones 60,40 and 20% acceptance.

lar to applied magnetic field in the spectrometer magnet) and weak dependence on the angle in zy-plane are visible. The π^+ acceptance matrix shows a similar behaviour with a symmetrically opposite dependence on the angle in zx–plane.

Due to a nearly flat dependence of the acceptance on the angle in zy–plane we neglect this one and only take into account the dependence on magnitude and angle in zx-plane of pion momentum vector. We used this acceptance as a weight for each pair during the processing of simulated data.

The axial symmetry of primary interaction allows us to improve the efficiency of UrQMD simulation by introducing in addition to the real secondary channel next fourteen non-overlapping imaginary channels which are put around the beam axis. The coordinates of an accepted pion pair in an arbitrary imaginary channel are rotated around the beam axis in accordance with rotation which transfers the axis of the hit channel into the axis of real one. This increases the simulation efficiency by a factor of fifteen and after that approximately five events out of one thousand generated ones contain at least two pions which fly through the secondary channel.

The simulation was done for pNi collisions with proton incident energy of 24 GeV. The freezeout time[1] was set to $10000 fm$ and all unstable particles are forced to decay at the end of time evolution cycle.

Types of Sources

In UrQMD three possible production processes of pions are included: direct production, decay of resonances and inelastic rescattering. UrQMD output contains information about the emission points, momenta and types of mother particles. The emission point of each particle is identified with the point of the last interaction (i.e. scattering) if it exists, otherwise with the creation point. If a particle takes part in a scattering or is produced directly, two types of mother particles are given. If particle is created during a resonance decay and after that does not interact at all, only one type of the mother resonance is found.

Due to a similarity in the description of the direct production and rescattering, we can not distinguish between these two processes. Fortunately, the space-time characteristics of pions produced by these processes are similar and their probabilities quickly fall with the distance from the point of primary interaction in DIRAC experiment condition so that for our purpose this is not a crucial problem.

According to these three types of production processes we divide the pion pairs into the following three groups:

- **Decay pairs**: both pions are produced in decays of resonances

[1]The time for which the evolution of the system created during the primary interaction is performed. After this time no interaction with high momentum transfer occurs and particles can only be influenced by FSI.

	$\pi^-\pi^-$	$\pi^+\pi^-$
Total number	111 620	418 900
Decay pairs	34.2%	40.0%
Direct pairs	12.9%	9.5%
Mixed pairs	52.9%	50.5%
Decay-one pairs	$\sim 0\%$	$\sim 10.1\%$
Decay-two pairs	$\sim 34.2\%$	$\sim 29.9\%$
Decay-com pairs	6.4%	14.6%

Table 5.1: Fractions of individual groups of $\pi^-\pi^-$ and $\pi^+\pi^-$ pairs. Decay-one are pairs of pions born in one resonance decay, Decay-two are pairs of pions coming from two different resonances and Decay-com pairs are Decay pairs of pions with the same type of mother particle.

- **Direct pairs**: both pions originate in direct processes or in rescattering
- **Mixed pairs**: one pion is from a decay and the other one from direct or rescattering process

The simulated r^*–distributions for all three groups of $\pi^-\pi^-$ and $\pi^+\pi^-$ pairs are shown in Figure 5.3. Their individual contributions are listed in Table 5.1. From the figures it is noticed, that spectra of Mixed and Direct pairs are similar for $\pi^+\pi^-$ and $\pi^-\pi^-$ case, whereas, Decay pairs differ from each other by presence of a dominant peak in the region of small r^* for $\pi^+\pi^-$. As it is shown in Figure 5.3(Bottom), this peak is formed by pairs of pions with the same type of mother particle (Decay-com pairs). Unfortunately, we are not able to distinguish between pions coming from decay of one resonance (Decay–one pairs) and two same resonances. Since these two types of Decay pairs have absolutely different spectra of r^*, we need to estimate their contributions.

Decay–com $\pi^-\pi^-$ pairs can only contain a very small amount of Decay-one pairs[2]. Decay-one pairs are characterised by a small r^*, peaked around $1fm$ and practically not exceeding 10 fm. Moreover, we can suppose that r^*–distribution of Decay-two pairs are similar for $\pi^-\pi^-$ and $\pi^+\pi^-$. Dividing the $\pi^-\pi^-$ by $\pi^+\pi^-$ r^*–spectra of Decay-com pairs (Figure 5.6) we obtain a constant equal to about 0.38 in the region of $r^* > 10fm$. Dividing the total number of $\pi^-\pi^-$ Decay-com pairs by this constant we estimate the amount of $\pi^+\pi^-$ pairs coming from two same resonances. Subtracting this amount from the total number of $\pi^+\pi^-$ Decay-com pairs, we obtain an approximate amount of $\pi^+\pi^-$ Decay-one pairs (See Tab. 5.1).

[2]We checked that no resonances which significantly contribute in these pairs, decay into two π^-.

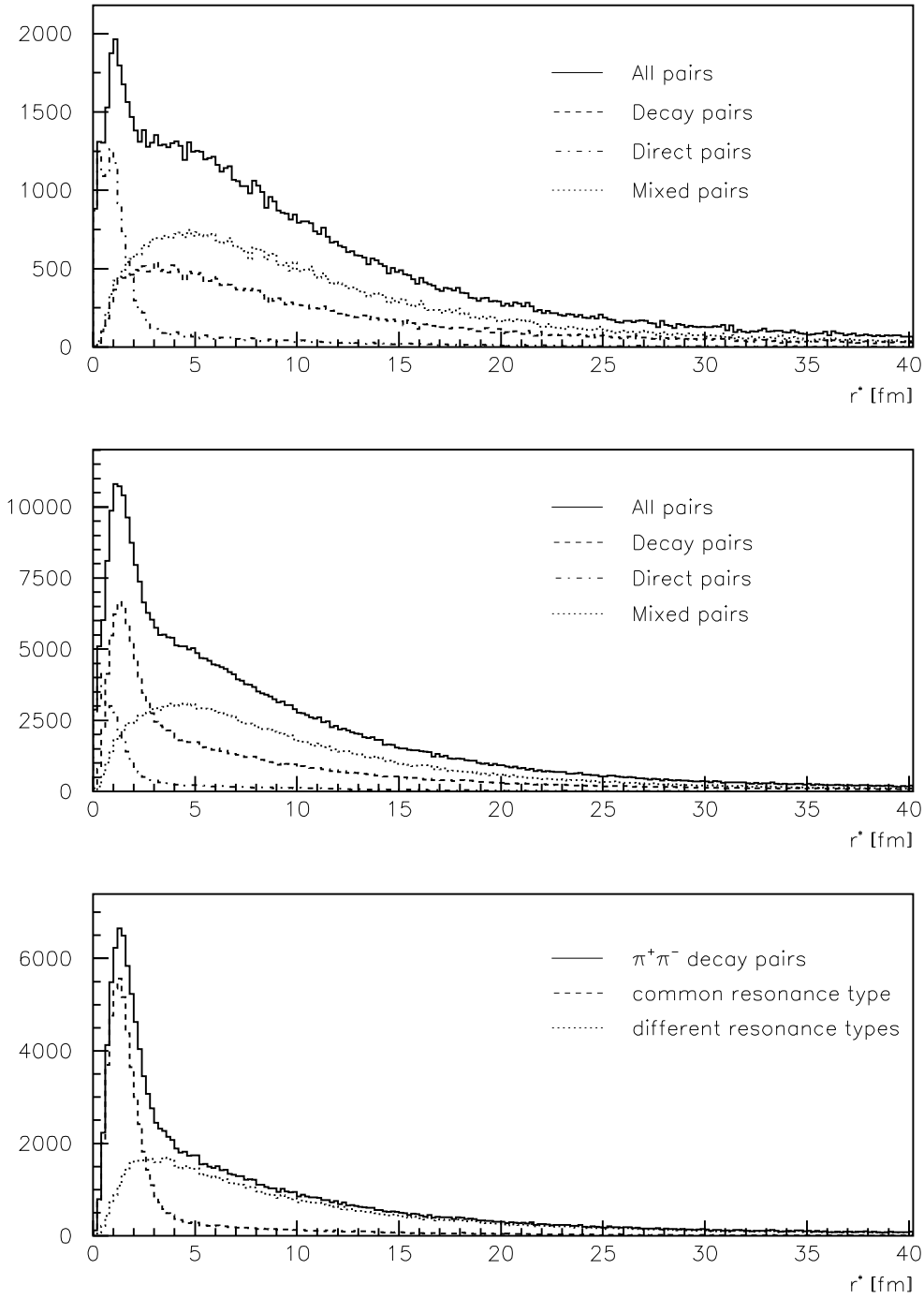

Figure 5.3: r^*–distributions generated by modified UrQMD for all three groups of $\pi^-\pi^-$ pairs (**Top**) and $\pi^+\pi^-$ pairs (**Middle**). The distribution of $\pi^+\pi^-$ Decay pairs for pions coming from one or two different species of resonances (**Bottom**).

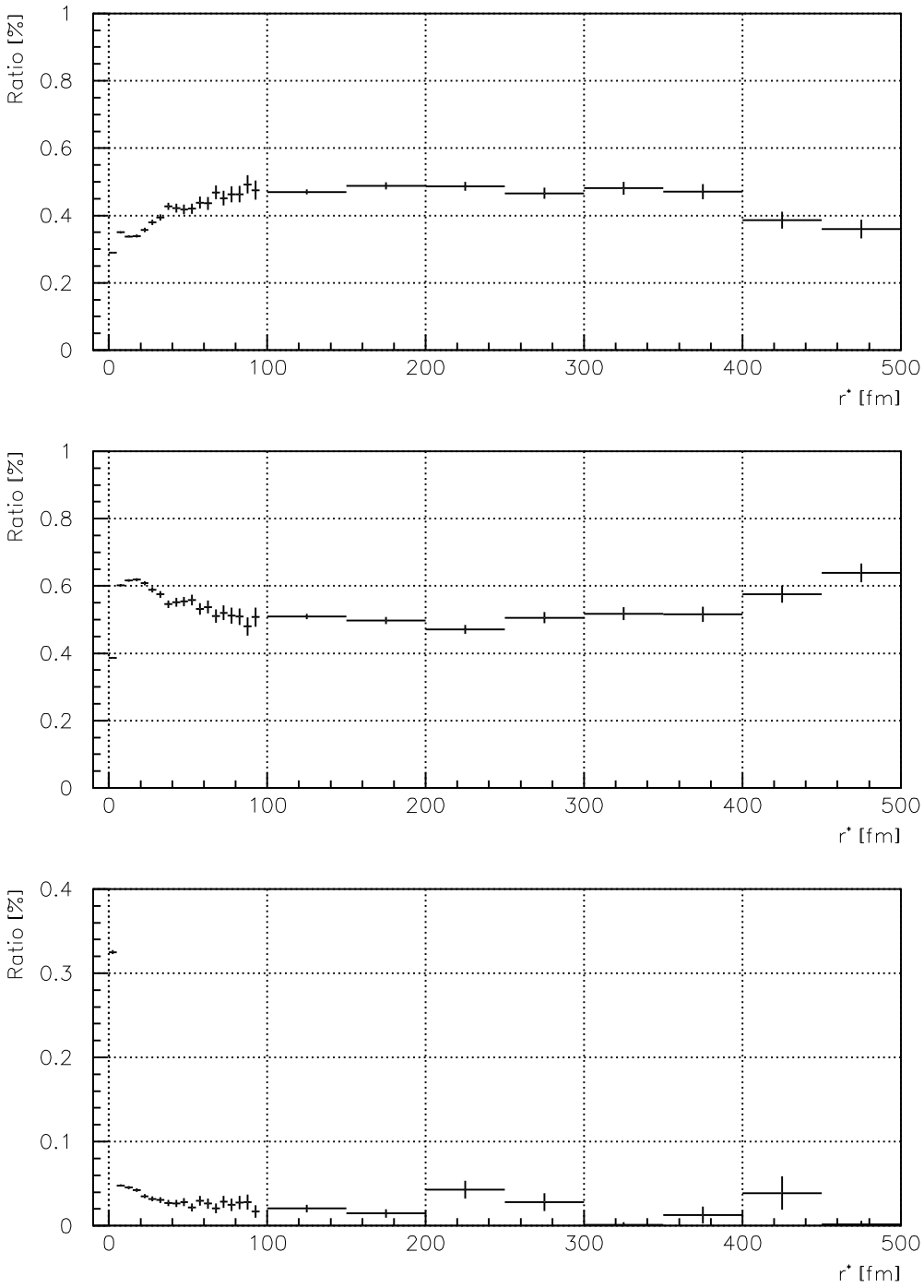

Figure 5.4: The contribution of each type of $\pi^-\pi^-$ pairs to the total r^*–distribution. Decay pairs(**Top**), Mixed pairs(**Middle**) and Direct pairs(**Bottom**).

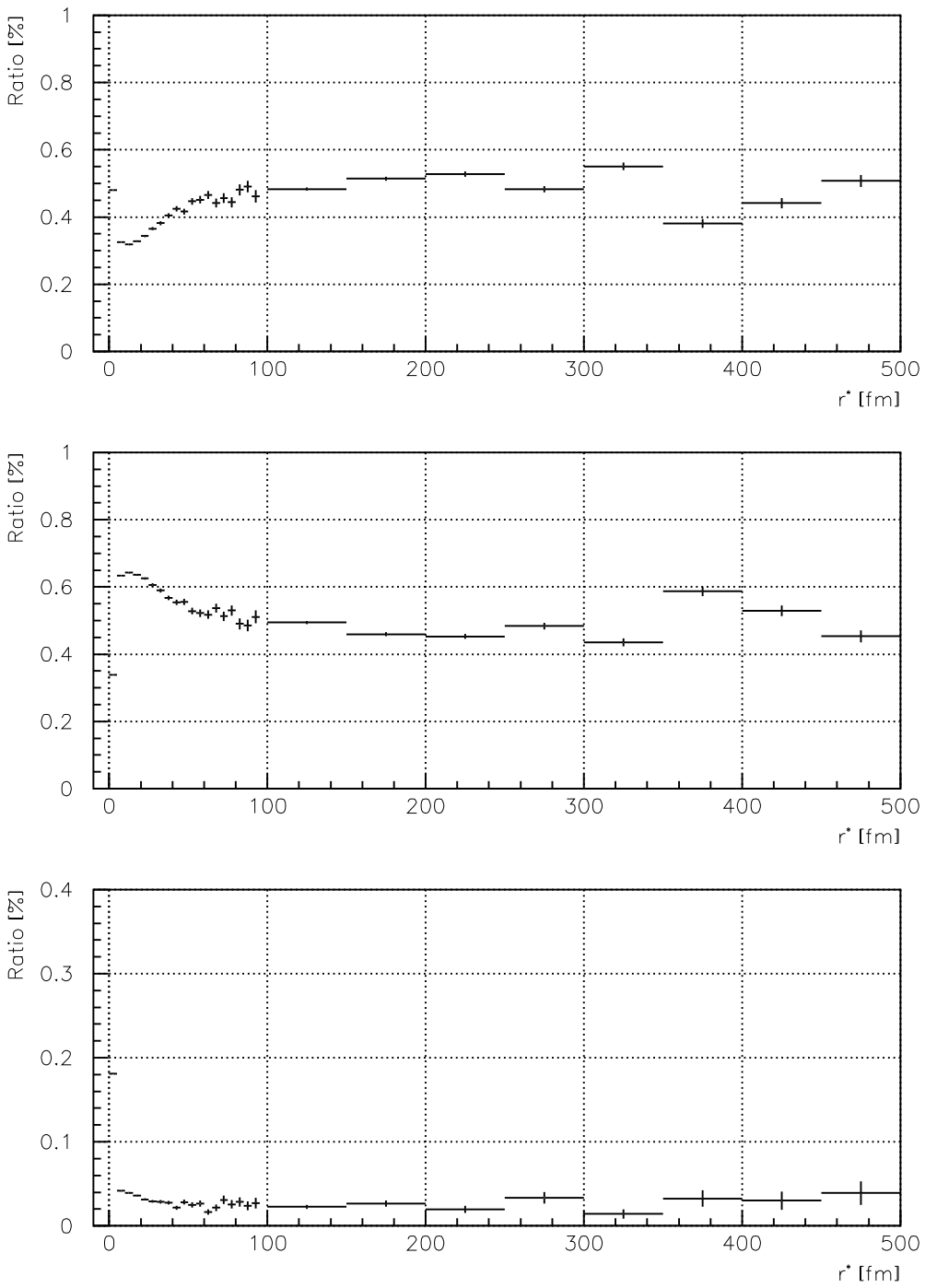

Figure 5.5: The contribution of each type of $\pi^+\pi^-$ pairs to the total r^*–distribution. Decay pairs(**Top**), Mixed pairs(**Middle**) and Direct pairs(**Bottom**).

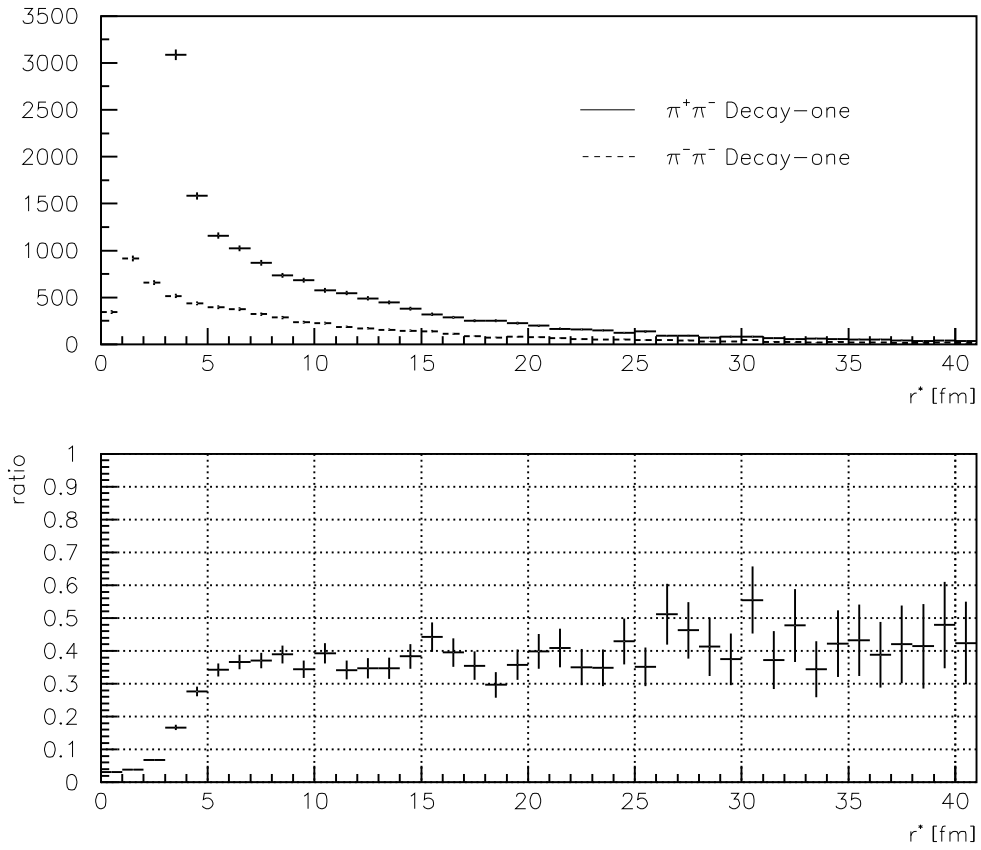

Figure 5.6: Decay-one pairs r^*distribution for $\pi^-\pi^-$ and $\pi^+\pi^-$ case (**Top**) and their ratio (**Bottom**).

In general, we can say, that Direct pairs significantly contribute (See Figure 5.4 and 5.5) in the region of small $r^* \lesssim 3fm$ with a maximum around $1fm$ and with a negligible tail for higher r^*. Mixed and Decay pairs have similar shapes of r^*–distributions (except for Decay-one pairs) with maxima around $4fm$ and tails extending up to thousands fm. These tails are dominantly formed by ω and η' pairs, i.e. pairs where at least one pion comes from a ω or η' decay, respectively. The Decay–one pairs have a r^*–spectrum close to that of Direct pairs and so they belong to the short-range pairs.

Yield of ω and η' resonances

DIRAC experiment approach to production of $A_{2\pi}$ atoms and Coulomb pairs discussed in Section 3.3.1 assumes the existence of two types of pion sources, i.e.

	$\pi^-\pi^-$	$\pi^+\pi^-$
$(\omega+\eta')$ pairs	21.2%	20.9%
$(\omega+\eta')_a$ pairs	21.2%	13.5%
ω pairs	20.6%	19.8%
ω_a pairs	20.6%	13.2%
ω_1 pairs	0.%	6.6%
ω_2 pairs	0.54%	0.31%
$\omega_1+\omega_2$ pairs	0.54%	6.9%
η' pairs	0.57%	1.13%
η'_a pairs	0.84%	0.50%
η'_1 pairs	0.%	0.79%
η'_2 pairs	$\ll 0.01\%$	$\sim 0.\%$
$\eta'_1+\eta'_2$ pairs	$\ll 0.01\%$	0.79%

Table 5.2: Fractions of particular ω and η' pairs.

the short-lived and the long-lived ones. The pions from the short-lived sources are produced at typical mutual distances $r^* \ll |a|$ in their c.m.s. and all other pion pairs are characterised by $r^* \gg |a|$, where $|a| = 387.5fm$ is Bohr radius of two pion system (Table 2.1).

This assumption is mainly violated by pions coming from the decays of ω and η' resonances:

$$\begin{array}{lcl} \omega & \to & \pi^+\pi^-\pi^0 \\ \omega & \to & \pi^+\pi^- \\ \eta' & \to & \pi^+\pi^-\eta \\ \eta' & \to & \rho^0\gamma \to \pi^+\pi^-\gamma \end{array} \qquad (5.1)$$

which form the main contribution in the region of $r^* \sim |a|$. Figures 5.8 and 5.9 display their r^*–distributions together with their inputs into total spectra as a functions of r^*. We can notice, that $(\omega+\eta')$–pairs form 90% part of r^*–distribution in the region $r^* \sim |a|$. Thus they are crucial for the evaluation of the correction due to the final size of pion production region.

When evaluating their contributions into the all $\pi^-\pi^-$ and $\pi^+\pi^-$ pairs, we must take into account the fact, that ω and η' $\pi^+\pi^-$ pairs contain pairs coming from a decay of one ω or η' resonance. In the following, we will denote them as ω_1 and η'_1 pairs, respectively. The r^*–distributions of these pairs significantly differ from the rest of ω and η' pairs (we will denote them as ω_a and η'_a). The ω_1 and η'_1 pairs are peaked around $r^* \sim 1fm$ and do not contribute into the region of $r^* \sim |a|$. Their r^*-distributions are similar to the that of Direct pairs as is shown in Figure 5.7.

Unfortunately, we meet the same problem as in the previous part, i.e. we are not able to distinguish exactly the simulated ω_1 and η'_1 pairs from the pairs coming

from decays of two different ω, η' resonances (ω_2 and η'_2 pairs, respectively). We can only provide an estimation of their yields.

If we compare the topology of the $\pi^-\pi^-$ pairs where just one π^- originates in ω decay with the $\pi^+\pi^-$ pairs where π^+ comes from the ω resonance and π^- is coming from any other source, we find them to be the same except for one difference. In the first case we observe as a product of the ω decay π^- while in the second one it is π^+. Since the probabilities that π^- or π^+ from ω decay fly into the secondary channel are the same we can suppose that also the yields of these two types are identical.[3]

The $\pi^-\pi^-$ pairs can not contain ω_1 pairs. When both pions originate from ω we know, that all $\pi^-\pi^-$ pairs are ω_2 pairs. Therefore, we can directly evaluate the ratio k_{d--} between ω_2–pairs and the pairs where just one π^- comes from ω decay. At the same time this ratio determines up to combinatoric factor[4] of 2, how many $\pi^+\pi^-$ ω_2–pairs are produced as compared with the number of $\pi^+\pi^-$ pairs where π^+ is from ω resonance and π^- is from any other source. This allows us to estimate the fraction of ω_1 and ω_2 $\pi^+\pi^-$ pairs.

The same method can be employed for evaluation of the amount of η'_1 pairs. Since the number of $\pi^-\pi^-$ η'_2–pairs is negligible, we can suppose that all $\pi^+\pi^-$ pairs with both pions coming from η' are η'_1–pairs. Their r^*–distribution shown in Figure 5.7 confirms this assumption.

In addition, the yields of η'_a pairs must be scaled by a factor of 1.46 to take into account the existence of decay channel $\eta' \to \rho^0\gamma \to \pi^+\pi^-\gamma$. Due to the extremely short lifetime of ρ^0 resonance, the pions created in this decay channel behave like pions directly produced in η' decays (if we neglect the kinematics differences). But they are marked as pions from ρ^0 decay. Hence, we are not able to identify them and we must use the scale factor of 1.46 which corresponds to branching ratios of η' decay channels included in UrQMD (0.65 for the direct decay and 0.3 for the decay through ρ^0)

The individual fractions of ω and η' pairs are listed in Table 5.2. The yields of η'_a are already corrected for ρ_0 contribution.

Parametrisation of r^*–distributions

For analyses of corrections due to the final size of production region we need good parameterisations of r^*–distributions, especially for ω and η' pairs. These parameterisations must be performed for both $\pi^+\pi^-$ and $\pi^-\pi^-$ pairs.

Firstly we will deal with $\pi^-\pi^-$ pairs. Path lengths $l \approx \tau\langle p_{\mathrm{dec}}\rangle/m_\pi$ of ω and η' are determined by the resonance lifetimes τ and the four-velocity p_{dec}/m_π of the decay pion. As a consequence of the exponential decay law, the corresponding

[3] This assumption is violated by the influence of the detector acceptance. Here we neglect its effect.

[4] Daughter particles of two ω resonances can form one $\pi^-\pi^-$ and $\pi^+\pi^+$ pair and two $\pi^+\pi^-$ pairs.

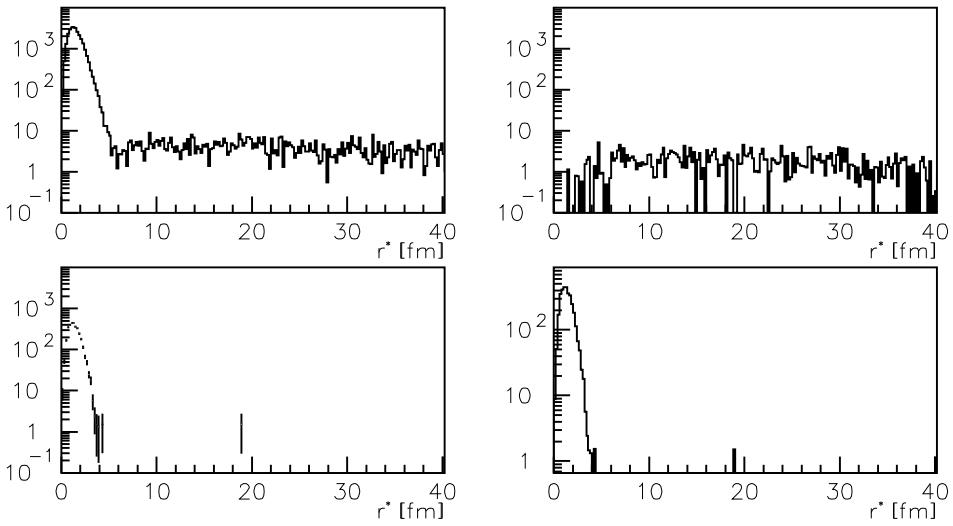

Figure 5.7: The r^*–distributions of $\pi^+\pi^-$ $(\omega_1+\omega_2)$ pairs(**Top-left**), $\pi^-\pi^-$ ω_2 pairs(**Top-right**) and $\pi^+\pi^-$ η_1' pairs(**Bottom-right**). The difference between $\pi^+\pi^-$ $(\omega_1+\omega_2)$ pairs and the $\pi^-\pi^-$ ω_2 pairs scaled by a factor of 2 (**Bottom-left**).

r^*–distributions are nearly exponential (Figure 5.8) except for the region of small r^* dominated by the phase space suppression factor $\propto r^{*2}$. Actually, these distributions may deviate from the exponential ones due to a continuous spectrum of the decay momenta and the averaging over the emission points of the second pion.

We found that the simulated η' contribution can be sufficiently well parameterised by a single exponential formula interpolating between the phase–space and the exponential behaviour (suggested by R. Lednický [26])

$$\sum_i \frac{dN(\pi_{\eta'}\pi_i)}{dr^*} \doteq n_{\eta'}\mathcal{F}(r^*; r_{\eta'}, l_{\eta'}), \tag{5.2}$$

$$\mathcal{F}(r^*; r_{\eta'}, l_{\eta'})$$
$$= \frac{x^2}{2.2}\left\{1-\exp\left[-\frac{2.2}{x^2}\left(1+0.2x^2\frac{1+0.15x^2 r_{\eta'}/l_{\eta'}}{1+x^5/125}\right)\right]\right\}\exp\left(-\frac{r^*}{l_{\eta'}}\right), \quad x=\frac{r^*}{r_{\eta'}}, \tag{5.3}$$

where fitted parameters are $r_{\eta'} = 1.99 \pm 0.01$ fm, $l_{\eta'} = 925 \pm 52$ fm. At the same time, a good description of the ω-contribution requires a superposition of the two exponential-like expressions:

$$\sum_{i\neq\eta'} \frac{dN(\pi_\omega\pi_i)}{dr^*} \doteq n_{1\omega}\mathcal{F}(r^*; r_{1\omega}, l_{1\omega}) + n_{2\omega}\mathcal{F}(r^*; r_{2\omega}, l_{2\omega}). \tag{5.4}$$

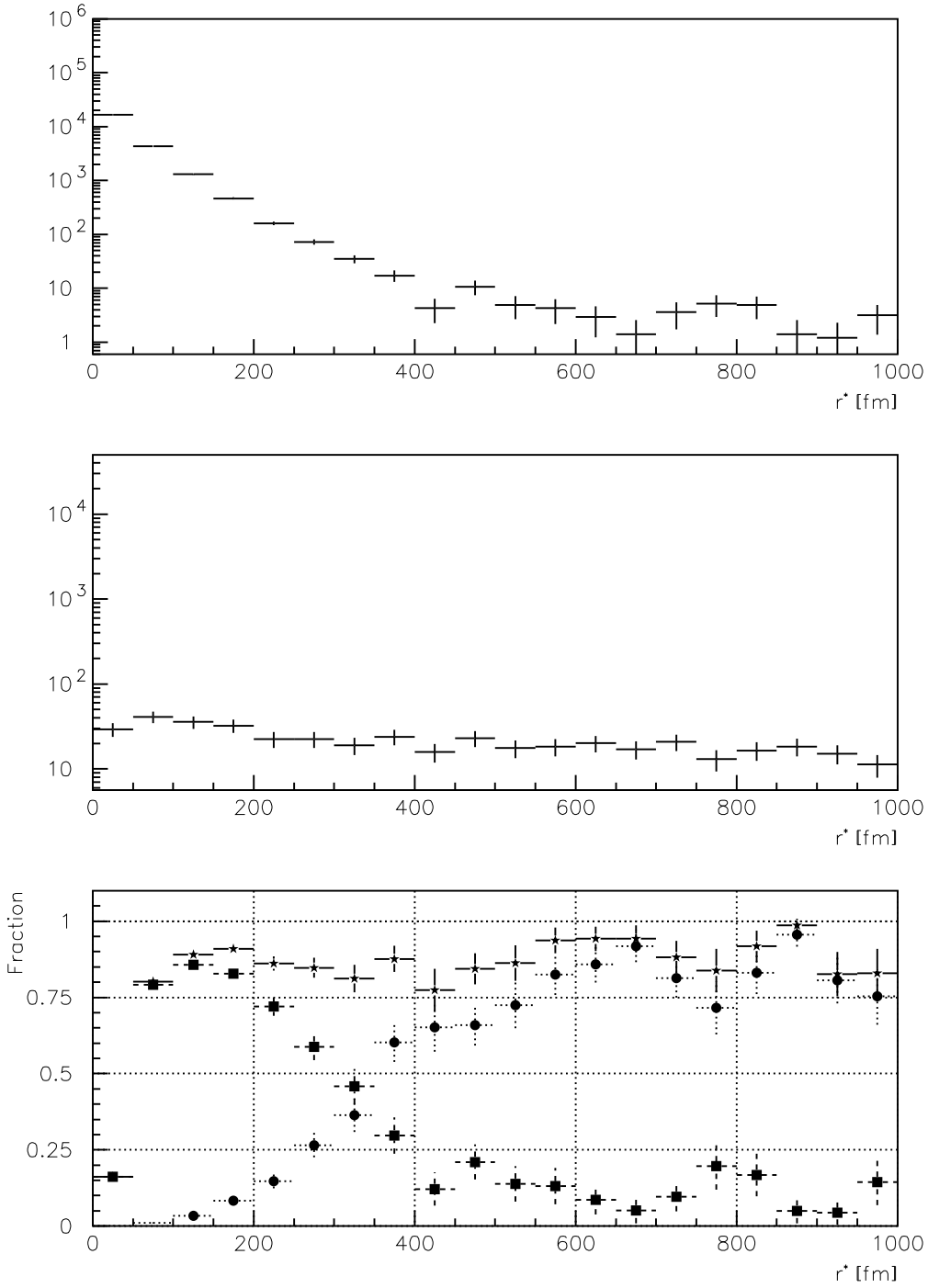

Figure 5.8: r^*–distribution of $\pi^-\pi^-$ pairs with at least one pion coming from decay of ω (**Top**) and η' (**Middle**). The relative contributions of $(\omega+\eta')$ pairs as a function of r^*-distribution (**Bottom**). The squares, circles and stars represent the ω,η' and $(\omega+\eta')$ pairs, respectively.

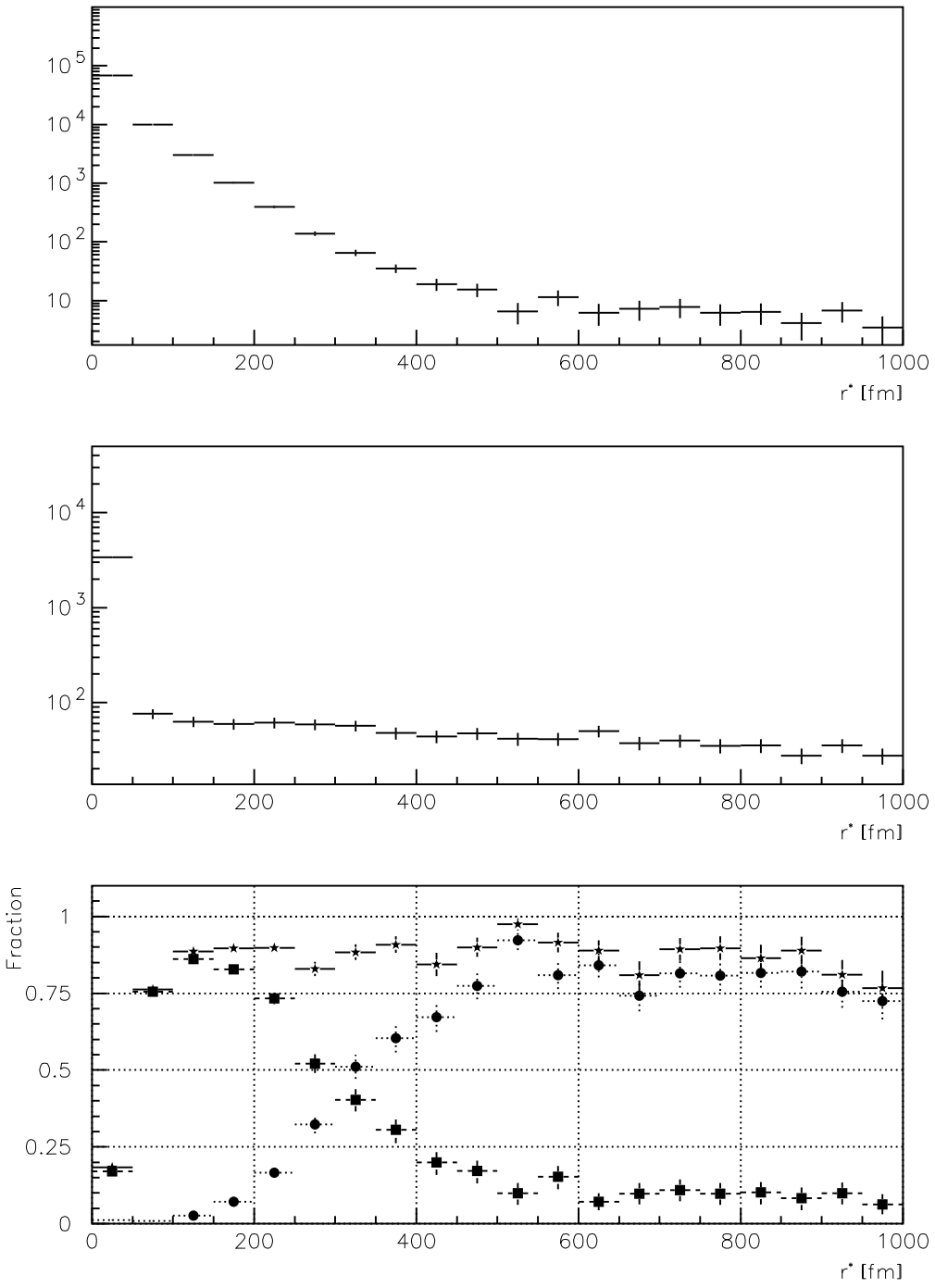

Figure 5.9: r^*–distribution of $\pi^+\pi^-$pairs with at least one pion coming from decay of ω (**Top**) and η' (**Middle**). The relative contributions of $(\omega + \eta')$ pairs as a function of r^*-distribution (**Bottom**). The squares, circles and stars represent the ω,η' and $(\omega + \eta')$ pairs, respectively.

From the fit we obtain the following values of parameters $r_{1\omega} = 3.44 \pm 0.11$ fm, $l_{1\omega} = 27.56 \pm 0.85$ fm, $r_{2\omega} = 0.83 \pm 0.06$ fm, $l_{2\omega} = 52.00 \pm 0.75$ fm and $n_{1\omega}/n_{2\omega} = 1.703$. The remaining part of Decay and Mixed pairs (the ω and η' contribution must be subtracted), including the tail, can be effectively described by a power–like expression

$$\mathcal{M}(r^*; r_M, \alpha, \beta) = r^{*2} \left[1 + \left(\frac{r^*}{r_M} \right)^{2\alpha} \right]^{-2\beta}, \tag{5.5}$$

where the fit gives $r_M = 15.6 \pm 0.9$ fm, $\alpha = 0.35 \pm 0.01$, $\beta = 5.38 \pm 0.18$. Let us note that the tail vanishes as $(r^*)^{-5.5}$, i.e. much faster than the Lorentzian ($\alpha = \beta = 1$) which is sometimes used for description of this type of spectra.

The Direct pairs are peaked around 1 fm. The shape of this peak has a double structure as can be seen in Figure 5.10. This shape is difficult to parametrise. However, the correction which we are interested in is only weakly[5] sensitive to shape of r^*–distribution for very small r^*. Therefore, we will represent this part of r^*–distribution by a single Gaussian distribution:

$$\mathcal{G}(r^*; r_G) = r^{*2} \exp\left(-\frac{r^{*2}}{4r_G^2} \right), \tag{5.6}$$

where the Gaussian radius $r_G \approx 1fm$.

As a result we represent the total r^*–distribution of $\pi^-\pi^-$ pairs as a sum of four different contributions:

$$N_\omega \omega + N_{\eta'} \eta' + N_{\mathcal{G}} \mathcal{G} + (1 - N_\omega - N_{\eta'} - N_{\mathcal{G}}) \mathcal{M} \tag{5.7}$$

with altogether 14 parameters. The yields of individual contributions according to UrQMD simulation are listed in Table 5.3 and the individual parameterisations are shown in Figure 5.10.

In case of $\pi^+\pi^-$ pairs the parameterisations fail due to a significant admixture of the pairs born together in one resonance decay (Decay-one pairs). These pairs deform the shapes of particular spectra in the region of small r^*. Nevertheless, due to a similarity between the particular $\pi^+\pi^-$ and $\pi^-\pi^-$ spectra in the region of larger r^*, we can use the parameters for $\pi^-\pi^-$ pairs with an adequate proportion for each of the $\pi^+\pi^-$ contributions. The yield of Decay-one pairs should be included in the contribution of Direct pairs.

The ratios for individual contributions of $\pi^-\pi^-$ and $\pi^+\pi^-$ pairs are shown in Fig 5.11. We see that except of Mixed and Decay pairs the assumption of similarity of $\pi^-\pi^-$ and $\pi^+\pi^-$spectra is valid. The ratio of Mixed and Decay pairs shows a tiny slope.

So for both pairs, $\pi^-\pi^-$ and $\pi^+\pi^-$, we apply the same parameterisations of particular contributions. Differences between $\pi^-\pi^-$ and $\pi^+\pi^-$ spectra are

[5]The Coulomb FSI for $r^* \to 0$ is very well described by Coulomb penetration factor $A_c(\eta)$. The main contribution into the correction comes from contributions with $r^* \sim |a|$.

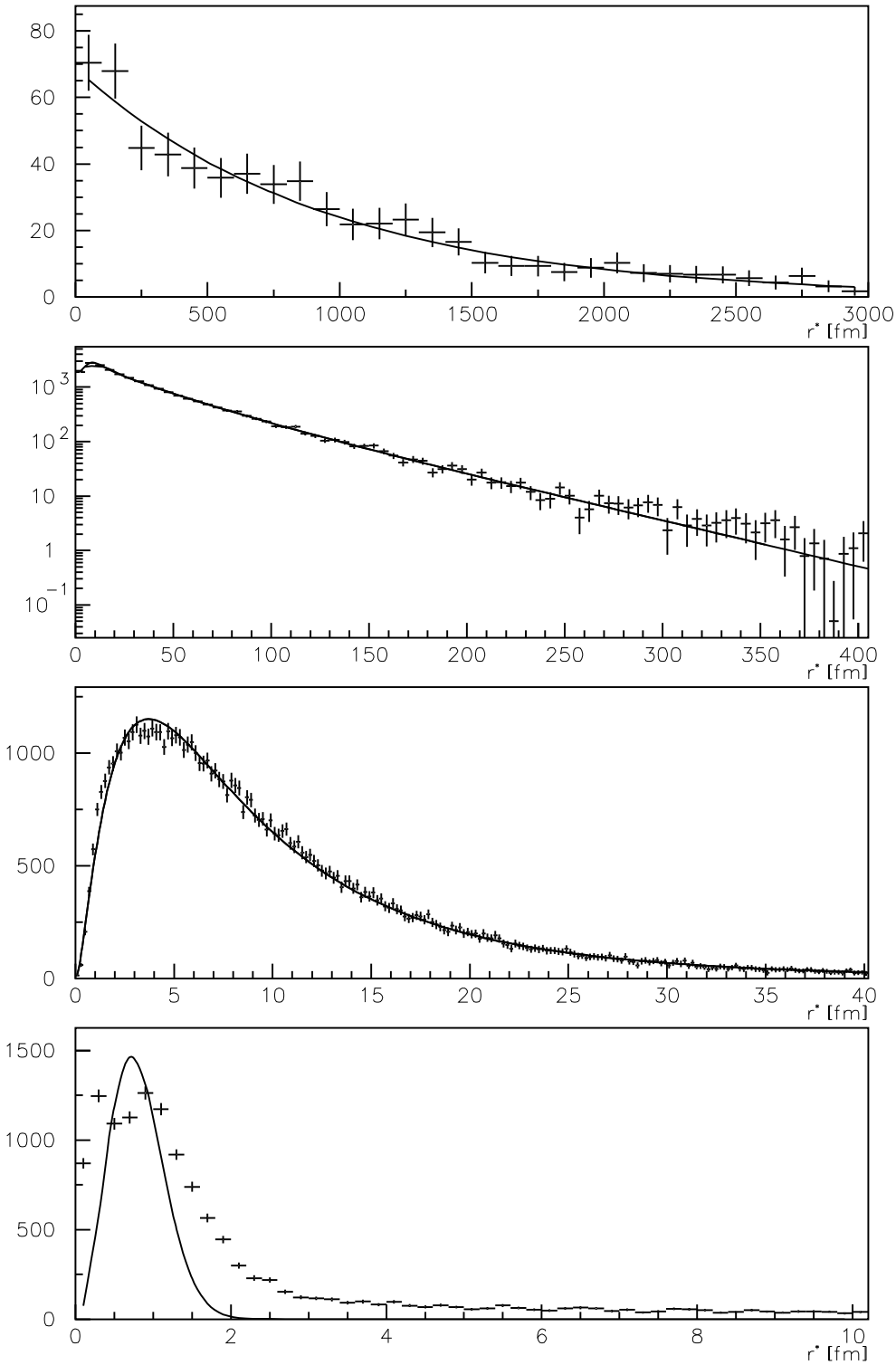

Figure 5.10: The distributions of r^* for individual groups of $\pi^-\pi^-$ pairs (points) and their parameterisations (curves). From top to bottom there are η' , ω , Decay with Mixed pairs (without η' and ω pairs) and Direct pairs, respectively.

Parameterisation	$q < 200 MeV/c$		$q < 15 MeV/c$	
	$\pi^-\pi^-$	$\pi^+\pi^-$	$\pi^-\pi^-$	$\pi^+\pi^-$
ω	20.4%	13.0%	20.8%	15.0%
η'	0.8%	0.5%	1.3 %	0.7 %
$\mathcal{M}$	65.9%	67.0%	63.7%	64.5%
$\mathcal{G}$	12,9%	19.5%	14.2%	19.8%

Table 5.3: The contributions of $\pi^-\pi^-$ and $\pi^+\pi^-$ groups described by particular parametrisation.

included in the different ratios of the individual contributions. They are listed in Table 5.3. Since the yields of the individual contributions slightly change with q, we are presenting here the yields for $q < 15 MeV/c$ in addition to the yields for $q < 200 MeV/c$. We will use them in a study of corrections for $A_{2\pi}$ analysis which is performed just in the interval $q \in (0; 15) MeV/c$.

5.2 Correlation Function

There are two possible ways to obtain information about correlation function from simulated data. The UrQMD code does not take into account the influence of FSI and QS so this influence must be additionally incorporated.

5.2.1 Weighted Spectra

Firstly for each simulated pair we provide the weight according to square of the pair wave function $\psi_{-\mathbf{k}^*}(\mathbf{r}^*)$ given by Eq.(2.42). Then we construct two q–distributions, one with and one without these weights. The ratio of these two spectra can be identified, under the smoothness assumption, with the correlation function. The correlation functions generated for each of individual groups of the $\pi^-\pi^-$ and $\pi^+\pi^-$ pairs are shown in Figure 5.12. The differences between $\pi^-\pi^-$ and $\pi^+\pi^-$ are obvious. The $\pi^+\pi^-$ pairs are mainly influenced by Coulomb attraction which leads to the enhancement of the pair production for small q, while the $\pi^-\pi^-$ pairs are subjected to Bose-Einstein statistics and Coulomb repulsion. The QS causes the enhanced pair production in relative wide region of q. The repulsion dominates for very small q which leads to a suppression in the pair production.

In this method the dependences between r^* ,P_p and q are taken into account. These dependences can significantly influence the final correlation function. In Figure 5.13 there are shown the r^*–distributions for two different q regions and their ratio. The r^*–distributions differ in the region of small r^* and in the most

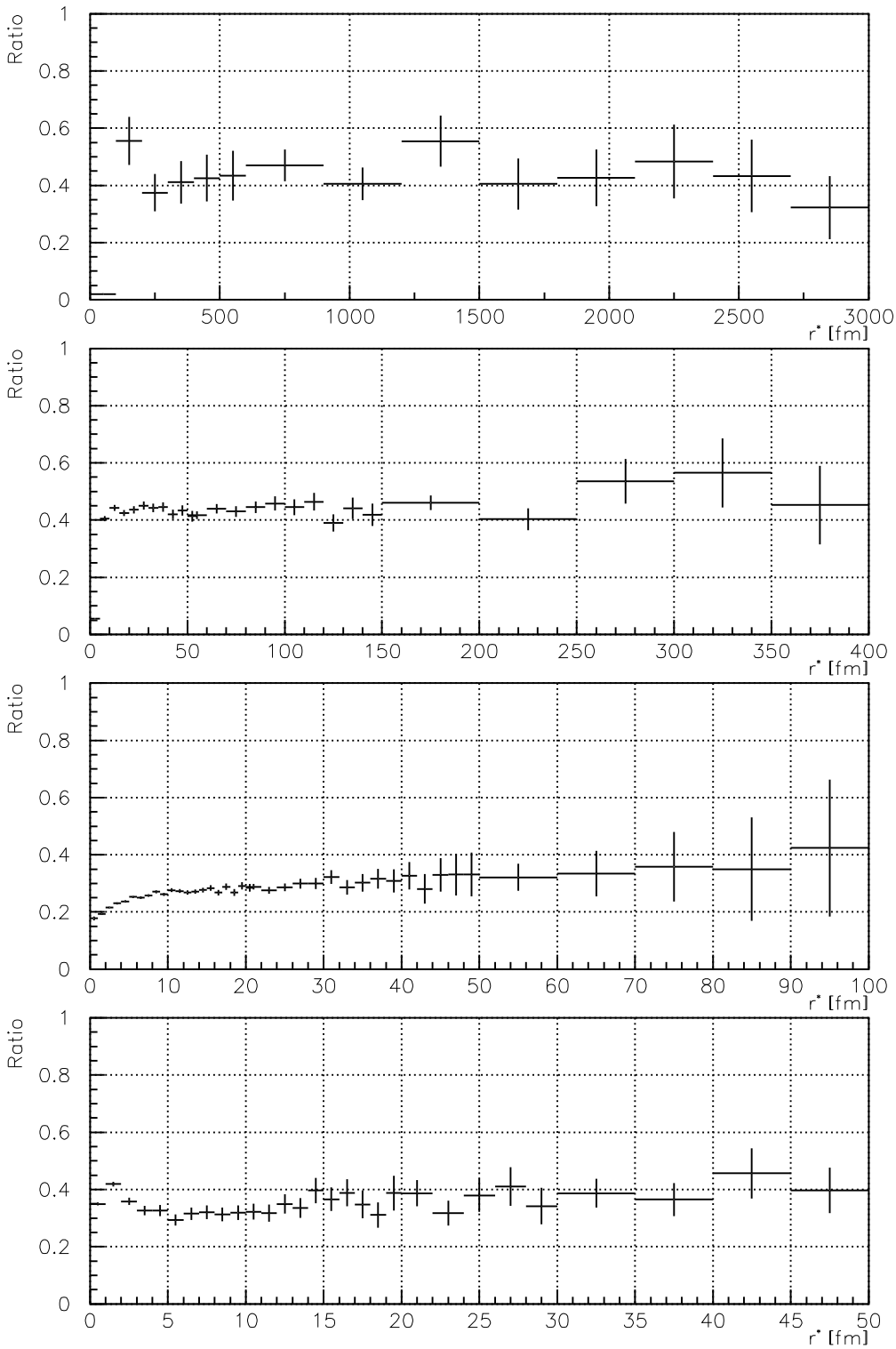

Figure 5.11: The ratios of $\pi^-\pi^-$ and $\pi^+\pi^-$ r^*–distributions for individual groups. From top to bottom there are η' , ω , Decay with Mixed pairs (without η' and ω pairs) and Direct pairs, respectively.

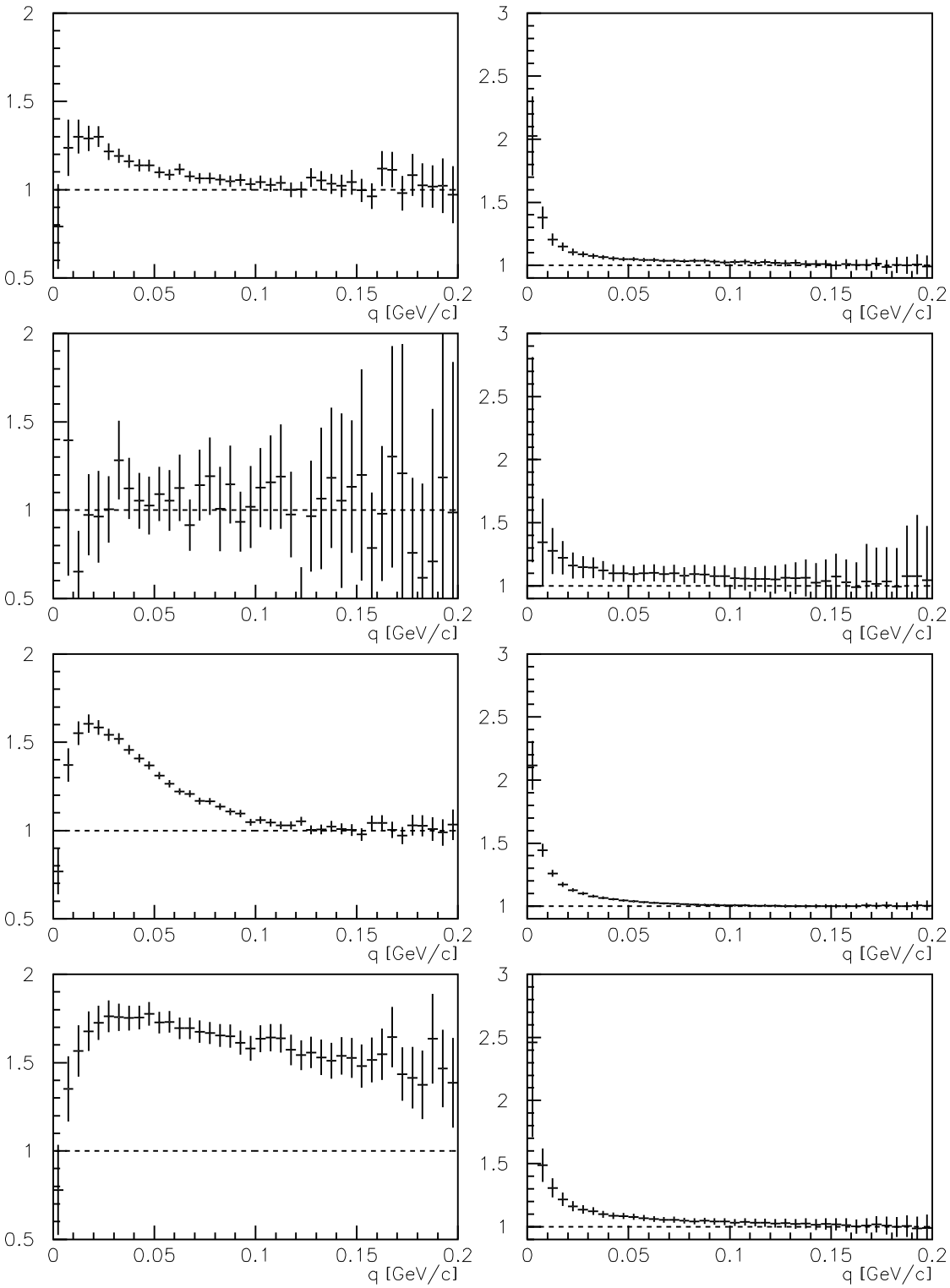

Figure 5.12: Correlation functions of individual types of $\pi^-\pi^-$ (Left) and $\pi^+\pi^-$ (Right) pairs constructed from UrQMD data by the weight method. From up to down are correlation function for ω, η', Direct and Mixed with Decay pairs, respectively.

important region of $r^* \sim |a|$ where the large errors prevent us to make any definite conclusion.

Figure 5.14 shows the relation of P_p and q for $\pi^+\pi^-$ pairs and in Figure 5.15 we can see the distribution of the angle between direction of vectors $\mathbf{r}^*$and $\mathbf{q}$ for four different bins of q. We see that the anisotropy of this distribution increases with q. This is mainly consequence of the small space acceptance of the secondary channel. For $q < 10MeV/c$, the acceptance of the set-up is practically independent of the direction of q but with the increasing q the directions related to the axis of the secondary channel (longitudinal direction) are preferred.

On the other hand the simulation of sufficient amount of data requires much computer time and variation of some features of the production mechanism is practically unfeasible. The simulated amount of data does not allow a detailed study of the dependences of P_p, $\mathbf{q}$ and $\mathbf{r}^*$mentioned above for $\pi^-\pi^-$ pairs. But we can suppose that behaviour of these pairs will be similar to $\pi^+\pi^-$ ones.

5.2.2 Numerical Computation

As the second possible method we can use the numerical computation of the correlation function according to Eq.(2.37). However, to be able to perform this task we need to accept some simplifications of the solved problem. The main simplification is in the assumption of an isotropic distribution of vector $\mathbf{q}$. It was shown in Figure 5.15 that this assumption is strongly violated for high q. In order to take into account this phenomenon we need to construct a 3-dimensional distribution of $\mathbf{q}$ and $\mathbf{r}^*$. For this analysis the significantly higher amount of simulated data must be available. Therefore, we neglect this and suppose the uniform distribution of the cosine of the angle between the vectors $\mathbf{q}$ and $\mathbf{r}^*$ for the uncorrelated pairs. This allows us to integrate over the directions of $\mathbf{q}$. After that the correlation effect is determined by the distribution of r^*, irrespective of its angular distribution. As another simplification we neglect the relatively weak dependence of r^*–distribution on q and P_p.

The advantages of this method are its rapidity and variability. The correlation function for a given r^*–distribution can be obtained practically immediately without long simulation. Moreover, the inaccuracies due to neglecting $\mathbf{q}$, $\mathbf{r}^*$and P_p dependencies can partially be compensated in fits of $\pi^-\pi^-$ correlation function. Due to the very high resolution of the spectrometer the effect of inaccuracy in experimental determination of q can be neglected here.

The correlation function obtained by this method can be compared with the one from the method of weights. The correlation function for ω and η' contributions are in a good agreement but in case of the $\mathcal{M}$ contribution, the differences are significant. Therefore we tried to find new parameters of power–like expression $\mathcal{M}(r^*; r_M, \alpha, \beta)$, defined by Eq.(5.5) in order to better approach the correlation function obtained from UrQMD data. The correlation functions corresponding to the original parametrisation of r^*–distribution of Mixed and Decay pairs and

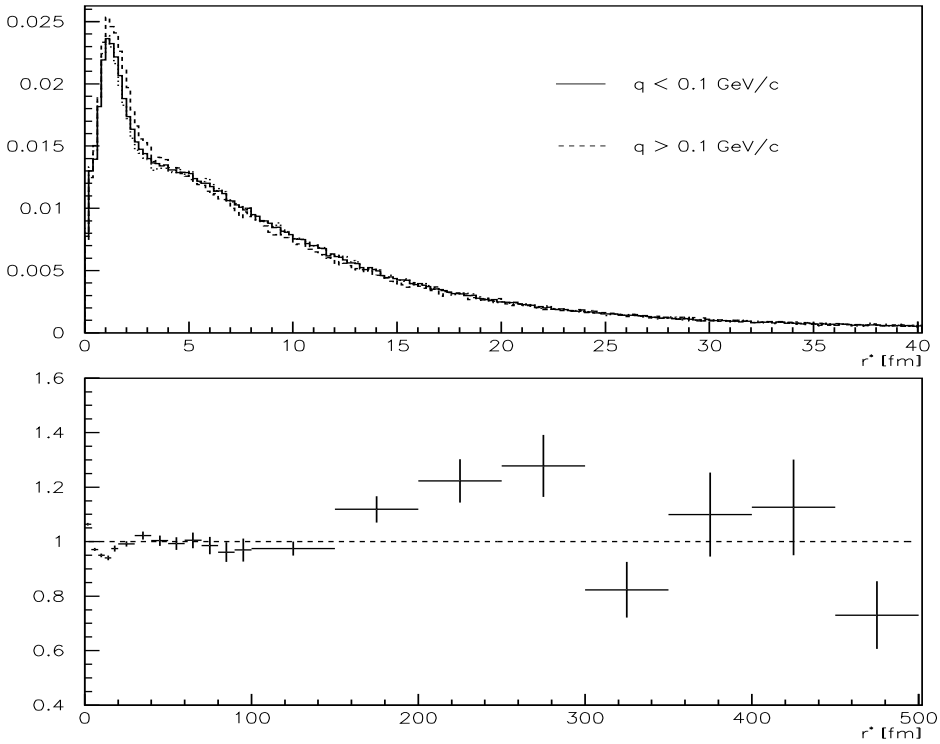

Figure 5.13: The r^*–distribution for $\pi^+\pi^-$ pairs with $q < 0.1 GeV/c$ and $q > 0.1 GeV/c$ (**Top**) and their ratio (**Bottom**).

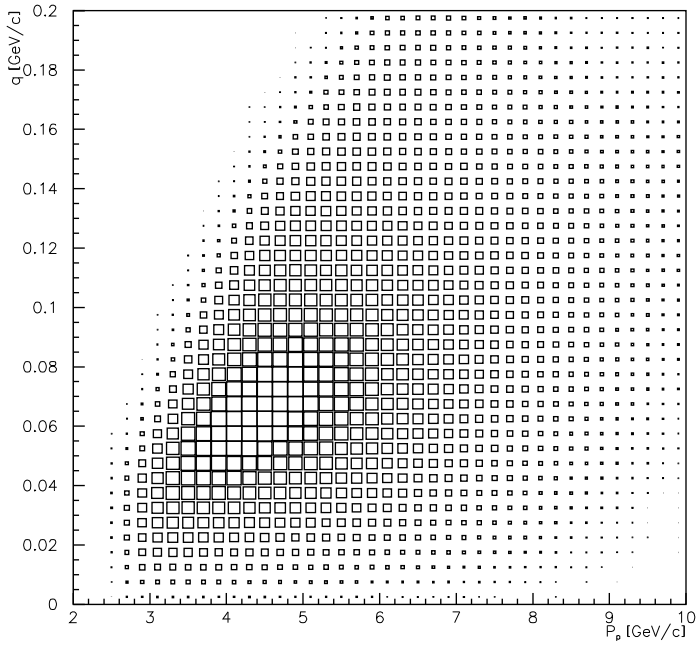

Figure 5.14: Relation between P_p and q for simulated $\pi^+\pi^-$ pairs.

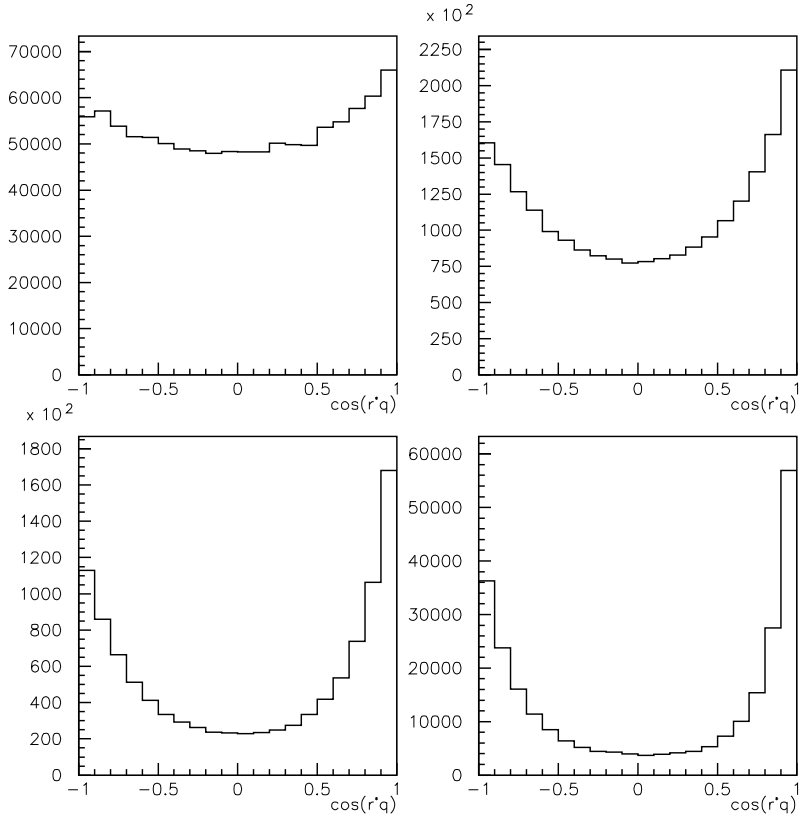

Figure 5.15: Distribution of the angles between **q** and **r*** for four different q bins: $(0.;0.05)$,$(0.05;0.10)$,$(0.10;0.15)$ and $(0.15;0.20)$ GeV/c.

new effective parametrisation (r_M = 10 fm, α = 0.9 and β = 2) are shown in Figure 5.16. Apart from the first three bins the new parametrisation describes the correlation function from UrQMD data very well. For a better description of the region of very small q the dependencies between vectors **q**, **r***and P_p must be taken into account.

The correlation functions obtained by the numerical method for all contributions of $\pi^-\pi^-$ and $\pi^+\pi^-$ pairs are shown in Figure 5.17.

5.2.3 Correction Factors

As it was mentioned in Section 3.3.1, the DIRAC experimental approach to production of $\pi^+\pi^-$ pairs and $A_{2\pi}$ atoms assumes that the pions are created either at zero or at very long distances. However, this approach is violated and a correction for production of Coulomb pairs and atomic pairs should be introduced according to Eqs.(3.18) and (3.19).

The correlation function of $\pi^+\pi^-$ pairs for individual contributions with respect to the simulated r^*–distributions and according to the DIRAC experiment

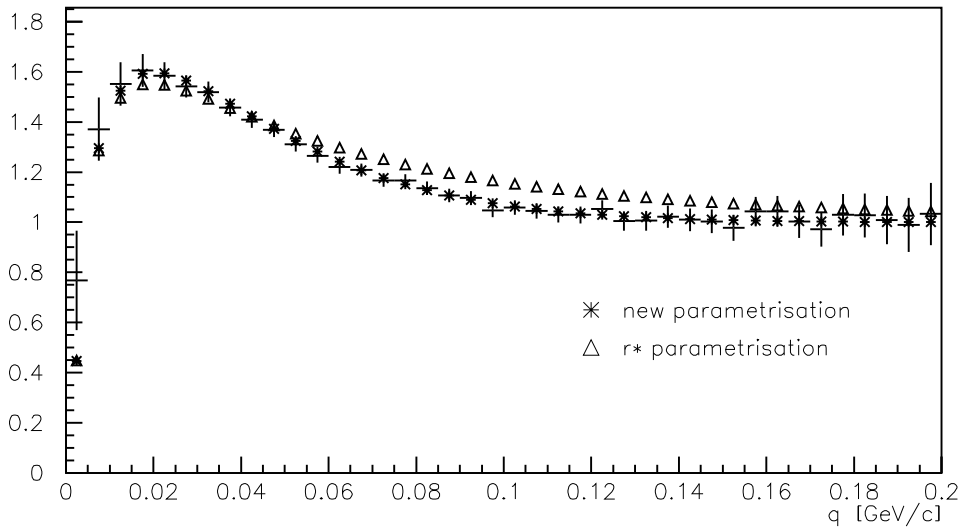

Figure 5.16: The $\pi^-\pi^-$ correlation function for Mixed and Decay pairs obtained from UrQMD data by the method of weights (crosses) and the correlation function numerically calculated for the original parametrisation of r^*–distribution (triangles) and for the effective one (asterisks).

approach are shown in Figure 5.18 together with the correction factor $1+\delta(\mathbf{k}^*)$.[6] We can see that for $\mathcal{M}$ and $\mathcal{G}$ contributions the correction factor $1+\delta(\mathbf{k}^*)$ has a nearly linear behaviour for q up to $40MeV/c$ and it is greater than one. This is due to the influence of strong FSI. On the contrary, the correction factor $1+\delta(\mathbf{k}^*)$ of ω and η' is smaller than unity. This is a consequence of larger production distances which induce weaker FSI interaction. In spite of this fact, both these contributions are significantly influenced by FSI and can not be included among long-lived sources. The correction factor for long-lived source behaves like $1+\delta(\mathbf{k}^*) = 1/A_c(\eta)$ and for $q \to 0$ it tends to zero.

In Figure 5.19 we plot the total correlation function corresponding to admixture of 15% of ω, 0.7% of η', 64.5% of $\mathcal{M}$ and 19.8% of $\mathcal{G}$ contributions together with function $A_c(\eta)$ which represents the correlation function in case of zero separation between emission points ($r^* = 0$). The bottom figure shows the total correction factor $1+\delta(\mathbf{k}^*)$. It should be noted that a constant correction factor $1+\delta(\mathbf{k}^*)$ can be absorbed in the normalisation parameter g in Eq.(3.11) and so the standard simple procedure of the lifetime extraction based on Eq.(3.11) could be safely used. A modification of this procedure is required only in the case when this factor substantially deviates from a constant.

In Figure 5.20 the correction factors $1+\delta_n$ for production cross section of

[6] The $\pi^+\pi^-$ pairs are due to a trigger restriction accepted up to $q \sim 40MeV/c$ and usually analysed up to $15MeV/c$. Therefore, the correlation function and corresponding corrections are shown in the interval of $q \in (0.; 40.)$.

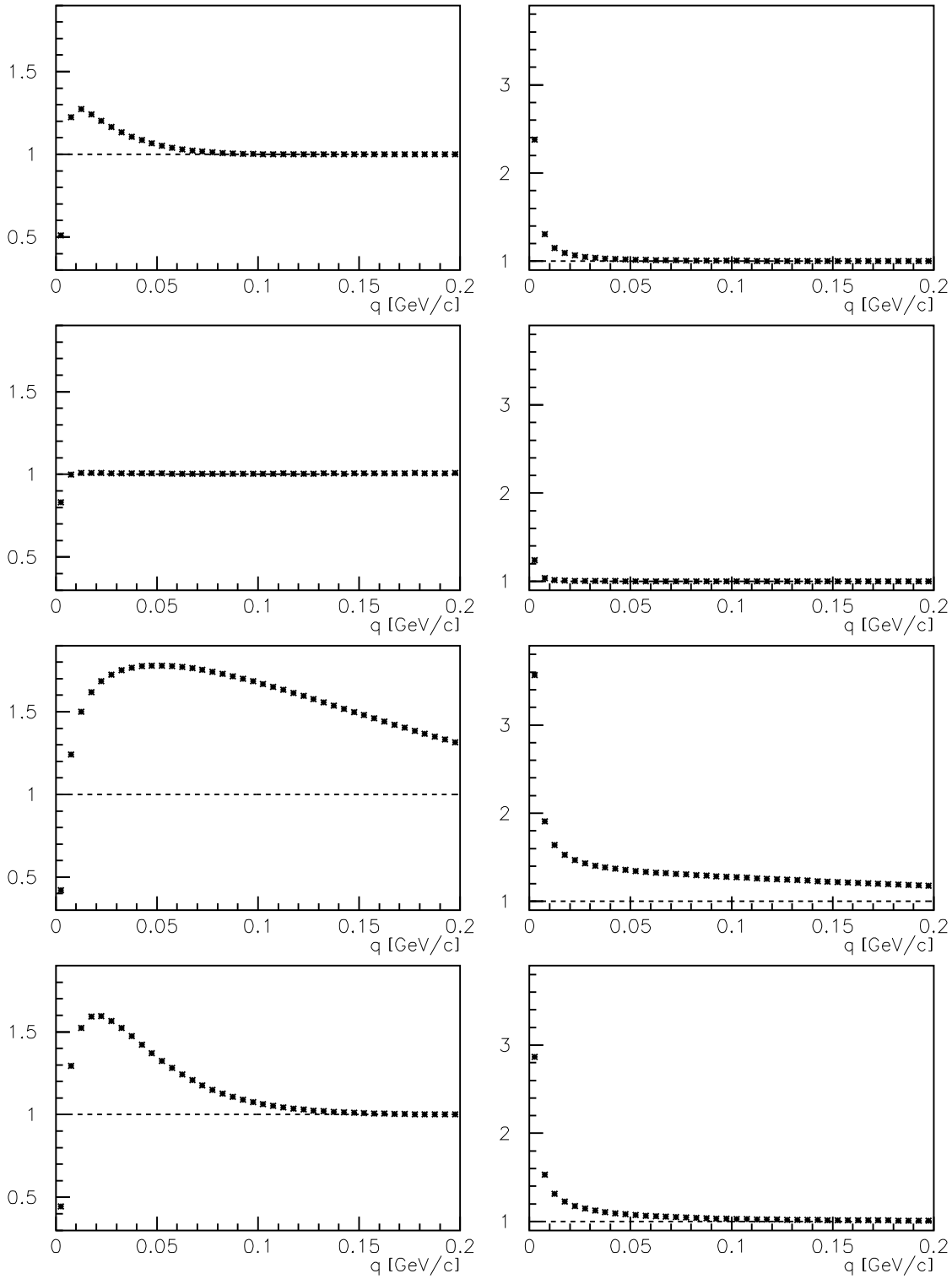

Figure 5.17: Correlation functions of individual types of $\pi^-\pi^-$ (**Left**) and $\pi^+\pi^-$ (**Right**) pairs numerically calculated using r^*–distribution from the UrQMD simulation. From top to bottom, results for ω, η', $\mathcal{G}$ and $\mathcal{M}$ pairs, respectively, are shown.

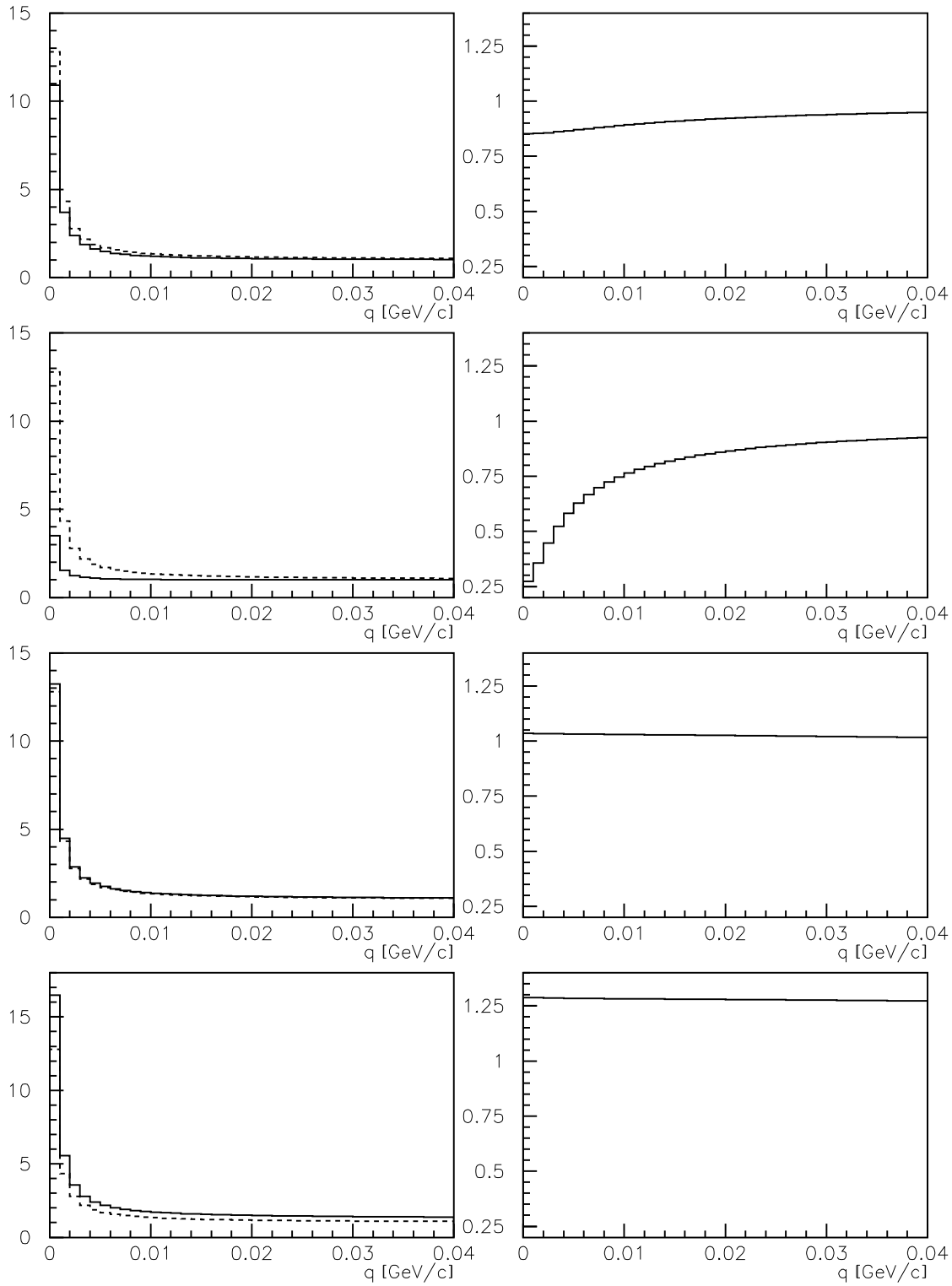

Figure 5.18: Left: The $\pi^+\pi^-$ correlation functions obtained according to simulated r^*–distribution (full line) and on condition of zero space–time separation between production points (dashed line) for interval $q \in (0; 0.04) GeV/c$. Right: Correction factor $1 + \delta(\mathbf{k}^*)$. From top to bottom, results for ω, η', $\mathcal{G}$ and $\mathcal{M}$ pairs, respectively, are shown.

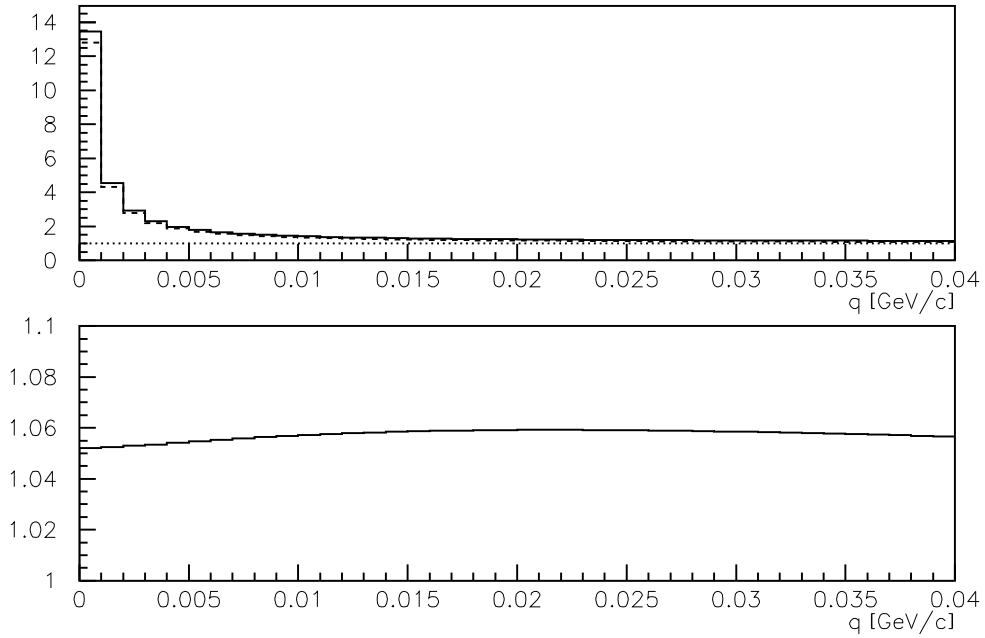

Figure 5.19: The $\pi^+\pi^-$ correlation function corresponding to the mixture of 15% of ω, 0.7% of η', 64.5% of $\mathcal{M}$ and 19.8% of $\mathcal{G}$ contributions (full line) and the correlation function with the assumption of zero separation between production points (dashed line) (**Top**). Corresponding correction factor $1+\delta(\mathbf{k}^*)$ (**Bottom**).

$A_{2\pi}$ atoms (Eq.(3.12)) determined according to Eq.(3.19) for the individual contributions are shown. We see an enhancement in $A_{2\pi}$ production for $\mathcal{M}$ and $\mathcal{G}$ contributions and a suppression for ω and η' contributions. The right panel in Figure 5.20 demonstrates a violation of Migdal relation in Eg.(3.20).

The same functions as in Figure 5.20 computed for admixture of 15% of ω, 0.7% of η', 64.5% of $\mathcal{M}$ and 19.8% of $\mathcal{G}$ contributions are shown in Figure 5.21. We can see that in this case the Migdal's relation is fulfilled up to a correction of the order of 10^{-3}.

The deviation of the ratio $(1+\delta_n)/(1+\delta(0))$ from unity leads to a correction in the value of k_{th}–factor. This factor defined in Eq. (3.15) is used for determination of the number N_A of produced $A_{2\pi}$ atoms from the measured number of Coulomb pairs n_{CC}. Figure 5.21 shows that the correction of k_{th}–factor does not exceed a fraction of a percent.

5.3 Resume

The simulation of distributions of the distances r^* between emission points in the $\pi^+\pi^-$ and $\pi^-\pi^-$ pair c.m.s. has been performed using modified UrQMD code [41]. Considering the finite size corrections to $A_{2\pi}$ lifetime measurement

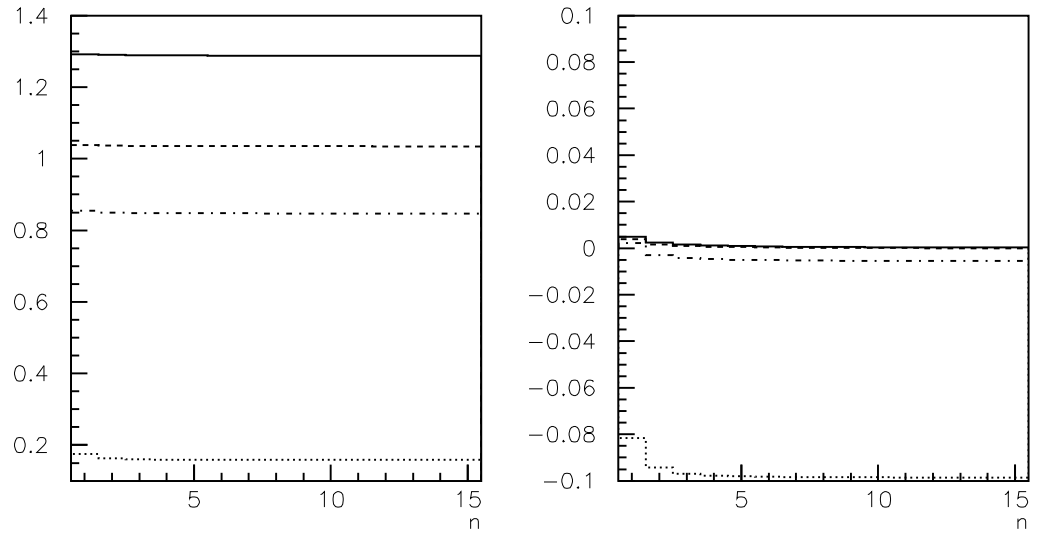

Figure 5.20: The correction factor $1 + \delta_n$ for individual contributions of $\pi^+\pi^-$ pairs as a function of main atomic quantum number n. In decreasing order they correspond to $\mathcal{G}$, $\mathcal{M}$, ω and η' contributions (**Left**). The differences $\delta_n - \delta(0)$ for each contribution (**Right**).

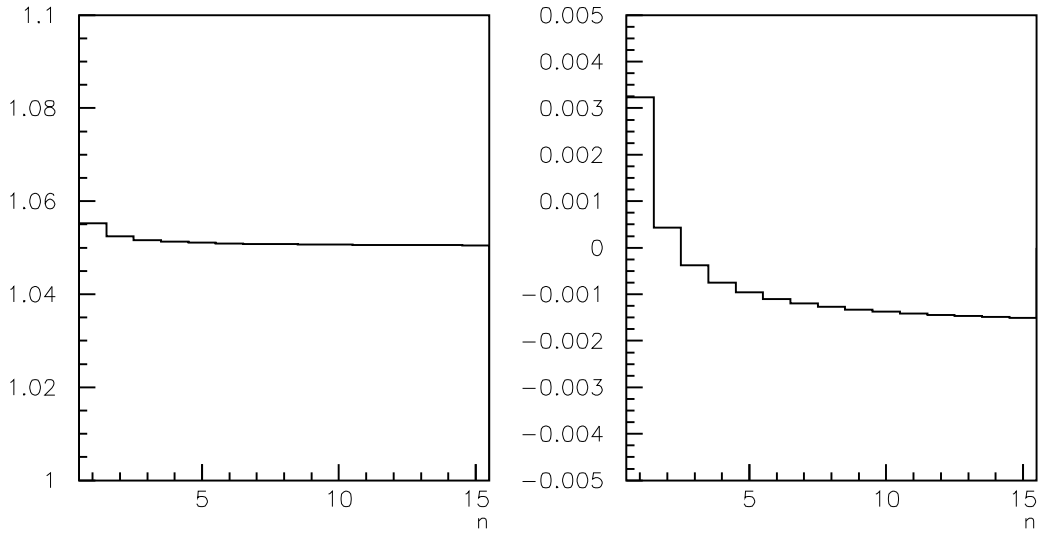

Figure 5.21: The correction factor $1 + \delta_n$ corresponding to the mixture of 15% ω, 0.7% η', 64.5% $\mathcal{M}$ and 19.8% $\mathcal{G}$ contributions (**Left**) and the corresponding difference $\delta_n - \delta(0)$ (**Right**).

we have found four specific contributions into these distributions. For each of these contributions the correlation function and a corresponding correction to the DIRAC approach have been numerically computed. The simulated yields of these four contributions for $\pi^+\pi^-$ and $\pi^-\pi^-$ pairs are listed in Table 5.3 and their characteristics can be described as follows:

$\mathcal{G}$ pairs

These pairs consist of pion pairs produced in direct processes, rescatterings or in decays of one and the same resonance. They are characterised by small r^* peaked at about $1fm$. We parametrised them by Gaussian distribution in Eq.(5.6) with radius of $1fm$. Though the corresponding correction factor $1+\delta(\mathbf{k}^*)$ is significantly different from unity, it is close to a constant up to a small linear slope which is almost independent of the Gaussian radius and can be easily incorporated in the standard procedure of the lifetime determination based on Eq.(3.11). Therefore, these pairs practically do not contribute to the studied systematic shift in the measurement of $A_{2\pi}$lifetime.

$\mathcal{M}$ pairs

They are pion pairs with at least one pion coming from the resonance decay (except for ω and η' resonances). Their r^*–distribution is peaked at around $4fm$ and has a noticable tail. It can be parametrised by power–like expression in Eq.(5.5). Similar to the $\mathcal{G}$–pairs, the corresponding correction factor $1+\delta(\mathbf{k}^*)$ is close to a constant up to a small linear slope which can be incorporated in the simple standard procedure based on Eq.(3.11). Therefore, these pairs hardly bring any systematic shift in the corresponding extracted value of the $A_{2\pi}$lifetime.

η' pairs

These pairs contain at least one pion which is created in η' decay. The characteristic path length of η' is about $900fm$ so their r^*–distribution extends up to thousands of fm. We parametrised it by a single exponential formula in Eq.(5.2). These pairs contribute to the total r^* distribution in the critical region of $r^* \sim |a|$ ($|a| = 387fm$). But the corresponding correction factor $1+\delta(\mathbf{k}^*)$ is to a large extent absorbed by the parameter $(1-\lambda)$ describing the contribution of long-lived sources in Eq.(3.11). Moreover, the yield of these pairs is about 1% so they also do not play a crucial role in the systematic shift of $A_{2\pi}$lifetime determination.

ω pairs

They are formed by pairs containing at least one pion produced in ω decay (except for pions from η' decays). The characteristic path length of ω is about 30 fm. Therefore, the tail of the corresponding r^*–distribution significantly extends

to the region of $r^* \sim |a|$. This distribution is parametrised by two exponential formula in Eq.(5.4). The corresponding correction factor $1 + \delta(\mathbf{k}^*)$ shows a non-linear behaviour and is also far from the correction factor for long-lived sources which behaves like $1/A_c(\eta)$. Therefore, the factor $1 + \delta(\mathbf{k}^*)$ cannot be absorbed in the parameters of the lifetime extraction procedure based on Eq.(3.11). Moreover, the yield of ω pairs is about 15% (for $\pi^+\pi^-$ pairs) so that these pairs form the crucial contribution to the systematic shift in $A_{2\pi}$lifetime determination.

The analysis of the correction $1+\delta_n$ to the standard calculation of the number of produced $A_{2\pi}$atoms based on Eg.(3.12) shows that for $\mathcal{G}$, $\mathcal{M}$ and ω contributions the Migdal's relation $\delta_n = \delta(\mathbf{k}^* = 0)$ is only slightly violated on a level of 10^{-3}. The strong violation of Migdal's relation in case of η' pairs can be neglected due to a small yield of this contribution and due to the fact that it is partly absorbed in the fitted contribution of long-lived sources. This implies that the ratio $(1 + \delta_n)/(1 + \delta(0))$ is close to unity and k_{th}–factor used for evaluation of a number of produced $A_{2\pi}$atoms is only slightly affected by the finite size correction.

Based on the UrQMD simulations, we can conclude that the main source of the systematic shift in the $A_{2\pi}$ lifetime determination is formed by ω pairs.

Chapter 6

Data Analysis

As a by-product, experiment DIRAC provides a high statistics data on the correlation functions of identical charged pions. These functions contain information about the space-time characteristics of the pion production region and can be used to check the predictions of the UrQMD simulations.

The basic idea of construction of the correlation function is based on a direct application of its definition (Eq. 2.1). The spectrum of prompt pion pairs is used as a nominator and the spectrum of accidental ones as a denominator. The prompt pairs are pairs of pions coming from one primary interaction. They are influenced by FSI and QS.[1] For a reference spectrum the accidental ones are used. They consist of pions from two different primary interactions. Therefore, their spectrum is not affected by FSI and QS. Of course, the different kinematic conditions of prompt and accidental pairs must be taken into account and the appropriate corrections must be applied.

Data are analysed with the help of the DIRAC analysis software package ARIANE [42] in 304_33 version. During reconstruction of track momenta an information from Drift Chambers (DC) and a requirement of the common vertex in the target are only used. The information from the upstream detectors is not taken into account due to anomalous behaviour of the standard upstream tracking code[2] in case of $\pi^-\pi^-$ analysed pairs.

6.1 Data selection

Since the experimental set-up is dedicated to the measurement of $\pi^+\pi^-$pairs and no special trigger for the measurement of $\pi^-\pi^-$or $\pi^+\pi^+$ pairs is introduced we use the events with standard T4+DNA trigger mark. This trigger (see Section 4.5) selects events with two opposite charged pion-like tracks with small relative mo-

[1]Contrary to $\pi^+\pi^-$ pairs where only Coulomb and strong FSI are involved.

[2]This code is optimised for $\pi^+\pi^-$pairs with q up to 30 MeV/c while the q of registered $\pi^-\pi^-$ pairs is up to 200 MeV/c.

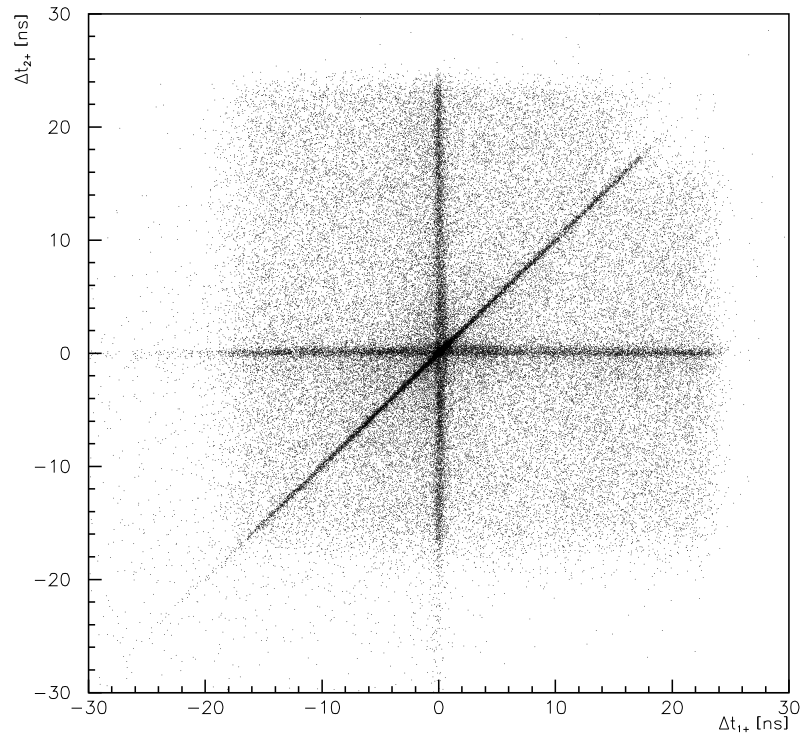

Figure 6.1: The time distribution of two π^- with regard to timing of π^+. The horizontal and the vertical lines correspond to prompt pairs consisting of π^+ and π^-. The diagonal line is formed by $\pi^-\pi^-$prompt pairs. Values Δt_{1+} and Δt_{2+} represent time differences between the π^+ and the first π^- and between the π^+ and the second π^-, respectively.

menta $q \lesssim 30 MeV/c$. The extra tracks in both positive and negative arms are allowed. This makes possible to extract $\pi^-\pi^-$and $\pi^+\pi^+$ pairs from these events. Moreover, the q of these pairs is not influenced by the restrictive trigger selection criteria and is constrained only by the angular acceptance of the secondary channel and by the momentum acceptance of the spectrometer system.

For further analysis the 2001 Ni data are chosen and, in the following, we focus only on $\pi^-\pi^-$pairs and their correlation function. The measured positive pion-like tracks contain a significant admixture of protons which deform the shape of $\pi^+\pi^+$ correlation function.

From all of the T4+DNA data we further choose only the events with two reconstructed DC tracks in the negative arm of the spectrometer and one DC track in the positive arm. The absence of electron trigger flag and a signal in muon detectors was checked to minimise a possible contamination by electron and muon pairs.

Prompt and Accidentals Pairs

The topology of $\pi^-\pi^-$events is more complicated than in case of $\pi^+\pi^-$pairs. Each selected event consists of three particles, two π^- and one π^+. There are three possible couples of pions which can originate from one primary interaction (prompt pairs - influenced by FSI and QS) or from two different interactions (accidental pairs - not influenced by FSI and QS), see Fig 6.1. Moreover, the kinematic characteristics of pions from prompt and accidental pairs differ due to a different phase-space.

Since we are interested in $\pi^-\pi^-$correlation function we need to extract the prompt and accidental $\pi^-\pi^-$ pairs from data. For a good understanding of the mutual relations between all three pions we demand that the remaining π^+ is accidental with respect to either of π^-. This is achieved by applying the cut on a difference between times of flight out from the target of π^+ and each of π^-, $|\Delta t_+| > 5\ ns$. The Δt_+ distribution is shown in Fig 6.2. The timing is performed by Vertical Hodoscope and corrected for the time of flight from the target.

The $\pi^-\pi^-$ pair is accepted as a prompt if the time difference between these pions is $|\Delta t_{--}| < 0.5ns$ and as an accidental if $|\Delta t_{--}| > 5ns$. These cuts are similar to the criteria which are applied for the selection of $\pi^+\pi^-$ pairs during the determination of $A_{2\pi}$ lifetime.

Summary of the selection criteria

Let us summarise the criteria for the event selection:

- T4+DNA trigger
- no electron trigger mark
- two reconstructed negative DC tracks and one positive DC track
- no muon signal corresponding to a negative track
- $5ns$ time gap between the positive track and any negative track
- $|\Delta t_{--}| < 0.5ns$ for prompt events
- $|\Delta t_{--}| > 5ns$ for accidental events

6.2 Correlation Function

The $\pi^-\pi^-$correlation function can be constructed as a ratio of prompt and accidental $\pi^-\pi^-$ events. Before this, however, two important phenomena must be taken into account. Firstly, the prompt events chosen according to the time condition $|\Delta t_{--}| < 0.5ns$ contain an indispensable admixture of accidental pairs.

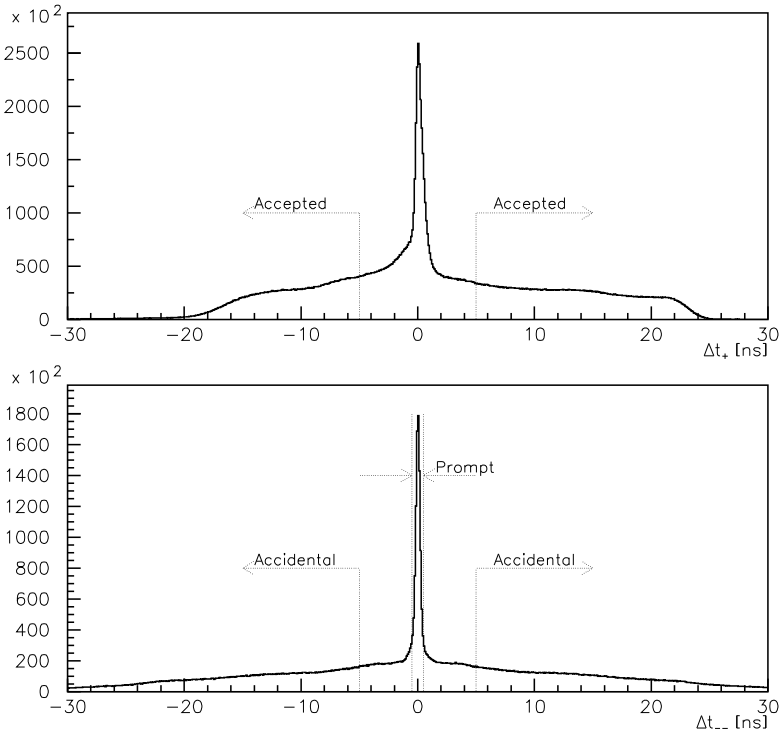

Figure 6.2: Time difference between π^- and π^+ (**Top**) and between two π^- (**Bottom**).

Secondly, the correction for different total pair momentum spectra of accidental and prompt pairs must be introduced.

The logic of the trigger system induces the linear shape of $|\Delta t_{--}|$ distribution of accidental $\pi^-\pi^-$pairs.[3] Therefore, we fit the measured $|\Delta t_{--}|$ distribution in the interval $|\Delta t_{--}| \in < 5; 10 > ns$ by a linear function and extrapolate this function under prompt pairs peak $|\Delta t_{--}| < 0.5ns$ (Fig. 6.3). The yield of accidental pairs in prompt pairs is 19.2% with an accurancy of 1%. This error is due to nonlinearity of the distribution of accidental pairs which is caused by the trigger electronics.

The spectra of total pair momenta P_p for both prompt and accidental pairs are shown in Fig. 6.4. We see that the spectrum of accidental pairs is shifted towards higher P_p. This is an effect of the difference of phase-space of production processes of these two types of pairs. Pions of the prompt pairs are produced in one interaction with the incident laboratory energy of 24 GeV/c while pions of accidental pairs are produced in two primary interactions each with the incident energy of 24 GeV/c. In case of sufficiently large space acceptance this will not play a crucial role but in case of the acceptance of DIRAC set-up it causes a visible

[3] In case of $\pi^+\pi^-$ accidental pairs, their $|\Delta t_{+-}|$ has a flat behaviour.

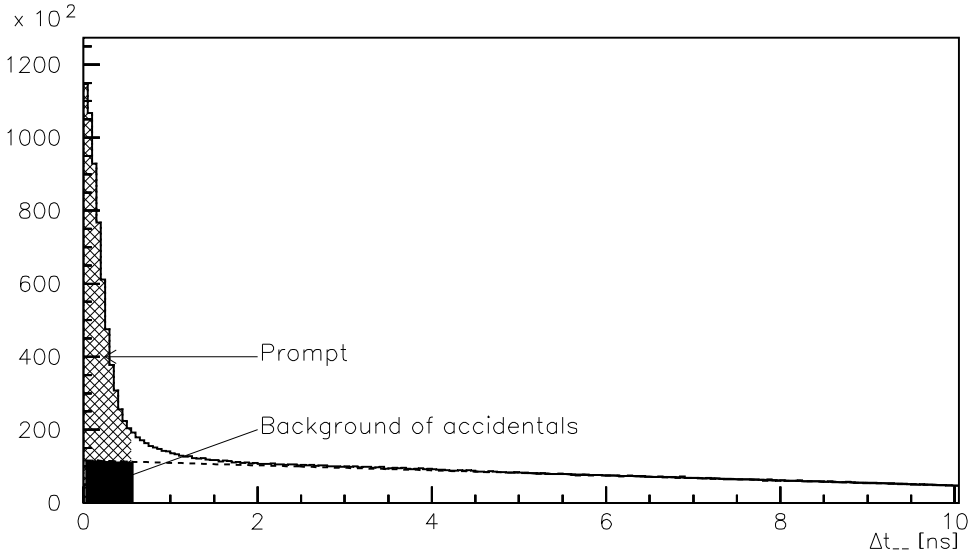

Figure 6.3: The time difference distribution $|\Delta t_{--}|$ between two π^- with fitted linear shape of accidental pairs.

effect. Since higher P_p leads to higher q of pairs this effect can have significant influence in the final correlation function.

To remedy this problem we introduce the weights corresponding to the ratio of the P_p distribution of the prompt and the accidental pairs (bottom part of Fig. 6.4). During the construction of an accidental q–spectrum we weigh each accidental event by the appropriate weight according to the pair P_p.

In case of similarity between P_p spectra we can neglect the admixture of accidental pairs in prompt pairs spectra as it will have the same behaviour as pairs from long-lived sources and will not deform the shape of the correlation function. However, in case of introduction of weighing of accidental pairs the behaviour of the accidental admixture is hardly predictable. That is why this admixture should be subtracted from all prompt pair spectra. (Not only from the q–spectrum but also from P_p one used to determine the weights.)

Finally, the q–spectrum cleaned of the prompt pairs is divided by weighted accidental q–spectrum whereby the correlation function is obtained (see Fig 6.5). We see the typical behaviour - the enhanced production of $\pi^-\pi^-$ pairs with decreasing q as a consequence of Bose-Einstein statistics and a strong fall of $\pi^-\pi^-$production in the region of small q due to Coulomb repulsion.

The influence of uncertainty in determination of admixture of the accidental pairs in the prompt spectra is shown in Fig 6.6. We see that the error due to this uncertainty is much smaller than the statistical error but, as a whole, it can generate a small slope in a shape of the correlation function.

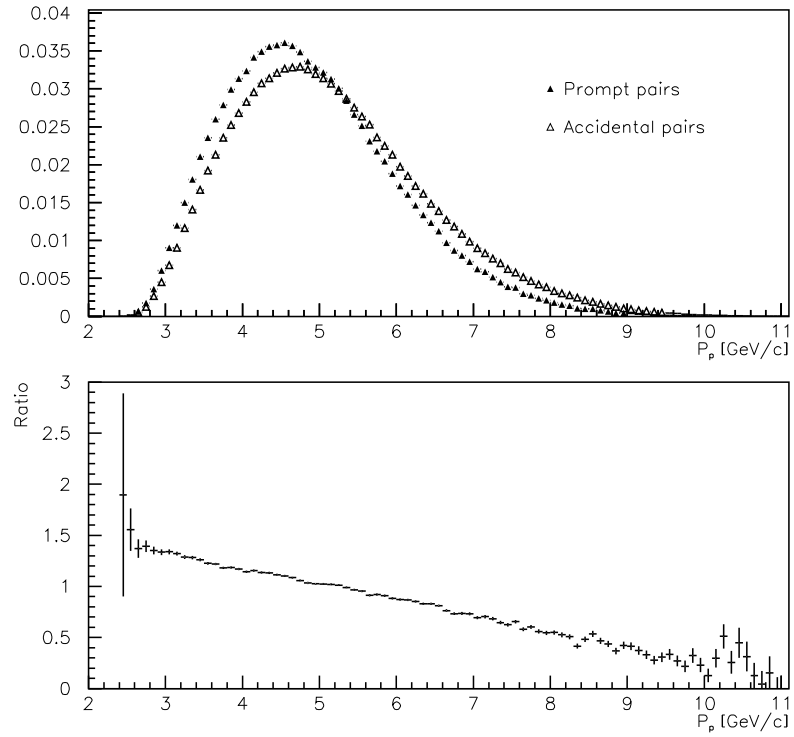

Figure 6.4: Normalised spectra of total pair momenta of prompt and accidental $\pi^-\pi^-$ pairs (**Top**) and their ratio (**Bottom**). The prompt spectrum is cleaned of the admixture of accidental pairs.

Summary of the construction of the correlation function

Let us summarise the steps of the construction of the correlation function

1. The P_p spectra of prompt and accidental events are extracted. The admixture of accidental pairs ($19.2 \pm 1\%$) is removed from the prompt spectrum.

2. The weights of accidental pairs are calculated based on the prompt and accidental P_p spectra.

3. The q–spectra of prompt and accidental (not weighted) pairs are constructed. The admixture of accidentals (19.2%) is subtracted from the prompt spectrum.

4. The weighted q–spectrum of accidental pairs is constructed.

5. The correlation function is obtained as the ratio of cleared prompt q–spectrum and weighted q–spectrum of accidentals.

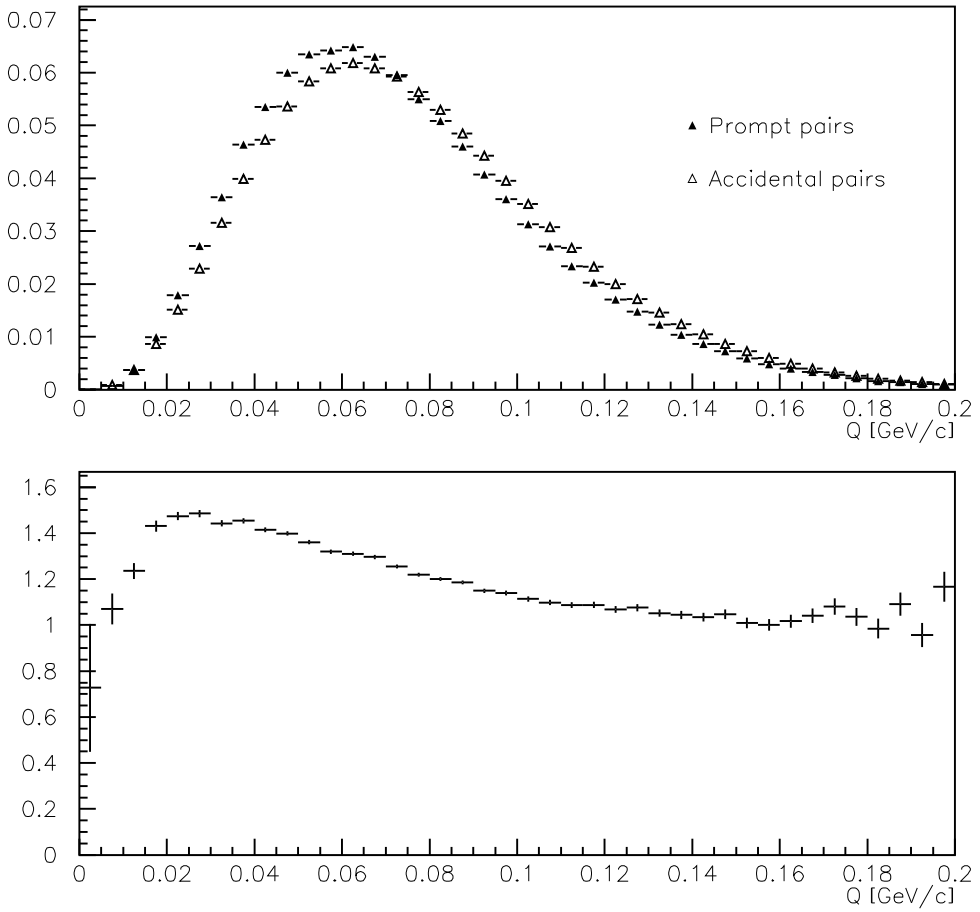

Figure 6.5: Normalised q–spectra of the cleared prompt pairs and the weighted accidental pairs (**Top**) and their ratio - the $\pi^-\pi^-$ correlation function. It is normalised to be ~ 1 for $q \to 0.2 GeV/c$ (**Bottom**).

6.3 Fit of $\pi^-\pi^-$ correlation function

A comparison of measured $\pi^-\pi^-$ correlation function with that constructed according to the results of UrQMD simulation provides a possibility to check the reliability of the simulation. Note that the most important contribution in the systematic shift of the $A_{2\pi}$lifetime measurement comes from ω pairs. Therefore, we mainly concentrate on the yield of these pairs.

In analysis of the simulated r^*–distribution, we identify four specific contributions: ω, η', $\mathcal{M}$ and $\mathcal{G}$. Since the r^*–distributions of ω and η' contributions are mainly determined by their known physical characteristics such as widths, masses and p_t and y spectra, we can suppose that their description by UrQMD simulation matches with the physical reality.

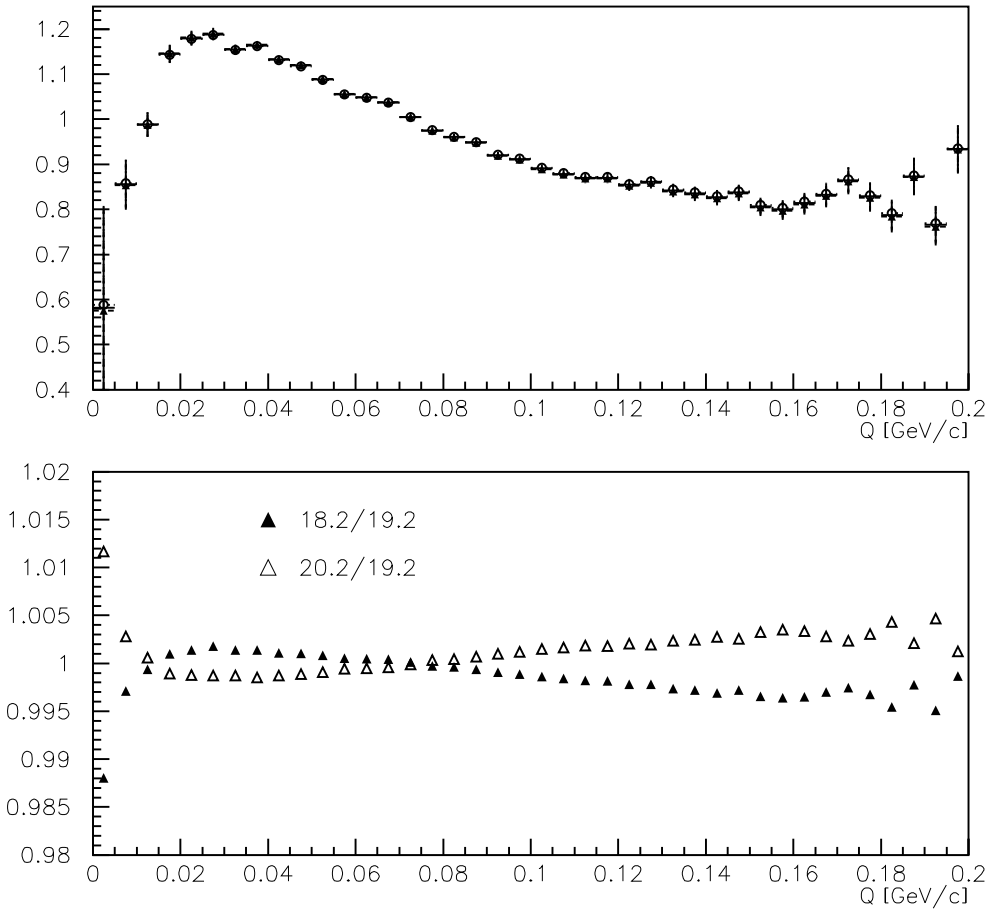

Figure 6.6: The influence of the uncertainty of the admixture of accidentals in prompt pairs. Three correlation function constructed for the value of the admixture 18.2%, 19.2% and 20.2%, respectively (**Top**). The ratios of these three function are shown in **Bottom**.

$\mathcal{G}$ contribution contains only pairs with very small r^*, peaked at about $1fm$, the possible variation of its r^*–distribution can bring only a small effect in the correlation function. Therefore, we accept their description obtained from the analysis of the simulated r^*–spectra.

The uncertainties of UrQMD model can mainly manifest themselves in $\mathcal{M}$ contribution. Moreover, this contribution is sensitive to the simplification in the numerical method used to evaluate an corresponding correlation function. Therefore, the parameters of $\mathcal{M}$ distribution are treated as free.

The measured $\pi^-\pi^-$ correlation function will be fitted by the following formula

$$\mathcal{F}(q) = N_{all}(1 + sq)\cdot \tag{6.1}$$

$$\cdot\{\lambda[(1-N_\omega-N_{\eta'}-N_\mathcal{G})C_\mathcal{M}(q;r_\mathcal{M},\alpha,\beta)+N_\omega C_\omega(q)+N_{\eta'}C_{\eta'}(q)+N_\mathcal{G}C_\mathcal{G}q]+(1-\lambda)\},$$

where $C_\mathcal{M}(q;r_\mathcal{M},\alpha,\beta)$, $C_\omega(q)$,$C_{\eta'}(q)$ and $C_\mathcal{G}(q)$ stand for correlation functions numerically calculated for $\mathcal{M}(q;r_\mathcal{M},\alpha,\beta)$, ω, η' and $\mathcal{G}$ distribution, respectively. The free parameters N_ω, $N_{\eta'}$ and $N_\mathcal{G}$ determine the yields of individual contributions and $(1-\lambda)$ describes the admixture of long-lived sources and misidentified particles. The linear slope s is included in the fitting formula to absorb a possible influence of an admixture of accidental pairs in prompt ones and other possible distorting effects.

The fitting function contains 9 free parameters. The determination of the free parameters of $\mathcal{M}$ distribution, $r_\mathcal{M}$,α,β, is performed by quadratic interpolation between correlation functions corresponding to three different values of each of these parameters, i.e. between 27 corresponding numerically calculated correlation functions.

The fitting procedure is performed for three measured correlation functions obtained from the measured data with the three estimated values of admixture of accidental background in prompt pairs, $19.2 \pm 1\%$. The fit of the full range of the correlation functions yields unreasonable values of the parameters, particularly $N_\omega \approx 0$. The failure of fitting procedure is probably caused by the simplifications used in the method of numerical calculation which manifest itself mainly in the first three bins of correlation function corresponding to $\mathcal{M}$ contribution (It can be seen as a difference between the correlation function obtained by the method of weights and the numerical calculation shown in Figure 5.16). After skipping the first three bins from the fit, the reasonable results are obtained. They are presented in Table 6.1.

It is important that the fitted value of N_ω agrees with the one predicted by the UrQMD simulation (20.4 %). The values of the parameters corresponding to $\mathcal{M}$ distribution differ from those obtained in our analysis of the simulated r^*–distribution (r_M = 10 fm, α = 0.9 and β = 2.). This discrepancy may be a consequence of the simplification in the method of numerical calculation or uncertainties in UrQMD model. The value of parameter s is rather high and implies the existence of a distorting effect in the measured correlation function.

The normalisation factors $N_{\eta'}$ and $N_\mathcal{G}$ are determined with high relative errors. It means that the fitting procedure is not sensitive to η' and $\mathcal{G}$ contributions. In case of η' contribution it is a consequence of the exclusion of the first three bins of q from fitting procedure. As it is seen from Figure 5.17 the corresponding correlation function significantly differs from unity only in the first bin. Besides the exclusion of the first three bins, the possible variation of $\mathcal{M}$ parameters together with the introduced linear slope can cause that the correlation function corresponding to $\mathcal{M}$ contribution together with linear slope partially describes

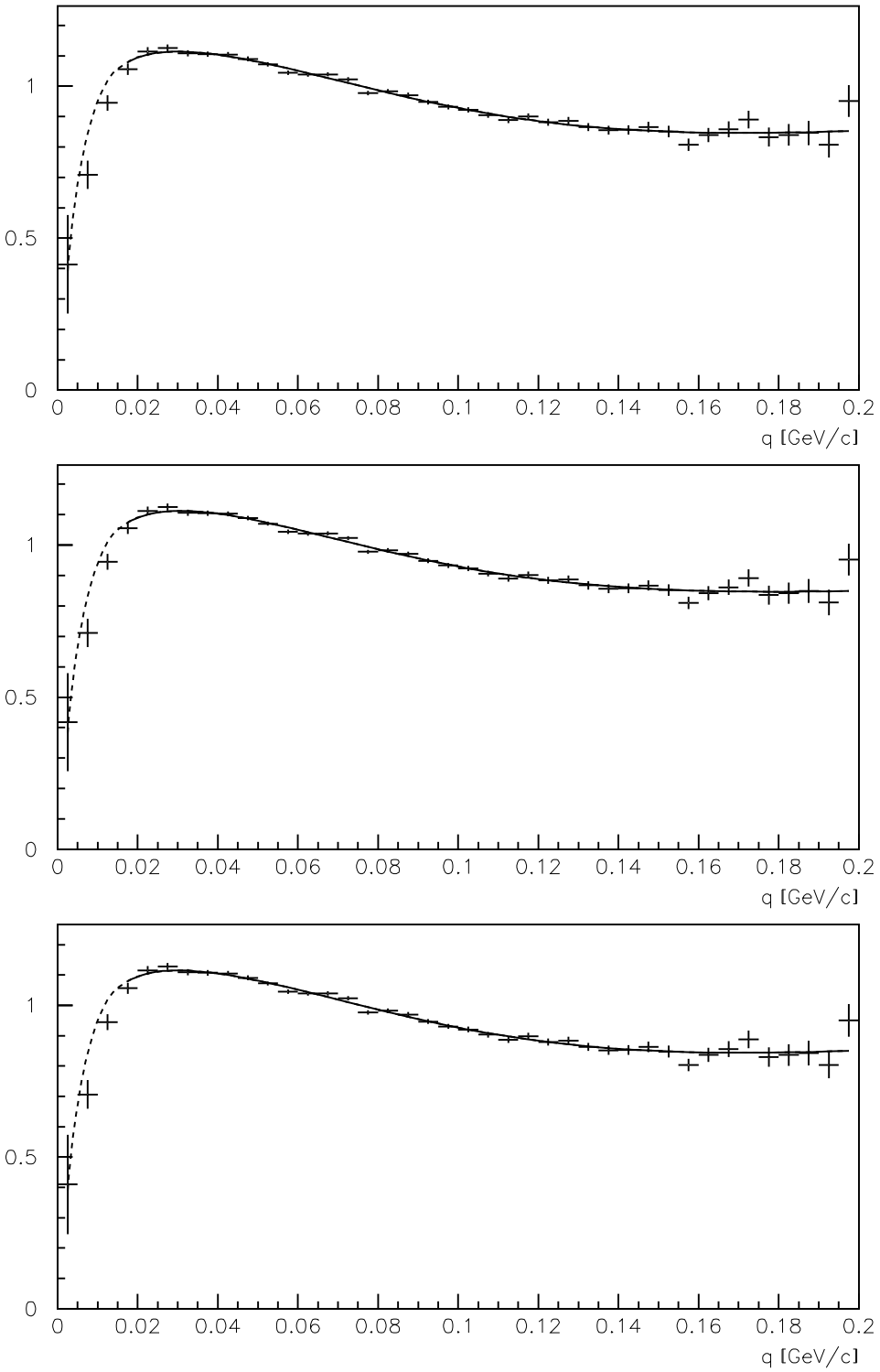

Figure 6.7: Fitted correlation functions (full lines) and their extrapolation in region of very small q (dashed lines) with expected accidental admixture of 19.2%,18.2% and 20.2%, respectively from up to down.

	Background of accidentals		
Parameter	18.2%	19.2%	20.2%
N_{all}	0.69 ± 0.01	0.70 ± 0.01	0.70 ± 0.01
λ	0.95 ± 0.01	0.95 ± 0.03	0.95 ± 0.16
$r_{\mathcal{M}}$	8.45 ± 0.80	8.04 ± 0.85	8.06 ± 0.77
α	1.20 ± 0.27	1.20 ± 0.24	1.18 ± 0.31
β	2.50 ± 0.03	2.48 ± 0.09	2.49 ± 0.02
N_{ω}	0.23 ± 0.08	0.22 ± 0.07	0.22 ± 0.08
$N_{\eta'}$	0.004 ± 0.011	0.001 ± 0.013	0.003 ± 0.06
$N_{\mathcal{G}}$	0.03 ± 0.06	0.02 ± 0.21	0.004 ± 0.14
s	1.11 ± 0.03	1.07 ± 0.03	1.04 ± 0.03
χ^2	37.53/28	37.72/28	37.86/28

Table 6.1: The results of the fits of measured $\pi^-\pi^-$ correlation function.

the influence of $\mathcal{G}$ contribution and so the fitting procedure becomes insensitive to $\mathcal{G}$ contribution.

To examine the insensitivity of the fitting procedure to η' and $\mathcal{G}$ contributions we performed the fits without these two contributions (we apply the constraints $N_{\eta'} = 0$ and $N_{\mathcal{G}} = 0$ in Eq.(6.1)). The fit results are shown in Table 6.2. If we compare χ^2 values of the fits in Tables 6.1 and 6.2 we may conclude that they are not sensitive to η' and $\mathcal{G}$ contributions.

The fitted values of N_{ω} in Tables 6.1 and 6.2 practically coincide and agree with the one predicted by UrQMD model (20.4%). Fixing zero $\mathcal{G}$ and η' contributions leads to about twice smaller error in N_{ω} (15%). We will stay however rather conservative and assume that the UrQMD model describes the ω yields with a 30% uncertainty.

6.4 Resume

The $\pi^-\pi^-$ correlation function has been extracted from the measured data and has been compared with the prediction given by the UrQMD simulation. The comparison has shown a very good agreement between description of ω pairs by the simulation and the measured correlation function. Note that the ω pairs represent the main source of the systematic shift of the $A_{2\pi}$lifetime measurement so the determination of their yield is crucial for the study of this shift.

It has not been possible to check the quality of the description of remaining three contributions due to the insensitivity of fitting procedure to η' and $\mathcal{G}$ contributions.

	Background of accidentals		
Parameter	18.2%	19.2%	20.2%
N_{all}	0.71 ± 0.01	0.71 ± 0.01	0.70 ± 0.01
λ	0.94 ± 0.02	0.92 ± 0.03	0.94 ± 0.02
$r_{\mathcal{M}}$	8.00 ± 1.51	8.03 ± 0.76	8.02 ± 0.51
α	1.19 ± 0.25	1.19 ± 0.32	1.19 ± 0.28
β	2.49 ± 0.05	2.48 ± 0.74	2.49 ± 0.03
N_{ω}	0.22 ± 0.03	0.21 ± 0.04	0.21 ± 0.03
$N_{\eta'}$	0.	0.	0.
$N_{\mathcal{G}}$	0.	0.	0.
s	1.11 ± 0.07	1.02 ± 0.09	1.05 ± 0.09
χ^2	37.55/30	37.74/30	37.84/30

Table 6.2: The results of the fits of measured $\pi^-\pi^-$ correlation function with additional constraints $N_{\eta'} = 0$ and $N_{\mathcal{G}} = 0$.

Chapter 7

Corrections to $A_{2\pi}$ lifetime measurement

The method of $A_{2\pi}$ lifetime measurement is based on the determination of breakup probability P_{br}, which is defined as a ratio of the numbers of broken-up n_A and produced N_A $A_{2\pi}$atoms. The value of P_{br} is evaluated from the measured $\pi^+\pi^-$ data according to Eq. (3.22)

$$P_{br} = \frac{n_A}{N_A} = \frac{1}{k_{th}(q)} \frac{\epsilon_{CC}}{\epsilon_A} \frac{n'_A}{n'_{CC}} \tag{7.1}$$

The negligence of the finite size of the production region and of the influence of strong FSI can lead to systematic errors in the number of measured Coulomb pairs n'_{CC}, in the number of atomic pairs n'_A (pairs from broken-up $A_{2\pi}$atoms) and in the value of theoretical factor $k_{th}(q_0) = N_A/N_{CC}$ which determines the ratio between produced $A_{2\pi}$ atoms and Coulomb pairs in the interval $q \in (0; q_0)$.

Note that the number n'_A of atomic pairs is determined as an excess of a measured q–spectrum of $\pi^+\pi^-$ pairs over an extrapolated one in the atomic signal region. The signal of atomic pairs extends up to $4MeV/c$ but a commonly used region for n'_A determination is only $q < 2MeV/c$. The construction of the extrapolated q–spectrum is based on Eq.(3.11). The parameters describing this spectrum are obtained from the fit of correlation function out of the atomic signal region, commonly in the region $q \in (4; 15)MeV/c$. The number of Coulomb pairs n'_{CC} is derived from the extrapolated q–spectrum in the same region where the signal of atomic pairs is evaluated.

7.1 Uncertainty of n'_{CC} and n'_A

The systematic errors in n'_{CC} and n'_A come from a common source, i.e. the inaccurate description of q–spectra of pairs from short-lived sources. The standard approach assumes that the behaviour of their correlation function is described

by Coulomb penetration factor $A_c(\eta)$, defined in Eq.(2.43) ($\eta = (k^*a)^{-1}$). The true behaviour is however given by the product $(1+\delta(\mathbf{k}^*))A_c(\eta)$. The omission of the correction factor $\delta(\mathbf{k}^*)$ in the standard procedure is partly compensated by a shift of the fitted parameters. Namely, the measured correlation function is fitted by formula

$$\mathcal{F}_d(q) = \lambda_1 A_c(\eta) + \lambda_2, \tag{7.2}$$

where the parameters λ_1 and λ_2 describe the contribution of pairs from short-lived sources and the contribution of all other pairs, respectively. The constraint $\lambda_1+\lambda_2 = 1$ used in Eq. (3.11) is not applied here. In case that the correction factor $\delta(\mathbf{k}^*)$ does not depend on k^* ($q = 2k^*$), the fitting procedure recovers the influence of the finite–size correction by absorbing the factor $1+\delta_f$ in the parameter λ_1 and thus giving the correct value of n'_{CC}.[1] The effect of the k^*-dependent finite-size correction factor is however only partly included in the parameter λ_1, thus leading to a systematic shift in n'_{CC}.

Since the number of atomic pairs n'_A is determined as an excess of measured q–spectrum over the extrapolated Coulomb pairs spectrum, the absolute shifts in determination of n'_{CC} and n'_A are the same (disregarding the opposite signs). The relative shift of n'_A is n'_{CC}/n'_A times higher than the shift of n'_{CC}.

The fit of $\pi^+\pi^-$ correlation function is commonly performed in the region $q \in (4;15)MeV$ and the bin width of fitted histogram is $0.25MeV/c$. The signal of atomic pairs extends to $q = 4MeV/c$ but it is usually analysed in the interval $q < 2$ MeV/c. We will follow this procedure to get closer to the real experimental conditions. The particular systematic shift is evaluated for two intervals, one commonly used for $A_{2\pi}$lifetime determination $q \in (0;2)$ and the other one involving all signals of atomic pairs $(0;4)MeV/c^2$.

Note, that q resolution of the spectrometer is at the level of 1 MeV/c, so it is worse than the width of bins. Due to the shape of the correlation function the main influence of the resolution is seen in the region of small q. In the region where the correlation function is fitted ($q > 4MeV/c$), the behaviour of this function is smooth enough and the influence of the resolution is small. We can neglect the influence of the resolution also when analysing the numbers of pairs in the intervals $(0;2)$ and $(0;4)$ MeV/c.

The "real" correlation function is constructed from the individual contributions discussed above in Chapter 5 using the method of numerical calculation. According to the prediction of UrQMD simulation we take the mixture of 15% ω, 0.7% η', 64.5% $\mathcal{M}(8, 1.2, 2.5)$ and 19.8% $\mathcal{G}$ contributions, respectively. This "real" correlation function is fitted by formula in Eq. (7.2) according to standard

[1] The fitted formula can be written in the form $g(\lambda A_c(\eta) + (1-\lambda))$. In this case the influence of the correction factor will be compensated in the product of coefficients g and λ.

[2] Note, that pion pairs from broken-up $A_{2\pi}$atoms have $q < 3MeV/c$ but due to the rescattering in the target and the influence of the spectrometer resolution the measured signal extends up to $q = 4MeV/c$

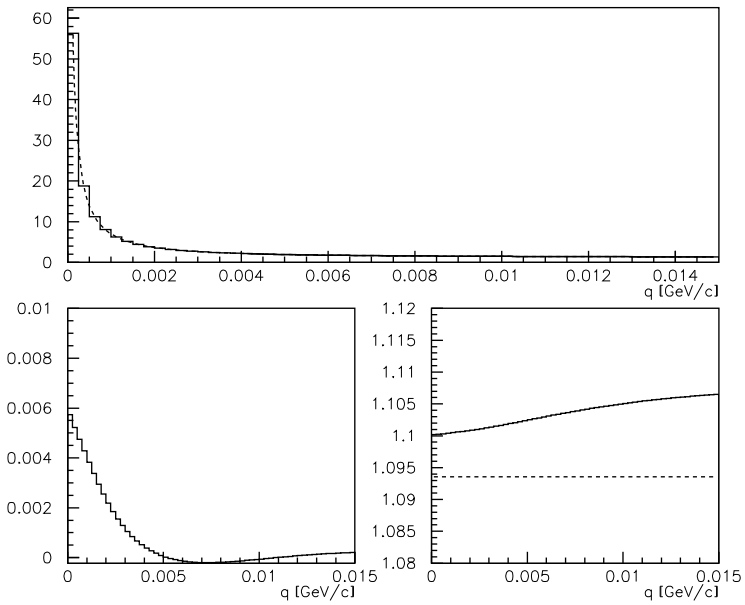

Figure 7.1: The $\pi^+\pi^-$ correlation function corresponding to the mixture of 15% ω, 0.7% η', 64.5% $\mathcal{M}(8, 1.2, 2.5)$ and 19.8% $\mathcal{G}$ contributions and their aproximation by formula given in Eq.(7.2)(dashed line) (**Top**). The relative error of this approximation as a function of q(**Bottom-left**). The corresponding correction factor $1 + \delta(\mathbf{k}^*)$ (full line) and its approximation by $\lambda_1 = 1 + \delta_f$ (dashed line) (**Bottom-right**).

DIRAC approach. The fitted values of the fraction parameters are $\lambda_1 = 1.094$ and $\lambda_2 = 0.016$. In Figure 7.1 we can see the correlation function and its approximation by the formula (7.2). In this figure the relative shift of this approximation and the correction factor $1 + \delta(\mathbf{k}^*)$ and its compensation by λ_1 parameter are also shown. A relative difference between the real correlation function and its standard approximate description in the region of $q < 4MeV/c$ is 0.44%.

To evaluate systematic shifts of n'_{CC} and n'_A, the q–distribution of the accidental pairs must be taken into account. Multiplying the simulated correlation function by this spectrum we obtain the "real" q–distribution of prompt pairs. A repetition of the same procedure for the fitted correlation function brings us the distribution according to the standard DIRAC approach. The difference of these two functions represents the systematic shift in the n'_{CC} determination.

In the signal region $q < 2MeV/c$ the value of the shift in n'_{CC} is $\delta n'_{CC} = -0.35\%$ and for $q < 4MeV/c$ we obtain $\delta n'_{CC} = -0.17\%$[3], i.e. we slightly underestimate the number of Coulomb pairs. Let us note, that for the wider signal interval of q the shift is smaller. This is due to behaviour of relative differences

[3]Here we use a notation that true value of n'_{CC} is obtained by dividing the experimental value by the factor $1 + \delta n'_{CC}$.

of the predicted q-spectrum and its approximation shown in Figure 7.2.

The measured ratios of the Coulomb and atomic pairs in the intervals $q < 2$ MeV/c and $q < 4$ MeV/c are 1/4 and 1/15, respectively. The corresponding shifts in n'_A are thus four and fifteen times higher (with opposite sign) than the shifts in $n'_C C$, i.e. $\delta n'_A = 1.4\%$ and 2.5%, respectively. Note that in contrast to n'_{CC} the systematic shift of n'_A increases with the width of the analysed signal region.

7.2 Uncertainty of k_{th} factor

The systematic error in the determination of k_{th} factor has been partially mentioned already in Section 5.2.3. There we have found, that the shift due to the finite size correction is at the level of a fraction of percent. Here we will determine this shift more precisely. The formula used for its evaluation (Eq.(3.15))

$$k_{th}(q_0) \equiv \frac{N_A}{N_{CC}} = \frac{(2\pi\alpha m_\pi)^3}{\pi} \frac{\sum_{n=1}^{\infty} \frac{1}{n^3}}{\int_0^{\eta(q_0)} A_C(\eta) d^3\eta} \tag{7.3}$$

assumes that the Coulomb pairs are produced at zero separation. To take into account the finite size of the production region and the strong FSI, the correction factors $1 + \delta(\mathbf{k}^*)$ and $1 + \delta_n$ should be introduced in this formula, i.e.

$$k_{th}(q_0) = \frac{(2\pi\alpha m_\pi)^3}{\pi} \frac{\sum_{n=1}^{\infty} (1 + \delta_n) \frac{1}{n^3}}{\int_0^{\eta(q_0)} (1 + \delta(\mathbf{k}^*)) A_C(\eta) d^3\eta}. \tag{7.4}$$

Evaluating the sum in the numerator of Eq.(7.4) up to $n = 15$ (see Figure 7.3) and computing the integral in the denominator numerically, we have found that for $q_0 = 2MeV/c$ the k_{th}–factor should be scaled by a factor of 1.0025 and for $q_0 = 4MeV/c$ it is 1.0024, i.e. the systematic shifts of $\delta k_{th}(q_0)$ are $\delta k_{th}(q_0 = 2) = -0.25\%$ and $\delta k_{th}(q_0 = 4) = -0.24\%$, respectively.

7.3 Dependence of systematic shifts on ω yields

We apply the above mentioned procedure of the evaluation of systematic shifts in determination of n'_A, n'_{CC} and k_{th} on several sets of possible mixtures of ω, η', $\mathcal{M}$ and $\mathcal{G}$ contributions. As the main source of the systematic shift is the ω contribution we concentrate on a study of its influence. We take the yields given by UrQMD simulation and suppose the 15% and 30% variation of the

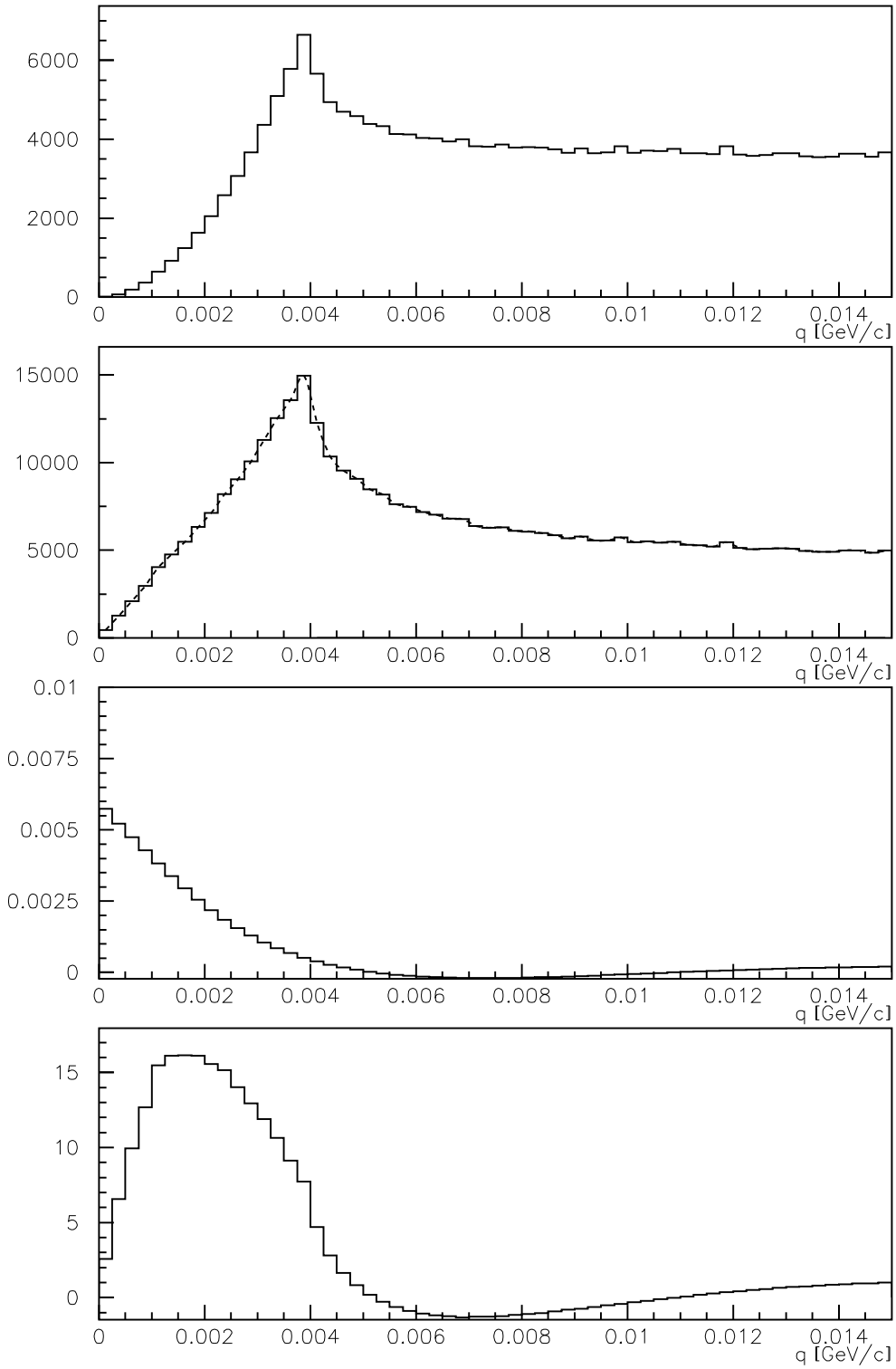

Figure 7.2: From top to bottom: (1) The q–spectrum of uncorrelated $\pi^+\pi^-$ pairs used for the final analysis. (2) The same spectrum weighted by the assumed correlation function (histogram) and its approximation (dashed line). (3) The relative difference between produced Coulomb pairs and their approximative description. (4) The shape of absolute difference between produced Coulomb pairs and their approximative description.

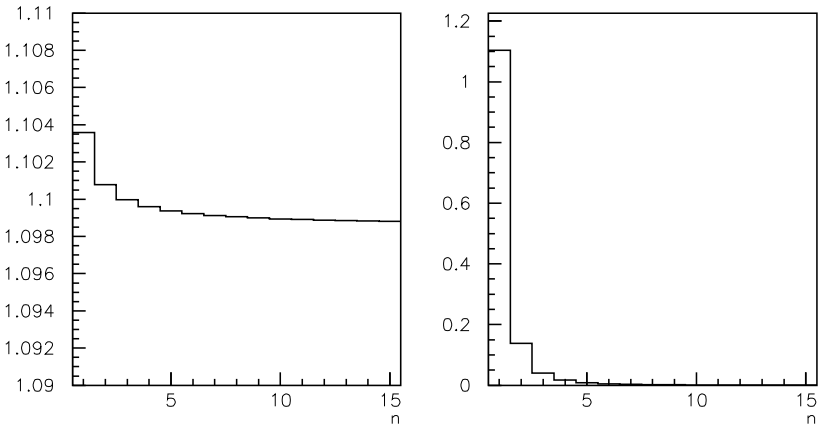

Figure 7.3: $(1+\delta_n)$ (**Left**) and $(1+\delta_n)/n^3$ (**Right**) as a function of n.

ω contribution reflecting the errors obtained in the fits of $\pi^-\pi^-$ correlation function discussed in Section 6.3. The shifts of each ω yield are studied with and without presence of η' and $\mathcal{G}$ contributions. The results obtained for both studied signal regions of q, $q < 2MeV/c$ and $q < 4MeV/c$, are summarised in Table 7.1. The shifts in P_{br} are determined according to the formula

$$(1+\delta P_{br}) = \frac{(1+\delta n'_A)}{(1+\delta k_{th})(1+\delta n'_{CC})}. \tag{7.5}$$

As seen from Table 7.1, the systematic shift due to 15% ω–contribution leads to about 1.4% and 2.5% overestimation of n'_A and about 2% and 3% overestimation of P_{br}, respectively in the region $q < 2$ and $q < 4MeV/c$. The rather conservative 30% uncertainty in ω–contribution causes the variation of the P_{br} shift $\pm 1\%$ and $\pm 1.5\%$ depending on q region. We observe only small differences when comparing the values obtained for the spectra with and without η' and $\mathcal{G}$ contributions. This shows that these two contributions along with $\mathcal{M}$[4] have a small influence on systematic shifts. This partially answers the question arising from the difference found between the numerically calculated and the weighted $\pi^-\pi^-$ correlation function. The possible discrepancy will not play a crucial role in estimation of shifts in $\pi^+\pi^-$ correlation function.

Let us note that from Table 7.1 it is obvious, that the main source of the systematic shift in P_{br} is the shift in determination of number of atomic pairs n'_A. This shift can essentially be reduced by employing the method of multi-layer target [43] in a future experiment. The multi-layer target with very thin layers and the total thickness same as the single layer target allows us to measure the spectrum of Coulomb pairs under the same conditions but practically without the influence of the atomic pairs. It means that instead of the extrapolated

[4]The neglecting of η' and $\mathcal{G}$ contribution causes a change of $\mathcal{M}$ contribution of about 20%

mixture [%] N_ω,$N_{\mathcal{M}}$,$N_{\eta'}$,$N_{\mathcal{G}}$	$q < 2MeV/c$				$q < 4MeV/c$			
	$\delta n'_{CC}$ [%]	$\delta n'_A$ [%]	δk_{th} [%]	δP_{br} [%]	$\delta n'_{CC}$ [%]	$\delta n'_A$ [%]	δk_{th} [%]	δP_{br} [%]
10,69.5,0.7,19.8	-0.15	0.61	-0.26	1.03	-0.07	1.08	-0.25	1.42
13,66.5,0.7,19.8	-0.27	1.10	-0.26	1.64	-0.13	1.98	-0.24	2.41
15,64.5,0.7,19.8	-0.35	1.39	-0.25	2.03	-0.17	2.53	-0.24	3.01
17,62.5,0.7,19.8	-0.44	1.76	-0.25	2.49	-0.22	3.24	-0.23	3.80
20,59.5,0.7,19.8	-0.56	2.24	-0.24	3.12	-0.28	4.11	-0.22	4.83
10,90,0,0	-0.10	0.42	-0.33	0.85	-0.05	0.77	-0.31	1.12
13,87,0,0	-0.22	0.89	-0.32	1.45	-0.11	1.60	-0.33	2.07
15,85,0,0	-0.31	1.25	-0.32	1.91	-0.15	2.29	-0.33	2.83
17,83,0,0	-0.40	1.61	-0.32	2.36	-0.20	2.97	-0.32	3.60
20,80,0,0	-0.45	1.82	-0.31	2.91	-0.24	3.84	-0.32	4.43

Table 7.1: The systematic shifts in the values of n'_{CC},n'_A,k_{th} and P_{br} for several sets of mixtures of ω, η', $\mathcal{M}$ and $\mathcal{G}$ contributions.

q–spectra we can use for evaluation of n'_A and n'_{CC} the measured one which is free of systematic errors due to the finite size corrections. The influence of the systematic error will remain only in the determination of the number N_A of produced $A_{2\pi}$atoms.

In general, we can conclude that the systematic errors due to the finite size corrections manifests themselves as a systematic shift in P_{br} on a level of percent. The upper estimation of this shift corresponding to 20% ω–contribution is about 3% for the commonly used region $q < 2MeV/c$. The systematic error in the determination of $A_{2\pi}$lifetime is roughly by a factor 2.5 larger, i.e. the upper limit is about 7.5%.

7.4 Resume

In this chapter the evaluation of the systematic shift due to the finite size corrections has been performed. Based on the UrQMD simulation, the systematic shift of about 2% has been found in the breakup probability P_{br} determined in the standard DIRAC procedure in the signal interval $q < 2$ MeV/c. Taking into account the rather conservative uncertainty of 30% in the yield of so called ω pairs, we arrive at the upper estimate of the shift in P_{br} of about 3%, corresponding to the shift in the pionium lifetime of about 7.5%. This error is comparable with the expected 10% statistical error.

The main source of the systematic shift has been identified to be the error in the determination of the number n'_A of atomic pairs. It can be significantly reduced by employing the measurement using a multilayer target for the deter-

mination of the spectrum of Coulomb pairs. We strongly recommend to use this method in the future experiment [44] which will aim to measure the $A_{2\pi}$lifetime better than to 6%,i.e. better than the upper estimate of the systematic shift (7.5%).

Chapter 8

Summary

In this work we have analysed possible systematic shifts in the experimental determination of the breakup probability P_{br} due to neglecting the finite size of the production region and strong FSI. The lifetime of $A_{2\pi}$ atoms is directly extracted from the value of P_{br} and the systematic shift of P_{br} appears in the extracted $A_{2\pi}$ lifetime multiplied by a factor ~ 2.5.

The size of the production region has been studied with the help of UrQMD simulations. The original code has been slightly modified to take into account the finite size of resonances. We have found that the most critical contribution to the lifetime systematic errors comes from pion pairs containing pions from ω–decays.

The results of UrQMD simulations have been compared with the $\pi^-\pi^-$ correlation function constructed from the data measured together with data for $A_{2\pi}$ lifetime determination. A good agreement between the simulated ω contribution and the measured $\pi^-\pi^-$ correlation function has been found.

We have found the upper limit of systematic shift in P_{br} due to neglecting finite size of the production region to be about 3% for the commonly used atomic pair signal interval $q < 2$ MeV/c. This value matches with the uncertainty in the $A_{2\pi}$ lifetime determination of about 7.5%.

The uncertainty in the number of atomic pairs n'_A has been identified as the main source of the systematic shift of P_{br}. This uncertainty can be significantly reduced by using the method of two targets, single and multilayer ones [43]. Therefore, we strongly recommend to use this method in the future experiment [44].

Bibliography

[1] B. Adeva *et al.*,DIRAC proposal, CERN/SPSLC 95-1 (1995).

[2] B. Adeva *et al.*, J. Phys. G: Nucl. Part. Phys. 30(2004) 1929-1946.

[3] B. Adeva *et al.*, Physics Letters B 619(2005) 50.

[4] G. Goldhaber et al., Phys. Rev. 120(1960) 300.

[5] G.I. Kopylov and M.I. Podgoretsky, Sov. J. Nucl. Phys. 15(1972) 219.

[6] R.Hanbury-Brown,R.Q. Twiss, Phil. Mag 45(1954) 663; Nature 178(1956) 1046.

[7] R. Lednicky, V. L. Lyuboshitz, Yad. Fiz 35(1982) 1316 (Sov. J. Nucl. Phys. 35(1982) 770); JINR report P2-546-92(1992) 1

[8] j. Ridky, Fortschr. Phys 36(1988) 707.

[9] R. Lednicky, Phys. of Atomic Nuclei 67(2004) 71.

[10] R. Lednicky et al., Phys. Rev. C 61(2000) 034901.

[11] R. Lednicky, V.V. Lyuboshitz, V.L. Lyuboshitz, Phys. of Atomic Nuclei 61(1998) 2050.

[12] L.D. Landau, E.M. Lifshitz, Quantum Mechanics: Non–Relativistic Theory, 3-rd Ed., Sect. 136, Pergamon Press, Oxford, 1977.

[13] G. Colangelo, J. Gasser, H. Leutwyler, Phys. Rev. Lett. **86** (2001) 5008.

[14] M. Gmitro, J. Kvasil, R. Lednicky, V.L. Lyuboshitz, Czech. J. Phys. B **36** (1986) 1281.

[15] A.B. Migdal,Zh. Eksp. Theor. Fiz. **28**(1955) 3, 10 (Sov. Phys. JETP **1**(1955) 2, 7).

[16] V.V. Anisovich, L.G. Dakhno, M.M. Makarov, Yad. Fiz. **32**(1980) 1521 (Sov. J. Nucl. Phys. **32**(1980) 788).

[17] L. Nemenov, Yad. Fiz. **41**(1985) 980.

[18] V.L. Lyuboshitz, Yad. Fiz. **48**(1988) 1501 (Sov. J. Nucl. Phys. **48**(1988) 956).

[19] J. Gasser, H. Leutwyler, Annals Phys. 158(1984) 142.

[20] G. Colangelo, J. Gasser, H Leutwyler, Phys. Lett B. 488(2000) 261.

[21] S. Pislak et al., Phys. Rev. D 67(2003) 072004.

[22] M.E. Sevior et al., Phys. Rev. Lett. 66(1991) 2569.

[23] L.G. Afanasyev *et al.*, Phys. Lett. B338(1994) 478.

[24] J.L. Uretsky, T.R. Palfrey,Jr., Phys. Rev. 96(1961) 1798.

[25] J. Gasser et al., Phys. Rev. D 64(2001) 016008.

[26] R. Lednicky, Dirac Note 2004-06(2004).

[27] L. Afanasyev, O. Voskresenskaya, Phys. Letters B **453**(1999) 302.

[28] C. Santamarina, m. Schumann, L.G. Afanasyev and T. Heim, J. Phys. B. aT. Mol. Opt. Phys. **36**(2003) 4273 [arXiv:physics/0306161]

[29] A. Lanaro, Dirac Note 2001-01(2001).

[30] B. Adeva, et al., Nucl. Instr. Meth. A515(2003) 467.

[31] M. Galas, et al., DIRAC Internal Note 1998-06(1998)

[32] D. Goldin and L. Tauscher. DIRAC Internal Note 2002-07(2002).

[33] A. Gorin et al., NIM A452(2000) 280.

[34] L. Afanasyev, V. Karpukhin, Nucl. Instr. and Meth. A492(2002) 351.

[35] A. Lanaro, DIRAC Internal Note 2002-03(2002)

[36] L. Afanasyev, et al., Nucl. Instr. and Meth. A 491(2002) 376.

[37] S. Vlachos, DIRAC Internal Note 2003-04(2003)

[38] P. Kokas, et al., Nucl. Inst. and Meth. A471(2001) 358.

[39] F.R. Leimgruber, et al., Nucl. Inst. and Meth. A364(1995) 198.

[40] J. Smolik for DIRAC experiment, AIP Conf.Proc.603:251-254,2001.

[41] Web page www.th.physik.uni-frankfurt.de/ urqmd.

[42] D. Drijard, M. Hansroul and V. Yazkov, The DIRAC offline user's Guide, and /afs/cern.ch/user/d/diracoff/public/offline/docs

[43] D. Goldin, DIRAC Thesis, "Measurement of $\pi^+\pi^-$ Bound State Lifetime with the DIRAC Spectrometer at CERN" (2005)

[44] B. Adeva *et al.*, DIRAC Addendum, CERN/SPSC/2004/009 (2004)